INVESTIGATION OF MULTIVALENT DOUBLE PEROVSKITES AS ELECTRODES FOR HIGH TEMPERATURE ENERGY CONVERSION

by

Adam John Weisenstein

A dissertation submitted in partial fulfillment
of the requirements for the degree

of

Doctor of Philosophy

in

Engineering

MONTANA STATE UNIVERSITY
Bozeman, Montana

November 2012

©COPYRIGHT

by

Adam John Weisenstein

2012

All Rights Reserved

APPROVAL

of a dissertation submitted by

Adam John Weisenstein

This dissertation has been read by each member of the dissertation committee and has been found to be satisfactory regarding content, English usage, format, citation, bibliographic style, and consistency and is ready for submission to The Graduate School.

Dr. Stephen Sofie

Approved for the Department of Mechanical Engineering

Dr. Chris Jenkins

Approved for The Graduate School

Dr. Ronald W. Larsen

STATEMENT OF PERMISSION TO USE

In presenting this dissertation in partial fulfillment of the requirements for a doctoral degree at Montana State University, I agree that the Library shall make it available to borrowers under rules of the Library. I further agree that copying of this dissertation is allowable only for scholarly purposes, consistent with "fair use" as prescribed in the U.S. Copyright Law. Requests for extensive copying or reproduction of this dissertation should be referred to ProQuest Information and Learning, 300 North Zeeb Road, Ann Arbor, Michigan 48106, to whom I have granted "the exclusive right to reproduce and distribute my dissertation in and from microform along with the non-exclusive right to reproduce and distribute my abstract in any format in whole or in part."

Adam John Weisenstein

November 2012

DEDICATION

I would like to dedicate this work to my wife and my family, for all of their love, support and understanding through this work.

ACKNOWLEDGMENTS

I first and foremost would like to thank NASA for the funding of this research. I would also like to thank my graduate committee members; Stephen Sofie, Vic Cundy, Michael Edens, Ahsan Mian, and David Miller for their time and guidance throughout this process. I am also very appreciative of Wane Stein for volunteering to be my graduate representative. I would like to thank all of the co-authors on this work including: Roberta Amendola, Nick Childs, David Driscoll, Paul Gannon, Clay Hunt, and Richard Smith. I would also like to thank my co-workers and other research groups: Julie E. Muretta, Cameron Law, Paul Gentile, Yves Idzerda's group, Hugo Schmitt's group, Steven Shaw's group, and Robert Walker's group. Finally, I would like to thank Stephen Sofie again, for all of his hard work, mentoring, advising, and enthusiasm he brought to this research.

TABLE OF CONTENTS

1. INTRODUCTION TO THE DEVELOPMENT OF THE ALL CERAMIC FUEL ELECTRODE 1

Introduction 1
Investigation into the Double Perovskite Structure 5

2. PROCESSING AND CHARACTERIZATION OF $Sr_{2-x}VMoO_{6-\delta}$ DOUBLE PEROVSKITES 16

Contribution of Authors and Co-Authors 14
Manuscript Information Page 16
Abstract 16
1. Introduction 17
2. Experimental Procedure 20
3. Experimental Results 23
3.1 X-Ray Diffraction (XRD) 23
3.2 X-ray photoelectron spectroscopy (XPS) and Rutherford backscattering analysis (RBS) 26
3.3 Redox Cycling 34
3.4 Microstructure and Micro-Hardness Testing 36
3.5 DC Resistivity Testing 41
4. Discussion 45
4.1 Formation of the Double Perovskite Structure 45
4.2 Resistivity of $Sr_{2-x}VMoO_{6-\delta}$ Double Perovskites 46
5. Conclusions 48
Acknowledgments 50
Supplimental Material for "Processing and Characterization of Sr2-xVMoO6-δ Double Perovskites 51

3. ELECTRICAL CONDUCTIVITY OF $Sr_{2-x}VMoO_6$ (x=0.0, 0.1, 0.2) DOUBLE PEROVSKITE SOLID OXIDE FUEL CELL FUEL ELECTRODE 61

Contribution of Authors and Co-Authors 60
Manuscript Information Page 61
Abstract 61
1. Introduction 62
2. Experimental 64
2.1 Synthesis 64
2.2 X-Ray Diffraction 65
2.3 Electrical Conductivity 66
2.4 Thermal Gravitational Analysis 67

TABLE OF CONTENTS - CONTINUED

2.5 X-Ray Photoelectron Spectroscopy 67
3. Results 68
3.1 X-Ray Diffraction 68
3.2 Electrical Conductivity 69
3.3 Thermal Gravitational Analysis 74
3.4 X-ray photoelectron spectroscopy 75
4. Discussion 80
5. Conclusions 82
Acknowledgements 83
Supplemental Material for "Electrical Conductivity of Sr2-xVMoO6 (x=0.0, 0.1, 0.2) Double Perovskite Solid Oxide Fuel Cell Fuel Electrode 84

4. FUEL ELECTRODE PERFORMANCE OF Sr_2VMoO_6 DOUBLE PEROVSKITES 88

Contribution of Authors and Co-Authors 87
Manuscript Information Page 88
Abstract 88
1. Introduction 89
2. Experimental Procedure 90
3. Results and Discussion 92
3.1 YSZ Electrolyte Supported SOFC 92
3.2 $Sr_{2-x}VMoO_{6-\delta}$ Infiltration 94
3.3 $SrMoO_{4-\delta}$ and $SrVO_{4-\delta}$ Infiltration 99
4. Conclusion 102
Supplemental Material for “Fuel Electrode Performance of Sr2VMoO6 Double Perovskites” 103
Physical Vapor Deposition of YSZ 103
YSZ Electrolyte Supported Fabrication 105

5. INTERCONNECT DESIGN 112

Introduction 112
Novel Design 114
Mesh Analysis 117
Conclusions 119

6. CONCLUSIONS TO THE INVESTIGATION OF MULTIVALENT DOUBLE PEROVSKITES AS ELECTRODES FOR HIGH TEMPERATURE ENERGY CONVERSION 121

TABLE OF CONTENTS - CONTINUED

Processing and Characterization of $Sr_{2-x}VMoO_{6-\delta}$ Double Perovskites 121
Electrical Conductivity of $Sr_{2-x}VMoO_6$ (x=0.0, 0.1, 0.2) Double Perovskite Solid Oxide Fuel Cell Fuel Electrode 122
Fuel Electrode Performance of Sr_2VMoO_6 Double Perovskites 122
Interconnect Design 123
Aknowledgments to the Investigation of Multivalent Double Perovskites as Electrodes for High Temperature Energy Conversion 124

REFERENCES 125

LIST OF TABLES

Table Page

1. Initial conductivity results 9
2. Elemental percentages at the surface of $Sr_{2-x}VMoO_{6-\delta}$ sintered pellets as determined by XPS 27
3. Elemental percentages at the surface of $Sr_{2-x}VMoO_{6-\delta}$ sintered pellets as determined by RBS 31
4. Yield strength and porosity of $Sr_{2-x}VMoO_{6-\delta}$ sintered pellets 40
5. Reported electrical conductivities of Sr2B'MoO_6 63
6. XPS binding energies and valence contributions for $Sr_{2-x}VMoO_{6-\delta}$ tape cast discs as prepared and after annealing in a hydrogen environment 80
7. Fuel Electrode Precursors 90

LIST OF FIGURES

Figure Page

1. Representation of a SOFC process (1) 2

2. Representation of the fuel cell's triple phase boundary (6) 3

3. Continuous Ni Metal Fuel Electrode 4

4. Discontinuous Ni Metal Fuel Electrode After 5hr at 850 °C 4

5. Phase stability and oxygen partial pressure of selected oxides (14) 6

6. Polaron hopping from V3+ to a V4+ site 6

7. Representation of an oxygen ion conducting through a double perovskite structure 8

8. Cell voltage and air electrode resistance vs. time for $La_{0.8}Sr_{0.2}MnO_{3-\delta}$ and $La_{0.7}Sr_{0.2}MnO_{3-\delta}$ perovskites (17) 8

9. % Change in Length vs. Temperature for $Sr_{2-x}VMoO_{6-\delta}$ pressed pellets 9

10. Representation of $Sr_2VMoO_{6-\delta}$ double perovskite 19

11. XRD pattern for $Sr_2VMoO_{6-\delta}$ sintered at 1300°C, 1200°C and 1100°C for 20 hours 24

12. XRD pattern for $Sr_{1.9}VMoO_{6-\delta}$ sintered at 1300°C, 1200°C and 1100°C for 20 hours 25

13. XRD pattern for $Sr_{1.8}VMoO_{6-\delta}$ sintered at 1300°C, 1200°C and 1100°C for 20 hours 26

14. XPS pattern for $Sr_2VMoO_{6-\delta}$ sintered at 1300°C 20 hours 27

LIST OF FIGURES - CONTINUED

Figure Page

15. Carbon 1s, Strontium 2p and Molybdenum 3d regions for $Sr_{2.0}VMoO_{6-\delta}$ tape casted samples sintered at 1100 ^{0}C (top) and 1300 ^{0}C (bottom) in a reducing atmosphere (5%H_2/95%N_2)..... 29

16. Oxygen 1s and vanadium 2p regions for $Sr_{2.0}VMoO_{6-\delta}$ tape casted samples sintered at 1100 ^{0}C (top) and 1300 ^{0}C (bottom) in a reducing atmosphere (5%H_2/95%N_2) 30

17. 2.5 MeV H+ RBS spectrum of a $Sr_{2.0}VMoO_{6-\delta}$ tape cast disc sample sintered at 1300 ^{0}C. SIMNRA software was used to simulate a composition of 20% Sr, 10% V, 10% Mo and 60%..... 32

18. 1.2 MeV He+ RBS spectrum of a $Sr_{2.0-x}VMoO_{6-\delta}$ pressed pellet sample sintered at 1300 ^{0}C. SIMNRA software was used to simulate a composition of 20% Sr, 10% V, 10% Mo and 60% O..... 33

19. 0.9 MeV D+ NRA spectrum of a $Sr_{2.0}VMoO_{6-\delta}$ sample sintered at 1300 ^{0}C. The spectra indicates a 0.5-0.1 μm carbon surface layer with less than 1% carbon content in the bulk..... 34

20. FESEM microstructure images of an original sintered $Sr_{1.9}VMoO_{6-\delta}$ pellet (upper left) and a redox tested $Sr_{1.9}VMoO_{6-\delta}$ pellet (bottom two images). Arrows indicate outside and inside sections of the pellets to the corresponding microstructure 35

21. SEM elemental imaging of a $Sr_{1.9}VMoO_{6-\delta}$ redox tested pellet, where top left, top right, and bottom pictures represent Sr, Mo, and V, respectively..... 36

LIST OF FIGURES - CONTINUED

Figure Page

22. FESEM/ ImageJ Binary microstructure image of the 1300˚C, 1200˚C, and 1100˚C (top left to bottom right) sintered $Sr_2VMoO_{6-\delta}$ pellets 38

23. FESEM/ ImageJ Binary microstructure image of the 1300˚C, 1200˚C, and 1100˚C (top left to bottom right) sintered $Sr_{1.9}VMoO_{6-\delta}$ pellets 39

24. FESEM/ ImageJ Binary microstructure image of the 1300˚C, 1200˚C, and 1100˚C (top left to bottom right) sintered $Sr_{1.8}VMoO_{6-\delta}$ pellets 40

25. Resistivity vs. Temperature for sintered $Sr_2VMoO_{6-\delta}$ pellets 42

26. Resistivity vs. Temperature for sintered $Sr_{1.9}VMoO_{6-\delta}$ pellets 43

27. Resistivity vs. Temperature for sintered $Sr_{1.8}VMoO_{6-\delta}$ pellet 44

28. Representation of the Scheelite structure 50

29. XRD pattern for $Sr2VWO6_{-\delta}$ 51

30. Percent change in length vs. time during sintering of $Sr_2VMoO_{6-\delta}$ pellets 52

31. Percent change in length vs. time during sintering of $Sr_2VMoO_{6-\delta}$ pellets 53

32. Percent change in length vs. time during sintering of $Sr_2VMoO_{6-\delta}$ pellets 53

33. Comparison of A-site deficient perovskite microstructures 54

34. % Change in Length vs. Time for $Sr_{2-x}VMoO_{6-\delta}$ 55

LIST OF FIGURES - CONTINUED

Figure Page

35. FESEM microstructure images of an original sintered $Sr_2VMoO_{6-\delta}$ pellet (upper left) and a redox tested $Sr_2VMoO_{6-\delta}$ pellet (bottom two images)..... 57

36. SEM elemental imaging of a $Sr_2VMoO_{6-\delta}$ redox tested pellet, where green, blue, and red represents Sr, Mo, and V, respectively..... 57

37. FESEM microstructure images of an original sintered $Sr_{1.8}VMoO_{6-\delta}$ pellet (upper left) and a redox tested $Sr_{1.8}VMoO_{6-\delta}$ pellet (bottom two and upper right images) 58

38. SEM elemental imaging of a $Sr_{1.8}VMoO_{6-\delta}$ redox tested pellet, where green, blue, and red represents Sr, Mo, and V, respectively..... 58

39. Microstructure and porosity of $Sr_{2-x}VMoO_{6-\delta}$ double perovskites sintered at 1300°C 65

40. Conductivity testing apparatus..... 67

41. XRD pattern of a Sr_2VMoO_6 pressed pellet at room temperature in air. A contaminate phase of $Sr_3V_2O_8$ is noted with circles, a small signal can also be found for the $SrMoO_4$ phase..... 69

42. Electrical conductivity of $Sr_{2-x}VMoO_{6-y}$ pressed pellets vs. temperature upon heating to and cooling from 200 ^{0}C in a nitrogen environment with 2.9% H_2O/4.9% H_2 content 71

43. Electrical conductivity of $Sr_{2-x}VMoO_{6-y}$ pressed pellets vs. temperature upon heating to and cooling from 400 ^{0}C in a nitrogen environment with 2.9% H_2O/4.9% H_2 content 72

LIST OF FIGURES - CONTINUED

Figure Page

44. Electrical conductivity of $Sr_{2-x}VMoO_{6-y}$ pressed pellets vs. temperature upon heating to and cooling from 600 ^{0}C in a nitrogen environment with 2.9% H_2O/4.9% H_2 content 73

45. Electrical conductivity of $Sr_{2-x}VMoO_{6-y}$ pressed pellets vs. temperature upon heating to and cooling from 850 ^{0}C in a nitrogen environment with 2.9% H_2O/4.9% H_2 content. The scatter in data as the $Sr_{1.9}VMoO_{6-y}$,, cools below 300 ^{0}C is due to instrument limitation in measuring such high conductivity 74

46. % change in weight of $Sr_{2-x}VMoO_{6-\delta}$ of sintered powder from 30°C up to 850°C and back down to 30°C at 2°C/min 75

47. V $2p_{3/2}$ (left) and Mo 3d (right) core-level region XPS spectra of a Sr_2VMoO_6 tape cast pellet after 30 minute annealings at 400 C and 550 C_2. The deconvolution of signal into various valence contributions is shown..... 77

48. Left to Right: O 1s and V 2p core-level region XPS spectra of a Sr_2VMoO_6 tape cast pellet as prepared, and after 30 minute annealings at 400 C, 550 C and 700 C in 10^{-6} Torr H_2. 78

49. C 1s, Sr, 2p and Mo 3d core-level region XPS spectra of a Sr_2VMoO_6 tape cast pellet a) as prepare and after 30 minute annealings at b) 400 C, c) 550 C and d) 700 C in 10^{-6} Torr H_2 79

50. Conductivity vs. Time for sintered $Sr_{2-x}VMoO_{6-\delta}$ pellets 84

51. % change in weight of $Sr_{1.9}VMoO_{6-\delta}$ of sintered powder from 30°C up to 850°C and back down to 30°C at 2°C/min. Oxygen level in amps (10^{-12}) vs. temperature in the furnace is also shown 85

LIST OF FIGURES - CONTINUED

Figure Page

52. Porous YSZ scaffold 91

53. Delamination of the Sr_2VMoO_6 fuel electrode from the YSZ electrolyte after sintering, as indicated by the red arrow 93

54. SEM elemental line scan of the interface between the YSZ and double perovskite layer 93

55. Voltage vs. Current for a Sr_2VMoO_6/YSZ/LSM SOFC at 850°C 95

56. Microstructure of a Sr_2VMoO_6 dual layer fuel electrode 95

57. Elemental mapping of the dual layer fuel electrode 96

58. XRD pattern for the $Sr_{2-x}VMoO_{6-\delta}$ solution 97

59. Ellingham Diagram (68) 98

60. XRD pattern for MoO_3 + TiH_2 99

61. SOFC performance of $SrMoO_{4-\delta}$ infiltrated fuel electrode 100

62. SOFC performance of $SrVO_{4-\delta}$ infiltrated fuel electrode 101

63. Elemental line scan of an infiltrated $SrMoO_{4-\delta}$ fuel electrode 101

64. Elemental line scan of an infiltrated $SrVO_{4-\delta}$ fuel electrode 102

65. SEM image of a YSZ PVD layer on a Sr_2VMoO_6 pellet 104

LIST OF FIGURES - CONTINUED

Figure Page

66. SEM elemental mapping of a YSZ PVD layer on a Sr_2VMoO_6 pellet 104

67. Transformation of tetragonal to monoclinic phase due to crack propagation (73) 106

68. Flexibility of a 30μm 3YSZ tape cast electrolyte 106

69. YSZ phase diagram (74) 107

70. Microstructure of 1%Ni doped 3YSZ 108

71. Microstructure of 2%Mn doped 3YSZ 109

72. Tetragonal (t) and cubic (c) peaks in YSZ (69). 110

73. XRD patter for 1%Ni and 2%Mn doped 3YSZ 111

74. Original fabricated interconnect design 113

75. Original interconnect design modeled in SolidWorks FlowExpress 114

76. New end cap interconnect design 115

77. Example of one cell stack 116

78. New interconnect design modeled in SolidWorks FlowExpress 116

79. Mesh foam at 130X 118

80. Mesh foam at 287X 118

81. Resistance vs. Time for FeCrAl foam 119

ABSTRACT

Solid Oxide Fuel Cells (SOFCs) are direct energy conversion devices that have demonstrated viability due to the associated high efficiencies, utilization of transition metal catalyst, and their unique fuel flexibility, which allows the use of dirty hydrocarbons. These high temperature systems typically utilize fuel electrodes composed of a ceramic/metal (cermet) composite that is comprised of nickel and yittria-stabilized zirconia (YSZ). While these systems have demonstrated performance potential due to the catalysis and electrical conductivity of nickel metal, a key shortcoming is the poor thermal stability of nickel metal at operating temperatures of 750-1000°C, for which increased temperature enhances performance. Nickel metal particle networks as well as other transition metal catalysts operating at high temperatures coarsen or agglomerate resulting in the loss of continuous electronic pathways. To address these challenges, new materials have been sought after to replace the mixed metal and ceramic two-phase Ni/YSZ fuel electrode.

One proposed solution is to utilize a single phase Mixed Ionic Electronic Conductor (MIEC) to replace the traditional cermet structure. In this study, the analysis and characterization of the processing and sintering of $Sr_{2-x}VMoO_{6-\delta}$ perovskites, where x=0.0, 0.1 and 0.2, was investigated. $Sr_{2-x}VMoO_{6-\delta}$ substrates were sintered in a reducing atmosphere ($5\%H_2$ $95\%N_2$) and the x-ray diffraction patterns indicate that the double perovskite is the primary phase for $Sr_{2-x}VMoO_{6-\delta}$ pellets sintered at 1200°C and 1300°C for 20 hours. However, these pellets show a secondary phase of $SrMoO_{4-\delta}$. X-ray photoelectron spectroscopy revealed a deficiency of vanadium on the pellet surfaces in which samples yielded surface vanadium concentrations of less than 5%. The vanadium inhomogeneity can be explained by the formation of the $SrMoO_{4-\delta}$ scheelite phase due to oxygen exposure on the surface of the pellets, which indicates inward vanadium migration to the bulk. $Sr_{2-x}VMoO_{6-\delta}$ pellets sintered at 1300°C showed very high conductivity, with $Sr_{1.9}VMoO_{6-\delta}$ exhibiting conductivity over 100,000S/cm at room temperature. The conductivity tests also indicate a semiconductor to metallic transition for all double perovskites related to the reduction of Mo6+ to Mo4+. Utilizing the double perovskites as fuel electrodes proved to be difficult, due to anion transport leading to secondary phases and thus delamination.

CHAPTER ONE

INTRODUCTION TO THE DEVELOPMENT OF THE ALL CERAMIC FUEL ELECTRODE

Introduction

A Solid Oxide Fuel Cell (SOFC), as shown in Figure 1, is a device that uses a chemical reaction to create electricity (1). The SOFC is comprised of three distinct layers, which are the fuel electrode (anode), electrolyte, and air electrode (cathode). The fuel and air electrodes are porous material layers where fuel (hydrogen, propane, etc) and air is introduced to the fuel cell, respectively. The electrolyte is a dense material layer establishing a Nernst membrane that creates a means of oxygen ion transfer and hence voltage potential. The SOFC is governed by the chemical reactions shown in Equations 1, 2, and 3 and is operated at 650°C to 1000°C to facilitate these reactions (2). Equations 1 and 2 show the reactions at the air electrode and fuel electrode, respectively and Equation 3 represents the overall reaction of the fuel cell.

The SOFC is governed by the Nernst Equation, as shown in Equation 4, which provides a relationship between the cell reactions the partial pressures of reactants and products. From this equation it is known that the ideal potential for a fuel cell operating at 298°K or 25°C is 1.18 for an open circuit voltage, which is derived from the reaction between hydrogen and oxygen producing a change in Gibbs free energy. This ideal open circuit voltage can be affected severely by a porous electrolyte, low purity gases, and

resistance in the electrodes (3). For SOFCs the Nernst potential is based on oxygen ion (O^{2-}) selectivity for the electrolyte.

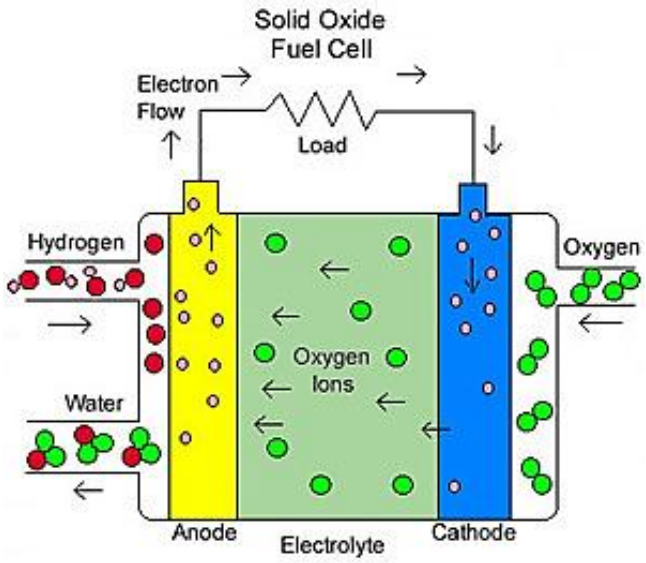


Figure 1: Representation of a SOFC process (1)

Equation 1: $1/2O_2 + 2e^- = O$

Equation 2: $H_2 + 1/2O = H_2O + 2e^-$

Equation 3: $1/2O_2 + H_2 = H_2O$

Equation 4: $E = E^o + \left(\frac{RT}{2F}\right) ln\left(\frac{P_{H2}}{P_{H2O}}\right) + \left(\frac{RT}{2F}\right) ln(P_{O2}^{\frac{1}{2}})$

SOFC's have been highly investigated in recent years because of their high efficiencies and their ability to utilize multiple fuels. However, degradation, do to nickel metal coarsening, in the fuel electrode has been shown during operation (4). The typical Ni/YSZ cermet fuel electrode consists of in excess of 35 volume % Ni metal and the remaining vol. % YSZ ceramic (5). The triple phase boundary as shown in Figure 2, is where Ni metal and YSZ ceramic meet the electrolyte. At the triple phase boundary,

oxygen ions that are transported throughout the dense electrolyte combine with H_2 and produce H_2O and two electrons to be electronically conducted throughout the fuel electrode. The reaction at the triple phase boundary is limited to the YSZ and Ni network being continuous throughout the fuel electrode, which is not necessarily the case and degrades over time with Ni metal coarsening. A continuous Ni network is shown in Figure 3 and a coarsened discontinuous network is shown in Figure 4, after exposure to 850°C for 5 hours. The triple phase boundary is limited to continuous pathways of both the metal and ceramic, because of the need for the ceramic to conduct ions and the metal to conduct electrons.

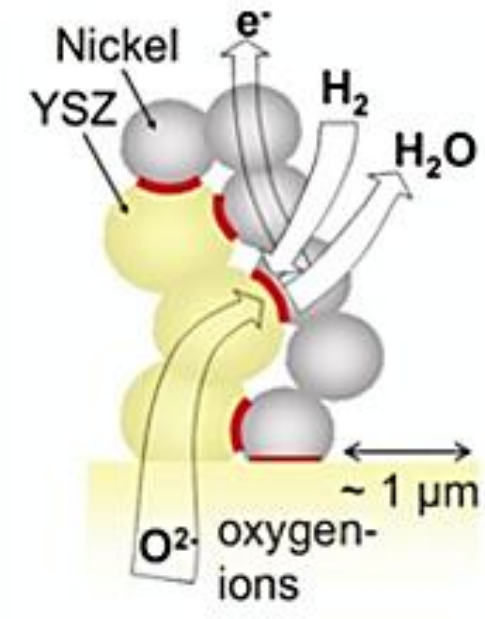


Figure 2: Representation of the fuel cell's triple phase boundary (6)

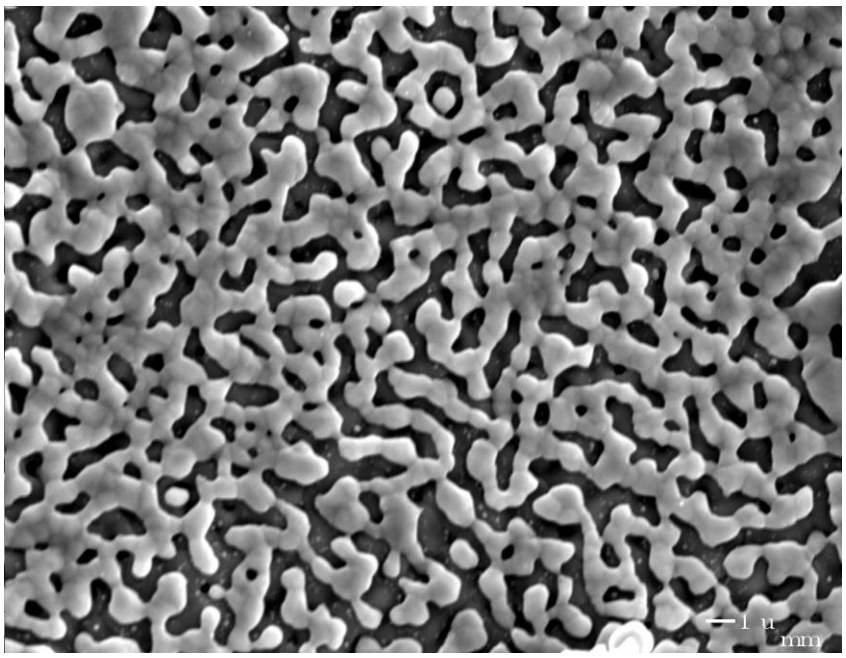


Figure 3: Continuous Ni Metal Fuel Electrode

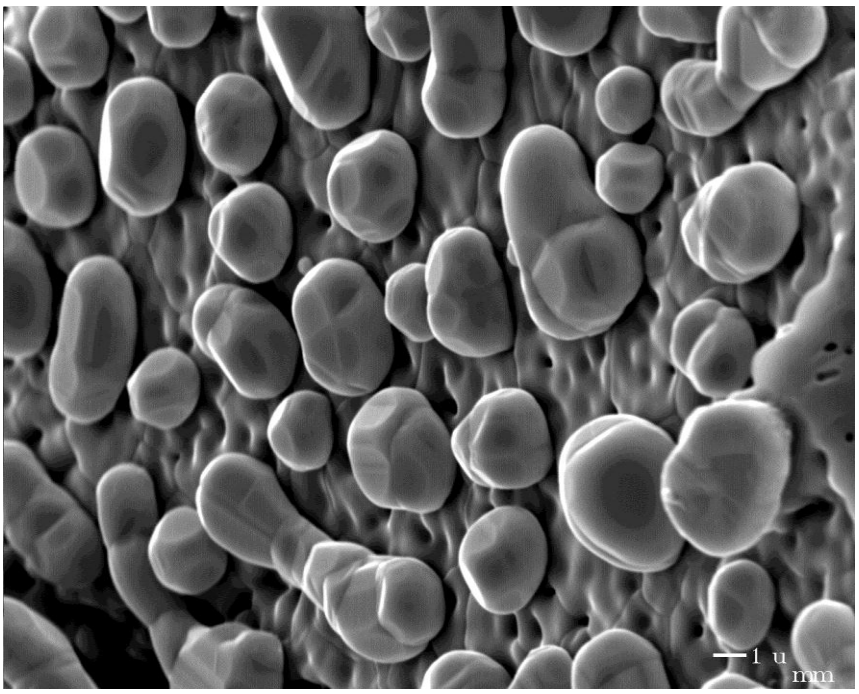


Figure 4: Discontinuous Ni Metal Fuel Electrode After 5hr at 850 °C

The continuous pathway problem can be solved with the use of a single ceramic Mixed Ionic and Electronic Conductor (MEIC). The MIEC is able to conduct both ionically and electronically throughout the length of the fuel electrode, therefore theoretically enabling the triple phase boundary to extend through the fuel electrode such that any exposed gas surface will facilitate electrochemical operation. One proposed MIEC is the double perovskite structure and therefore, is the focus of this study. The perovskite structure has been a focus of recent fuel cell research due to an ability to achieve high mixed ionic and electronic conduction (MIEC), while exhibiting high catalytic activity (7; 8; 9; 10; 11; 12). The perovskite structure has been utilized as fuel electrode, air electrode, and electrolyte in fuel cell applications.

Investigation into the Double Perovskite Structure

To begin this study seven multivalent double perovskites were investigated, e.g. $Sr_xB^IB^{II}O_{6-\delta}$, where B^I represents Ni, Ti, W, Mn, and V and B^{II} represents Mo, V, and W. These multivalent B-site elements were chosen because of the cation's ability to change valences or oxidation states depending on oxygen partial pressure. The partial pressure of oxygen encountered on the fuel electrode side varies from 10^{-18}Pa to 10^{-20}Pa (13), which could lead to multiple valence states, as shown in Figure 5. This could theoretically lead to polaron hopping. As shown in Figure 6, polaron hopping occurs when a polaron on a lower charged cation jumps to a more positively charged cation. This process continues throughout the material as long as different oxidation states are present. The polaron

hopping process was theorized by Hui et al. (14) to account for p-type to n-type behavior in perovskite type materials.

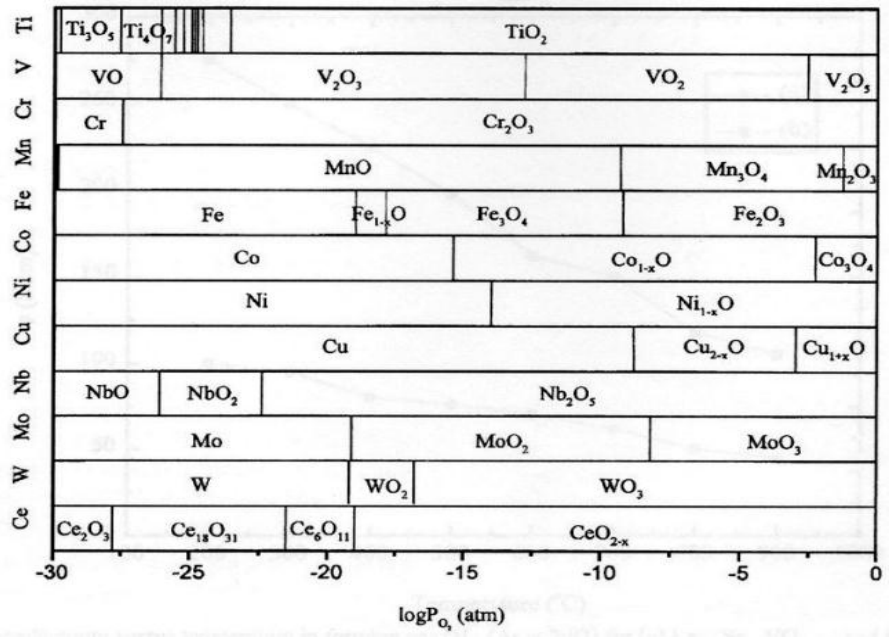


Figure 5: Phase stability and oxygen partial pressure of selected oxides (14)

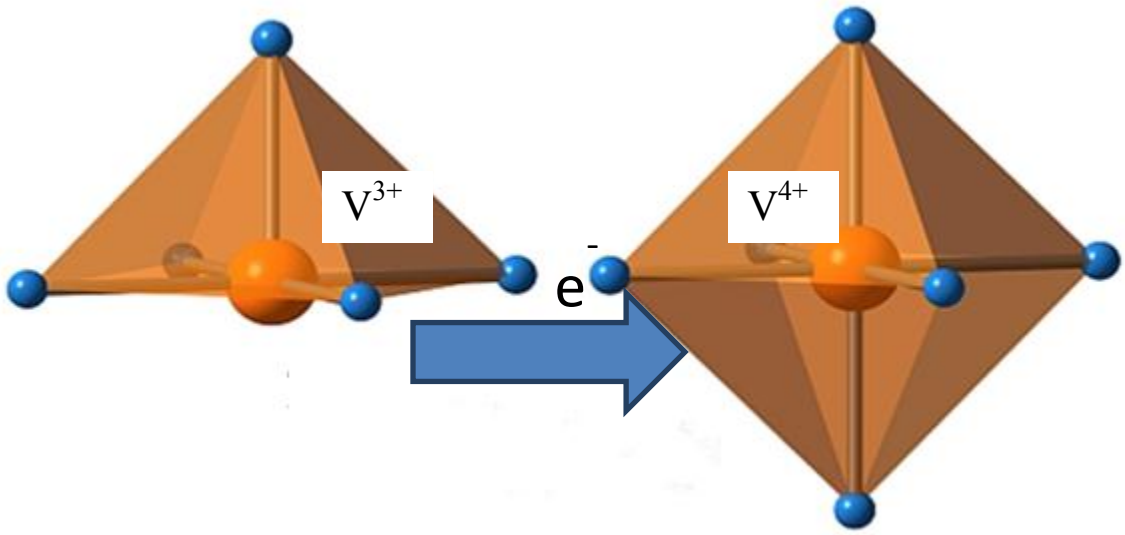


Figure 6: Polaron hopping from V3+ to a V4+ site

A-site deficiencies were also investigated as Sr_x varied from $Sr_{1.8}$ to Sr_2. A-site deficiencies can contribute to oxygen vacancies, due to charge neutrality, which can contribute to greater ionic conductivity, as shown in Figure 7, however Li et al. (15) found the electronic conductivity was reduced with increasing A-site deficiencies. Charge neutrality is shown in Equation 9, in the Processing and Characterization of $Sr_{2-x}VMoO_{6-\delta}$ Double Perovskites section. A-site deficiencies have been shown to increase fuel cell performance and decrease resistivity in common perovskites. Hiu et al. (16), found that A-site deficiencies produced from doping $SrTiO_3$ greatly increased the conductivity of the perovskite. The increase in conductivity was believed to be a consequence of the reduction of B-site cation valance state. As shown in Figure 8, Weber et al. (17) also found that the perovskite $La_{0.7}Sr_{0.2}MnO_{3-\delta}$ exhibited lower resistance and higher SOFC performance than the full stoichiometric $La_{0.8}Sr_{0.2}MnO_3$. Out of the seven initially investigated double perovskites, only $Sr_{2-x}VMoO_{6-\delta}$ was selected for more rigorous investigation due to its significant conductivity, as shown in Table 1. Three sintering temperatures were also investigated do to initial dilatometer tests performed on $Sr_{2-x}VMoO_{6-\delta}$ Double Perovskites, indicating that the highest rate of densification occurred between 1100°C and 1300°C, as shown in Figure 9. The dilatometer determined sintering temperatures correspond well to sintering temperatures reported by Karen et al. (18) for $Sr_{2-x}VMoO_{6-\delta}$ Double Perovskites.

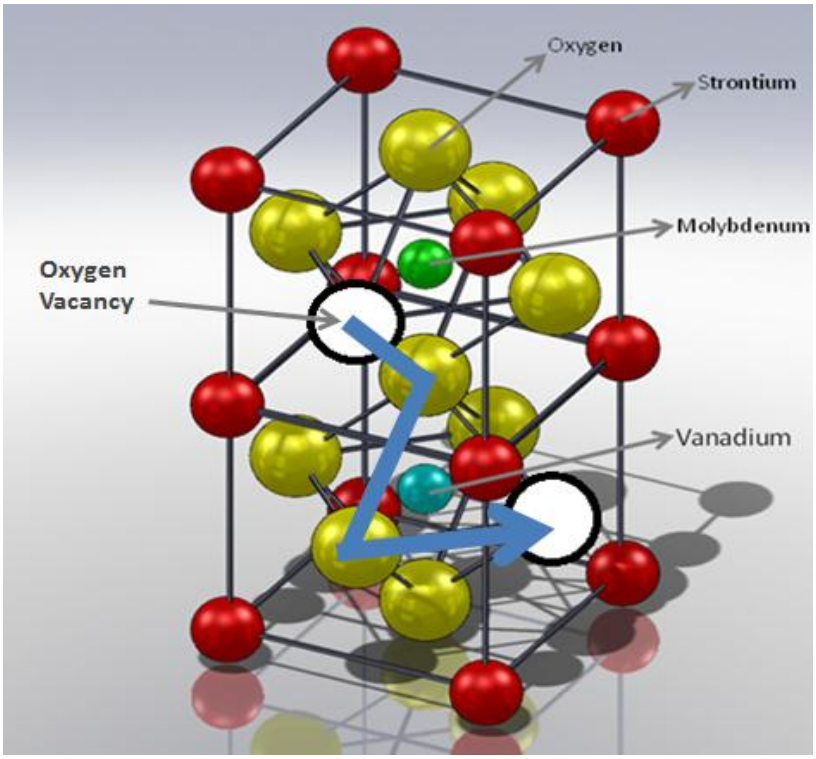


Figure 7: Representation of an oxygen ion conducting through a double perovskite structure

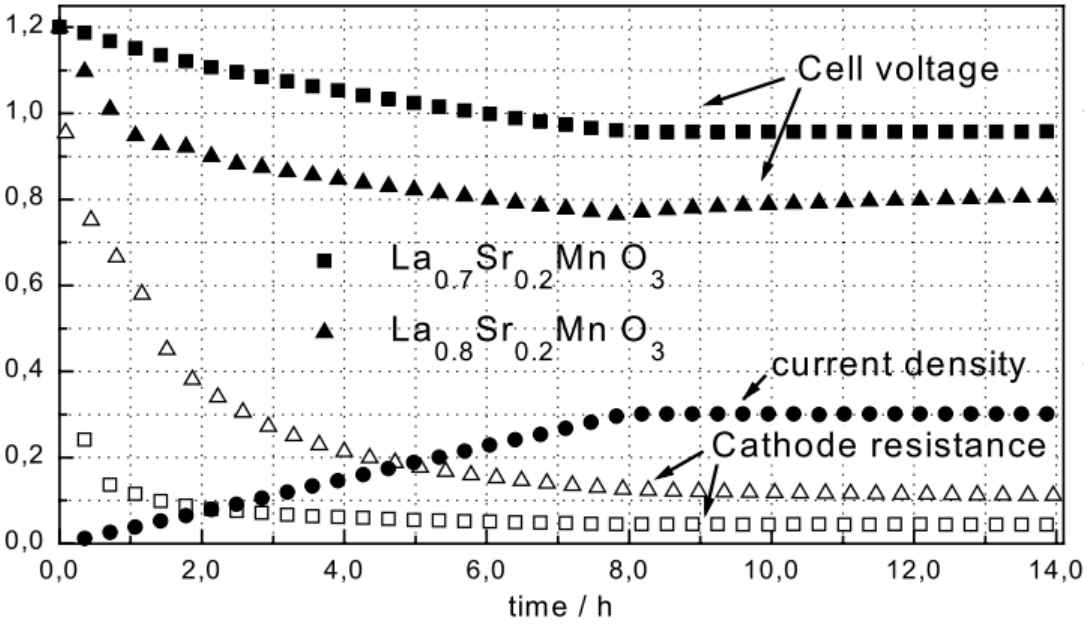


Figure 8: Cell voltage and air electrode resistance vs. time for $La_{0.8}Sr_{0.2}MnO_{3-\delta}$ and $La_{0.7}Sr_{0.2}MnO_{3-\delta}$ perovskites (17)

Table 1: Initial conductivity results

Investigated Double Perovskite	Maximum Conductiviy (S/cm)
Sr_2NiMoO_6	<1
Sr_2TiMoO_6	<1
Sr_2VMoO_6	12556
Sr_2VNiO_6	<1
Sr_2VMnO_6	<1
Sr_2VWO_6	65
Sr_2WMoO_6	<1

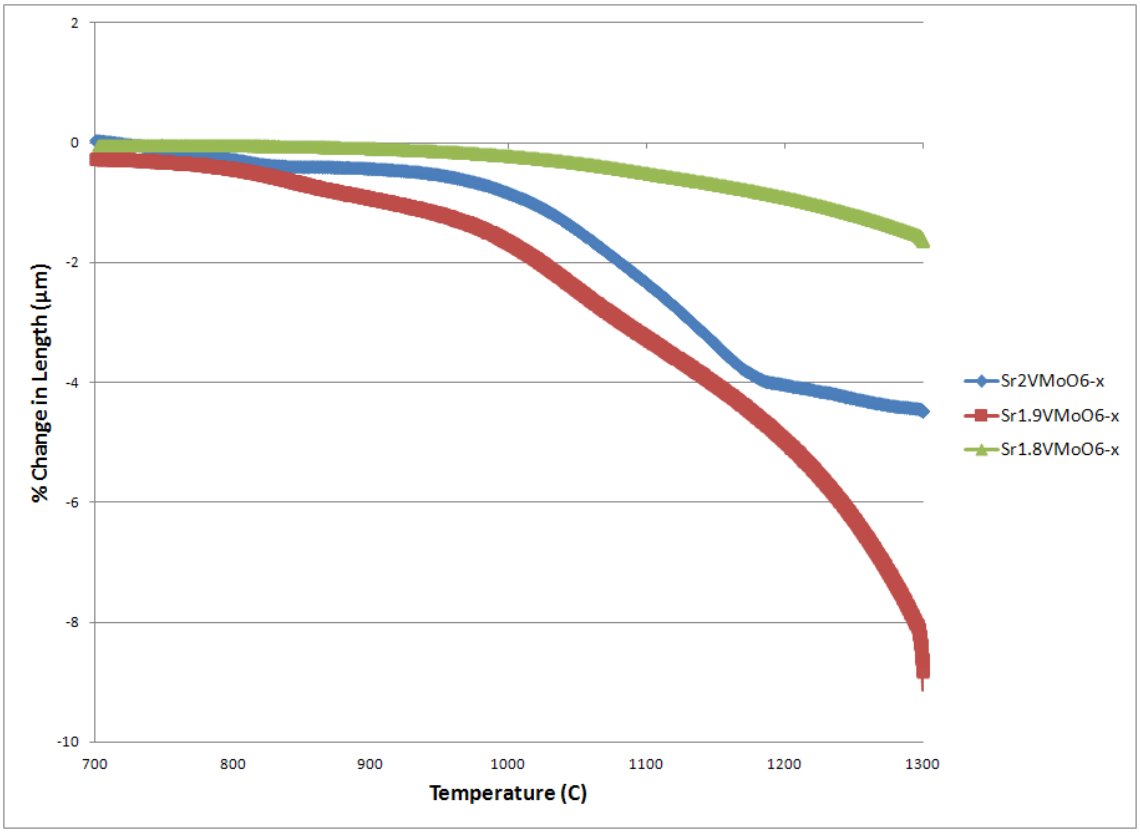


Figure 9: % Change in Length vs. Temperature for $Sr_{2-x}VMoO_{6-\delta}$ pressed pellets

Three papers were written for publication and a design being considered for patent submission was completed during this investigation into the $Sr_{2-x}VMoO_{6-\delta}$ double perovskites. The first publication titled "Processing and Characterization of $Sr_{2-x}VMoO_{6-\delta}$ Double Perovskites" was an analysis and characterization of the processing and sintering of $Sr_{2-x}VMoO_{6-\delta}$ perovskites, where x=0.0, 0.1 and 0.2. These double perovskites were investigated with application potential in high temperature fuel cell electrodes and electro-catalysts. The analysis included the following: dilatometery, X-Ray Diffraction (XRD), X-ray Photoelectron Spectroscopy (XPS), Rutherford Backscattering Spectroscopy (RBS), Field Emission Scanning Electronic Microscopy (FESEM), micro-hardness testing, and DC conductivity testing. Dilatometery was utilized to determine the change in length due to changes in temperature and XRD was used to determine the phases present in these sintered materials. Surface sensitive XPS and bulk sensitive RBS were utilized to determine elemental concentrations at different depths within the double perovskites and XPS was also used for valence state analysis. The microstructure and porosity of the material was determined from FESEM analysis, while the hardness and resistivity was determined from the micro-hardness testing and DC conductivity testing. The x-ray diffraction patterns indicate that the double perovskite is the primary phase for $Sr_{2-x}VMoO_{6-\delta}$ pellets sintered at 1200°C and 1300°C for 20 hours; however, these pellets show a secondary phase of $SrMoO_{4-\delta}$. X-ray photoelectron spectroscopy revealed a deficiency of vanadium on the pellet surfaces, in which samples yielded surface vanadium concentrations of less than 5%. The vanadium inhomogeneity can be explained by the formation of the $SrMoO_{4-\delta}$ scheelite phase

(ABO_4) due to oxygen exposure on the surface of the pellets, which indicates inward vanadium migration to the bulk, and was exhibited in redox cycling. $Sr_{2-x}VMoO_{6-\delta}$ pellets sintered at 1300°C showed the lowest resistivity at both SOFC operating temperature (800°C) and room temperature. The resistivity tests also show a semiconductor to metallic transition for all double perovskites, from heating up to 800°C to cooling down to room temperature in a reducing atmosphere, related to the reduction of Mo6+ to Mo4+.

The second publication titled "Mechanisms of Conduction of Sr2-xVMoO6-δ Double Perovskites" was an in-depth look into the conduction due to changes in the double perovskite. Electrical conductivity of $Sr_{2-x}VMoO_{6-y}$ (x=0.0, 0.1, 0.2) solid oxide fuel electrode material was investigated in a reducing atmosphere at temperatures up to 800 ^{0}C. A solid state synthesis technique was used to fabricate the materials and the crystal structure was verified through XRD. Elemental valence states were identified through XPS on the double perovskite material before and after annealing in a hydrogen environment. Samples exhibited metallic conduction with electrical conductivities of 1250 S/cm ($Sr_2VMoO_{6-y'}$), 2530 S/cm ($Sr_{1.8}VMoO_{6-y''}$) and 3610 S/cm ($Sr_{1.9}VMoO_{6-y'''}$) at 800 ^{0}C in 5%H_2/95%N_2. A highly insulating phase begins to reduce between 400^{0}C and 500 ^{0}C in a 5%H_2/95%N_2 environment. This was confirmed by XPS valence state analysis and Thermal Gravimetric Analysis (TGA). The TGA was able to measure the weight gain and loss of the double perovksite with temperature changes and indicated that major changes were happing from 400^{0}C to 600^{0}C. This reduction leads to a large increase in electrical conductivity. The electrical conductivity of $Sr_{2-x}VMoO_{6-\delta}$ materials

at 800 ˚C in a 2.9% H_2O/ 4.9%H_2/92.2%N_2 environment exceeds that reported for state of the art Ni-YSZ fuel electrode by a factor of ~1.25-3 at the same temperature in similar environments. Polycrystalline $Sr_{1.9}VMoO_{6-\delta}$ samples exhibited higher conductivity than that reported for $SrMoO_3$ polycrystalline samples. A single crystal sample of $Sr_{1.9}VMoO_{6-\delta}$ could be a candidate for the highest known conducting oxide.

The third publication titled "Fabrication and testing of SOFC electrolyte supported cells utilizing $Sr_{2-x}VMoO_{6-\delta}$ fuel electrodes" was an investigation into the SOFC fabrication and electrochemical behavior of the double perovskites as fuel electrodes. $Sr_2VMoO_{6-\delta}$ fuel electrodes were synthesized utilizing both solid state synthesis and solution synthesis. The solid state synthesized powders were applied by screen printing, however a problem that was encountered when utilizing the double perovskite fuel electrode with the YSZ electrolyte was the delamination of the electrode from the electrolyte during the sintering of the two layers. The SEM elemental line scans indicated that there is no major migration of the cation elements around the interface. This would indicate that there is not a large amount of $SrZrO_3$ formation between the YSZ and $Sr_2VMoO_{6-\delta}$. However, an anion reaction between YSZ and $Sr_2VMoO_{6-\delta}$ layers could result in the formation of the $SrMoO_4$ scheelite structure. The infiltrated SOFC with the solution $Sr_2VMoO_{6-\delta}$ was able to produce max power density of 194.8mW/cm^2 at 0.87V. However, upon further XRD analysis, the perovskite phase was not fully developed at 850°C, which lead to the investigation into the infiltration of $SrBO_{4-\delta}$ fuel electrodes. Both of these electrodes performed well despite the lack of good cation infiltration.

SOFC stack testing was also investigated in this research, which produced a novel interconnect design being considered for patent submission. One of the additional goals of this research was to test the fabricated SOFCs in a stack design for purposes of demonstrating reversible SOFC technologies for NASA applications. A rough preliminary interconnect design was developed through a senior Capstone project and provided a framework and overall dimensions suitable for stack testing at Montana State University. While perhaps sufficient for demonstrating short stack tests, many opportunities for improvement have been identified. The senior capstone project designers lacked direct hands on experience in fabricating and testing fuel cells, which has required substantial revisions to serve as a permanent test bed for reversible stacks for both commercial fabricated and in house (MSU) fabricated SOFCs. The proposed novel design is dramatically simplified in that there are no flow channels needed, with only two holes for the incoming and outgoing gas. Based on the current methods of testing single cells with flow meshes, this new design is achievable because of the Ni and FeCrAl mesh that is placed on the top and the bottom of the fuel cell, to serve as a flow path. The foam creates multiple flow channels and acts like multiple flow channels in all directions. This new design is capable of solving the problems with the original design by eliminating the gas manifolds, 90 degree edges, and complexity of the overall design which is important given the high cost of the alloy and poor machineablility. The new design also allows for different size fuel cells to be utilized, because the inlet and outlet holes are brought into the middle of the interconnect enabling any size from 53mm to 18.5mm in diameter mesh and mica seal to be used.

CHAPTER TWO

PROCESSING AND CHARACTERIZATION OF $Sr_{2-x}VMoO_{6-\delta}$ DOUBLE PEROVSKITES

Contribution of Authors and Co-Authors

Manuscripts in Chapters 2, 3, and 4

Author: Adam Weisenstein

Contributions: Synthesized double perovskite powders and pellets. Performed dilatrometry, microhardness, and resistivity measurements. Drafted initial manuscript.

Co-Author: Nick Childs

Contributions: Performed RBS and XPS analysis. Collaborated on the drafting of the manuscript.

Co-Author: Roberta Amendola

Contributions: Assisted in performing initial XPS and collaborated on the drafting of the manuscript.

Co-Author: David Driscoll

Contributions: Performed XRD and collaborated on the drafting of the manuscript.

Co-Author: Stephen Sofie

Contributions: Collaborated on the conception and design of the investigation and provided important intellectual content to the manuscript.

Co-Author: Paul Gannon

Contributions: Collaborated on the conception and design of the investigation and provided important intellectual content to the manuscript.

Co-Author: Richard Smith

Contributions: Collaborated on the conception and design of the investigation and provided important intellectual content to the manuscript.

Manuscript Information Page

Adam Weisenstein, Nick Childs, Roberta Amendola, David Driscoll, Stephen Sofie, Paul Gannon, Richard Smith
Journal of Materials Chemistry and Physics
Status of Manuscript:
____ Prepared for submission to a peer-reviewed journal
__X_ Officially submitted to a peer-review journal
____ Accepted by a peer-reviewed journal
____ Published in a peer-reviewed journal

Elsevier
Submitted October, 2012

CHAPTER TWO

PROCESSING AND CHARACTERIZATION OF $Sr_{2-x}VMoO_{6-\delta}$ DOUBLE PEROVSKITES

Abstract

In this study, the analysis and characterization of the processing and sintering of $Sr_{2-x}VMoO_{6-\delta}$ perovskites, where x=0.0, 0.1 and 0.2, was investigated with application potential in high temperature fuel cell electrodes and electro-catalysts. $Sr_{2-x}VMoO_{6-\delta}$ substrates were sintered in a reducing (5%H_2 95%N_2) atmosphere at 1100°C, 1200°C, and 1300°C. The x-ray diffraction patterns indicate that the double perovskite is the primary phase for $Sr_{2-x}VMoO_{6-\delta}$ pellets sintered at 1200°C and 1300°C for 20 hours; however, these pellets show a secondary phase of $SrMoO_{4-\delta}$. X-ray photoelectron spectroscopy revealed a deficiency of vanadium on the pellet surfaces, in which samples yielded surface vanadium concentrations of less than 5%. The vanadium inhomogeneity can be explained by the formation of the $SrMoO_{4-\delta}$ scheelite phase (ABO_4) due to oxygen exposure on the surface of the pellets, which indicates inward vanadium migration to the bulk, and was exhibited in redox cycling. $Sr_{2-x}VMoO_{6-\delta}$ pellets sintered at 1300°C showed the lowest resistivity at both SOFC operating temperature (800°C) and room temperature. The resistivity tests also show a semiconductor to metallic transition for all double perovskites, from heating up to 800°C to cooling down to room temperature in a reducing atmosphere, related to the reduction of Mo6+ to Mo4+.

Keywords: Solid Oxide Fuel Cell; Double Perovskite; Synthesis; Structure; Properties

1. Introduction

Solid Oxide Fuel Cells (SOFCs) have demonstrated an ability to be a viable source of energy production because of the associated high efficiencies and their unique fuel flexibility, which allows the use of dirty hydrocarbons. However, SOFCs typically utilize fuel electrodes composed of nickel and yittria-stabilized zirconia (YSZ), which contribute to many short comings. These short comings include nickel metal coarsening that leads to agglomeration and extreme sensitivity to fuel impurities. Metal catalysts operating at high temperatures, including nickel, coarsen resulting in the loss of continuous electronic pathways at SOFC operating temperatures. This can lead to a reduced triple phase boundary length, which can be detrimental to the longevity and performance of the fuel cell (19; 5; 20). Further, studies have shown sulfur, a contaminant in most fossil fuels, to irreversibly poison the nickel catalyst (21). To address these challenges, new materials have been sought after to replace the mixed metal and ceramic two-phase Ni/YSZ fuel electrode.

One proposed solution is to utilize a single phase Mixed Ionic Electronic Conductor (MIEC) to replace the traditional cermet structure (22; 23). Normally, current collection is limited to the nickel network being continuous throughout the fuel electrode and degrades over time with nickel metal coarsening (19). However, the continuous pathway problem could be solved with the use of a single phase MIEC ceramic as a fuel electrode. The MIEC structure can also extend the triple phase boundary through the fuel electrode such that any exposed gas surface will facilitate electrochemical operation. This study is focused on examining the double perovskite structure, as shown in Figure

10, because of the potential to engineer mixed ionic and electronic conduction, thermal and chemical stability, high tolerance to sulfur, and good single-cell performance in hydrogen and methane (24; 25). The double perovskite structure allows the engineering of two discrete unit cells to modify properties, because its structure consists of long range repeating layers of two discrete single perovskites. In some manner this structure acts as a composite that is ordered at the atomic level. A limited number of double perovskites have been researched and utilized as fuel electrodes; such as Sr_2MnMoO_6, $Sr_2Mg_{1-x}MnMoO_6$, and, $Sr_2Fe_{4/3}Mo_{2/3}O_6$ and have shown electrical conductivities in the 450 S/cm, 10 S/cm, and 16 S/cm range, respectively (24; 25; 26). The double perovskites A_2VMoO_6, where A=Ca and Sr, have also been investigated and have shown conductivities as high as 3,600 S/cm and 12,000 S/cm, respectively (18). Traditional Ni/YSZ fuel electrodes have exhibited conductivities of 0.1 S/cm, 40 S/cm, and 989 S/cm for nickel contents of 15, 30, and 50 volume percent (27), which is substantially less than the bulk nickel reported conductivity of 25,906 S/cm at 900˚K (28). This indicates that a double perovskite can provide adequate to exceptional electrical conductivity for a SOFC, providing that electro catalysis can also be facilitated.

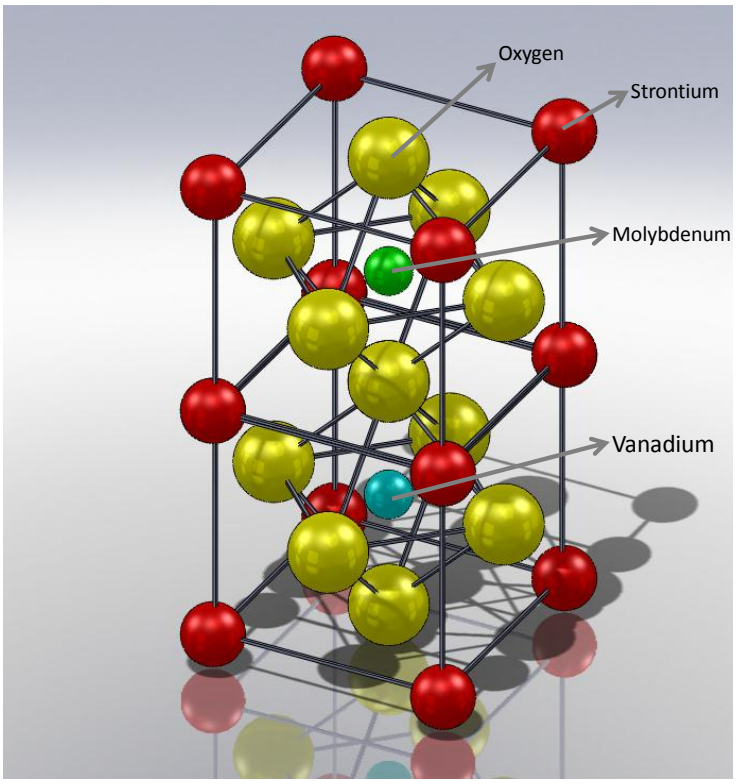


Figure 10: Representation of $Sr_2VMoO_{6-\delta}$ double perovskite

$Sr_{2-x}VMoO_{6-\delta}$ perovskites, where x=0.0, 0.1 and 0.2, were selected for investigation due to the significant conductivity observed in initial testing and reported catalytic activity of molybdenum and vanadium oxides (29; 30). Several multivalent double perovskites were also initially investigated (e.g. $Sr_2B^IB^{II}O_6$, where B^I represents Ni, Ti, W, Mn, and V and B^{II} represents Mo, V, and W); however the resulting conductivities were lower than 100S/cm which was not within the scope of this study. Analysis and characterization of the processing and sintering of the $Sr_{2-x}VMoO_{6-\delta}$ powders/pellets utilizing: dilatometery, X-Ray Diffraction (XRD), X-ray Photoelectron Spectroscopy (XPS), Rutherford Backscattering Spectroscopy (RBS), Nuclear Reaction

Analysis (NRA), Field Emission Scanning Electronic Microscopy (FESEM), micro-hardness testing, and DC conductivity testing was investigated due to the relative novelty of the double perovskite materials and the lack of published material pertaining to the material structure and properties resulting from fabrication and variations in stoichiometry. In this manner, the focus of this research is to identify the means by which these materials can be repeatedly fabricated and to understand how variations in stoichiometry and sintering temperature impact chemical phase, elemental concentration and valence states, which in turn govern important fuel electrode properties such as microstructure, coefficient of thermal expansion, mechanical strength, and resistivity.

2. Experimental Procedure

As received Alfa Aesar $Sr_{2-x}VMoO_{6-\delta}$ precursor powders ($SrCO_3$ Stock#14343, VO_2 Stock#22957, and MoO_2 Stock#48117 at 58.3, 16.4, 25.3 weight%, respectively), were combined with 40g of deionized water, ball milled for 24 hours, and then flash frozen with liquid nitrogen. The frozen slurry was then placed into a Virtis Advantage vacuum freezer, for at least 96 hours, where the liquid was sublimed from the slurry, producing well homogenized powders without agglomeration and precursor separation through traditional drying processes. The powders were then calcined in a box furnace at 1000°C for 6 hours at a heating rate of 5°C/min and a cooling rate of 10°C/min and then ground by hand with a mortar and pestle. Pellets for sintering in the dilatometer were fabricated by pressing the thermally treated powders in a 6.35mm (1/4in) die at 250 MPa. $Sr_{2-x}VMoO_{6-\delta}$ disks were also prepared, for valence state and chemical shift analysis by

XPS, by utilizing the tape casting method at a solids loading of 30%, where 25.4mm (1 in) disks were subsequently punched out of the green tapes for sintering.

Pressed pellets and tape cast disks were sintered in a reducing (5%H_2 95%N_2) atmosphere at 1100°C, 1200°C, and 1300°C in both a Linseis dilatometer L75 and an atmosphere controlled tube furnace (MTI, GSL 1500X), respectively, at a heating/cooling rate of 10°C/min for 20 hours. The three sintering temperatures were determined from initial dilatometer tests performed on all of the investigated double perovskites, indicating that the highest rate of densification occurred between 1100°C and 1300°C, which corresponds to sintering temperatures reported by Karen et al (18).

Phase characterization of the dilatometer sintered pellets was performed by X-Ray Diffraction (XRD) (Scintag X1, $CuK_{\alpha 1}$=1.5406Å) where an aluminum bracket was fabricated to hold the 6.35mm (1/4in) pellets for analysis. X-ray Photoelectron Spectroscopy (XPS, Physical Electronics 5600) was utilized on the same sintered pellets to determine the elemental percentages at a depth of approximately 1 nanometer and to identify chemical shifts and valence states of the elemental species. The C 1s, O 1s, V 2p, Sr 2p and Mo 3d core-level regions of the XPS spectrum were recorded. The spectrometer energies were calibrated to the O 1s (530.0 eV) peak for the V 2p region and to the C 1s (284.8 eV) peak for the Sr 2p and Mo 3d regions of the spectrum. XPS was performed with a magnesium X-ray source (Mg Kα = 1253.6 eV) operated at 15 kV and 15 mA. A Shirley background was used during peak fitting and a Marquardt-Levenberg optimization algorithm was used to deconvolute peaks into various charge state contributions (31). RBS with 2.5 MeV H^+ and 1.2 MeV He^+ ion beams was used to

determine bulk compositional analysis of $Sr_{2-x}VMoO_{6-\delta}$ samples sintered at 1300 ˚C. NRA with a 0.9 MeV D+ beam was used to determine carbon content through the $^{12}C(d,p)^{13}C$ nuclear reaction. The H+ and D+ beams were incident on the samples at 7^0 from normal with a scattering angle of 150^0, and the He^+ was incident normal to the sample with a scattering angle of 165^0. The integrated charge for the H^+, He^+ and D^+ spectra was 80 μC, 48 μC and 40 μC respectively. Simulation of measured spectra was performed with the software program SIMNRA (32).

Scanning electron microscopy (FE-SEM Zeiss SUPRA 55VP) was utilized at 1000x for each pellet and these microstructures were then analyzed in binary image processing software ImageJ, where the pictures were converted to a binary color scheme and porosity was evaluated. Dilatometer tests were performed on all of the $Sr_{2-x}VMoO_{6-\delta}$ pellets sintered from 1100°C to 1300°C to determine the double perovskite sintering characteristics. $Sr_{2-x}VMoO_{6-\delta}$ pellets sintered at 1300°C were also redox tested in a Linseis dilatometer L75 to observe the ability of the double perovskites to reduce and oxidize at 800°C in three different oxygen partial pressures. The redox cycle testing consisted of alternating between forming gas ($95\%N_2/5\%H_2$), nitrogen, and air at one hour intervals. SEM was used to investigate the microstructure of the redox cycled double perovskites.

A LECO microhardness tester with a test load of 200gf was used to conduct Vickers hardness tests on the sintered pellets to identify the relative strength of the materials relative to the sintering process. Multiple measurements were made on the surface of the pellets and then the theoretical yield strength was estimated and averaged.

DC conductivity tests were performed on the double perovskite sintered pellets by connecting silver wire leads to sintered pellets via silver paste using the standard 4-probe measurement technique utilizing an Agilent 34420A Nano Volt Meter. The samples were then clamped into a stainless steel fixture with electrical insulating alumina plates and placed inside a tube furnace for which a controlled atmosphere could be introduced. Resistivity tests were then performed on all sintered pellets, heating from 20°C to 800°C and then cooling to room temperature, in a reducing environment (5%H_2 and 95%N_2). The non-invasive XRD, XPS, RBS, hardness testing, and resistivity tests were performed on the dilatometer sintered pellets, prior to the invasive investigation of the microstructure.

3. Experimental Results

3.1 X-Ray Diffraction (XRD)

The XRD patterns for the double perovskites are shown in Figures 11, 12, and 13. The XRD patterns in Figure 11 indicate that the double perovskite is the main phase for $Sr_2VMoO_{6-\delta}$ pellets sintered at 1200°C and 1300°C for 20 hours; however these pellets show a scheelite-type secondary phase of ABO_4, where A represents Sr and B represents V or Mo. The XRD pattern for $Sr_2VMoO_{6-\delta}$ pellets sintered at 1100°C for 20 hours indicates that the ABO_4 structure is the primary phase, while showing a double perovskite secondary phase. As shown in Figures 12 and 13, $Sr_{1.9}VMoO_{6-\delta}$ and $Sr_{1.8}VMoO_{6-\delta}$ also exhibit the double perovskite as the main phase for the pellets sintered at 1200°C and 1300°C for 20 hours, with a secondary scheelite phase. Also, $Sr_{1.9}VMoO_{6-\delta}$ sintered at 1200°C shows a phase pure double perovskite. These tests indicate that the scheelite

phase is reduced and the desired double perovskite $Sr_{2-x}VMoO_{6-\delta}$ structure is formed as the sintering temperature increases. The presence of $SrMoO_4$ prompted investigation into the electrical conductivity of the phase, as described in the DC Conductivity section, where it was found to have low conductivity when compared to the double perovskite structure.

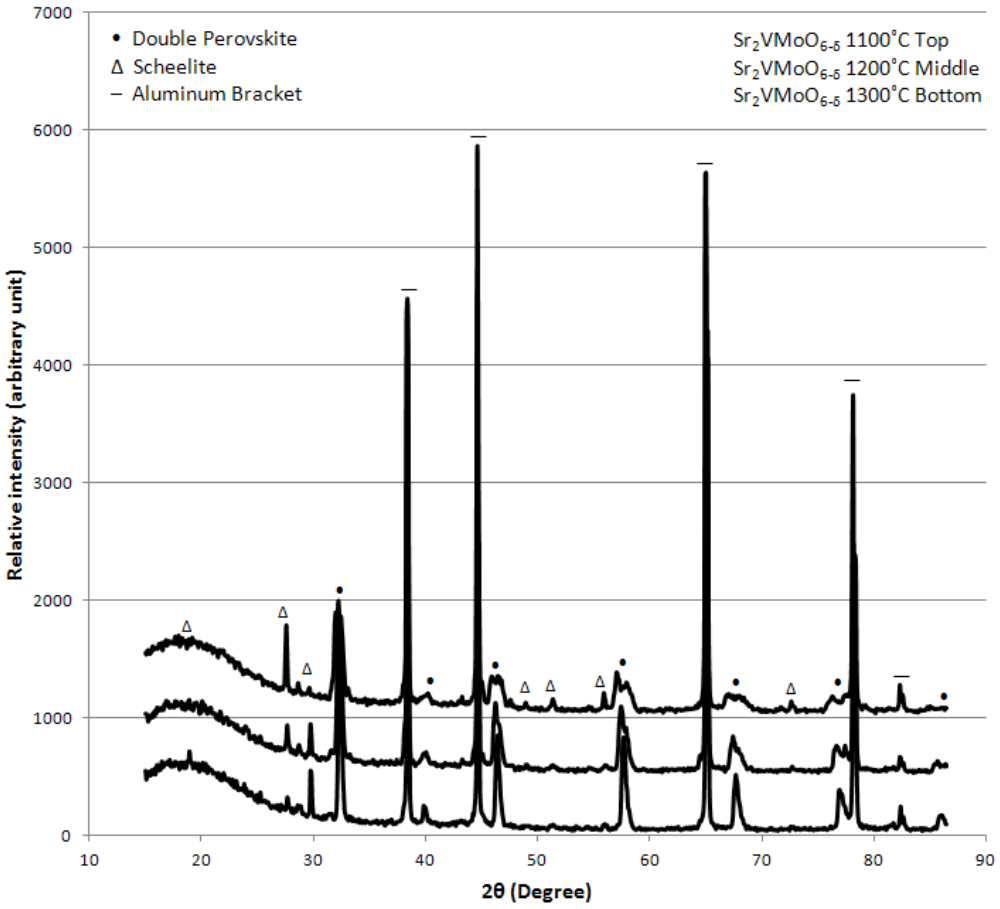


Figure 11: XRD pattern for $Sr_2VMoO_{6-\delta}$ sintered at 1300°C, 1200°C and 1100°C for 20 hours

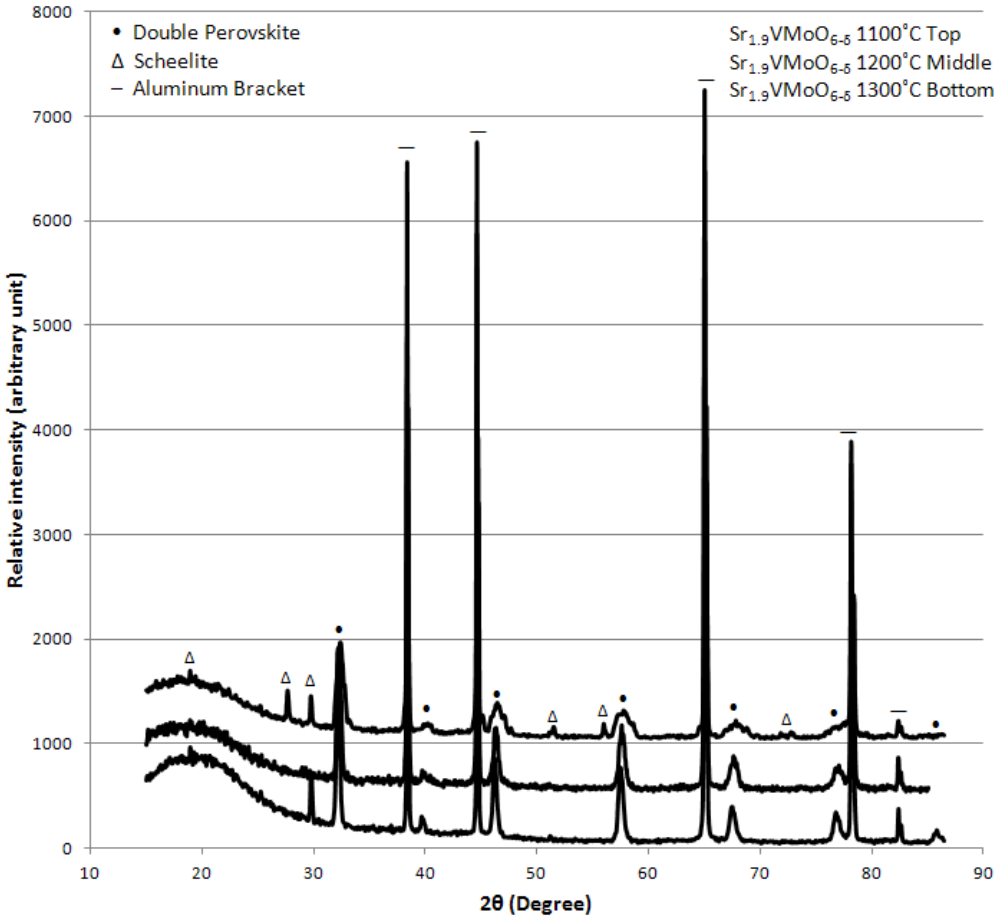


Figure 12: XRD pattern for $Sr_{1.9}VMoO_{6-\delta}$ sintered at 1300°C, 1200°C and 1100°C for 20 hours

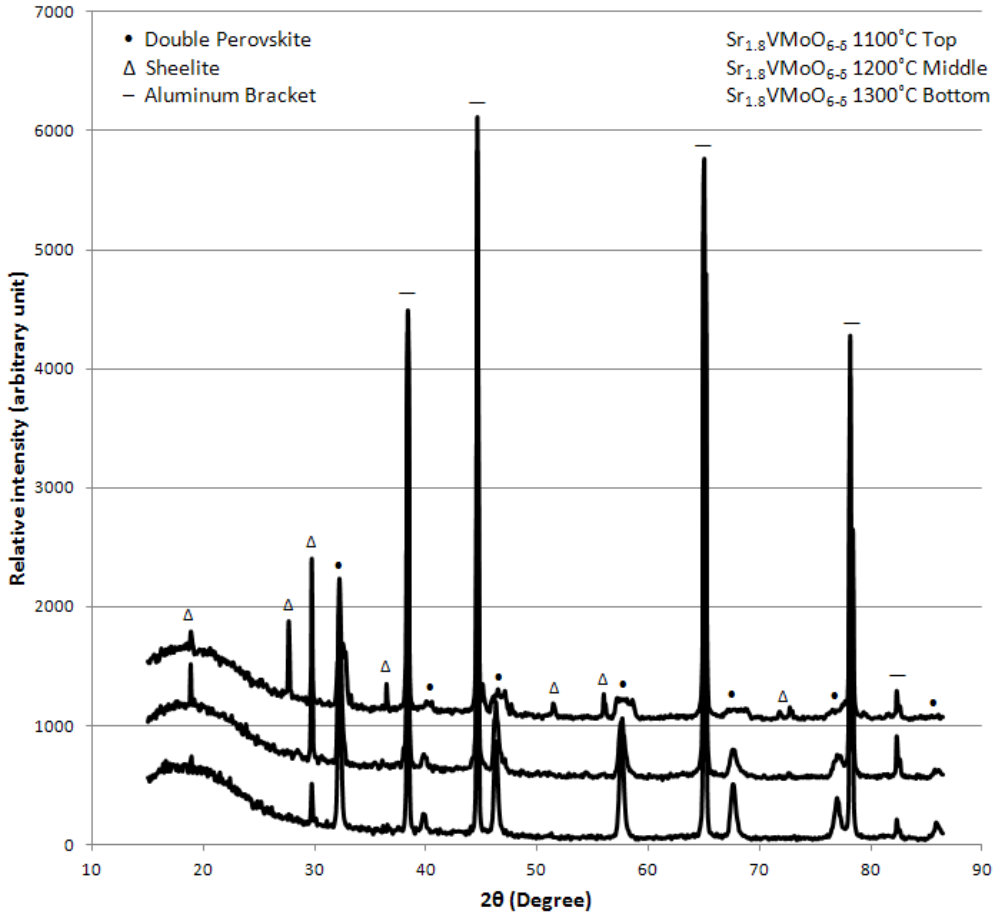


Figure 13: XRD pattern for $Sr_{1.8}VMoO_{6-\delta}$ sintered at 1300°C, 1200°C and 1100°C for 20 hours

3.2 X-ray Photoelectron Spectroscopy (XPS)
and Rutherford Backscattering Analysis (RBS)

XPS was utilized on the sintered pellets to determine the elemental percentages at a depth of approximately 1 nanometer. Figure 14 represents an XPS survey spectrum used for this compositional analysis. XPS revealed a deficiency of vanadium on the pellet surfaces, as shown in Table 2, as 8 out of 9 samples had surface vanadium elemental contents of less than 5%. The average elemental composition over all samples analyzed was found to be 24.8%, 4.2%, 11.8%, and 59.2% for Sr, V, Mo, and

O, respectively. No significant trends were identified with different starting compositions or with different sintering temperatures; however it is important to note that up to 10% error can be expected in compositional analysis via XPS.

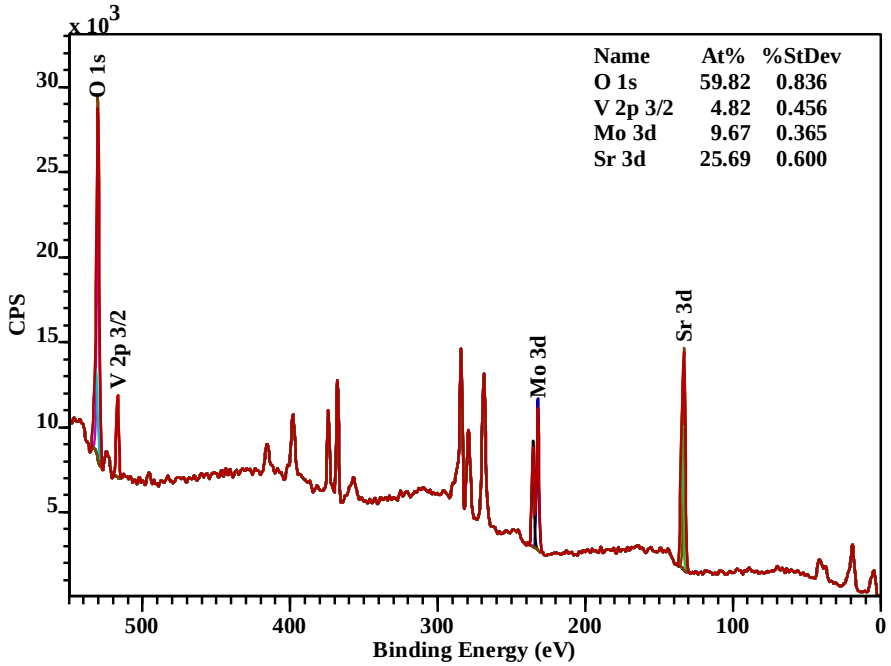


Figure 14: XPS pattern for $Sr_2VMoO_{6-\delta}$ sintered at 1300°C 20 hours

Table 2: Elemental percentages at the surface of $Sr_{2-x}VMoO_{6-\delta}$ sintered pellets as determined by XPS

$Sr_{2.0}VMoO_6$	Sintering Temperature (^{0}C)	Sr(%)	Mo(%)	V(%)	O(%)
	1300	25.6	9.6	4.8	60.0
	1200	28.1	12.2	3.8	56.0
	1100	24.7	12.1	3.1	60.1
$Sr_{1.9}VMoO_6$	Sintering Temperature (^{0}C)	Sr(%)	Mo(%)	V(%)	O(%)
	1300	22.2	15.4	2.7	59.7
	1200	24.4	10.4	4.5	60.8
	1100	24.7	12.9	2.4	60.1
$Sr_{1.8}VMoO_6$	Sintering Temperature (^{0}C)	Sr(%)	Mo(%)	V(%)	O(%)
	1300	25.7	10.9	8.5	54.9
	1200	23.7	11.0	4.3	61.0
	1100	23.7	11.9	4.0	60.4

XPS was also used to analyze the chemical shifts and valence states of $Sr_{2-x}VMoO_{6-\delta}$ tape cast samples. The Sr 2p region of the 1100 ^{0}C sample exhibits two phases, thought to be strontium carbonate and strontium in a perovskite-like phase, as shown in Figure 15. The percent composition of these phases, determined by fitted area ratios of the Sr 2 $p_{3/2}$ region, is 27% and 73% for the carbonate-like and perovskite-like phases, respectively. The Sr 2p region of the 1300 ^{0}C sample exhibits a main phase, 91% of the 2 $p_{3/2}$ peak, consistent with a perovskite-like phase, with the remaining assumed to be the carbonate phase (33; 34). The Mo 3d regions of both samples exhibit a mix of valence states, ranging from Mo(VI) to Mo(0). The Mo valence states for the 1300 ^{0}C sintered sample are dominated by Mo(VI) and Mo(IV), 76.9% and 18.5% respectively. The 1100 ^{0}C sintered sample is also dominated by the same Mo(VI)/Mo(IV) valence states (87.7%/11.2%). The Mo(VI) state in the 1100 ^{0}C samples exhibits two chemical components, one $3d_{5/2}$ component at a binding energy (BE) of 232.1 eV and another at a BE of 233.9 eV making up 53.5% and 34.2% of the total Mo $3d_{5/2}$ signal respectively (35). At this time the authors are unable to find a similar reference to a Mo $3d_{5/2}$ peak at this higher BE. This higher BE Mo(VI) state is not present in the 1300 ^{0}C sintered sample. The O1s peak for the 1100 ^{0}C sintered sample was broader than the 1300 ^{0}C sample, consisting of 47% at 530.0 eV and 53% at 531.8 eV. The 1300 ^{0}C sample O 1s region was split between 63% at 530.0 eV and 37% at 531.8 eV. The binding energy for O 1s in perovskite oxides has been reported to be between 529.8 eV and 530.2 (36). The 1100 ^{0}C vanadium region was fit to two charge state $2p_{3/2}$ contributions, one with a BE of 517.0 eV and another with a BE of 519.0 eV, as shown in Figure 16. These are thought to

be vanadium in a V(V) state (69%) and V(IV) state (31%). The 1300 ^{0}C vanadium region was fit to two charge state $2p_{3/2}$ contributions, one with a BE of 516.9 eV and another with a BE of 514.0 eV. These are thought to be vanadium in a V(IV) state (90%) and V(III) state (10%) (37).

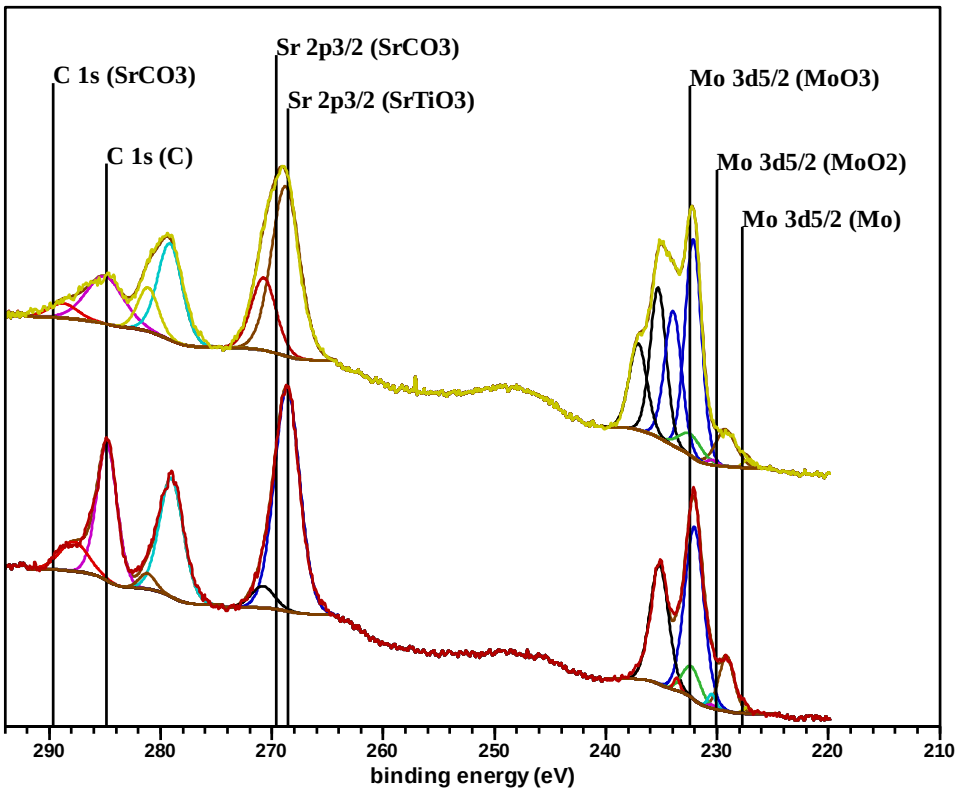


Figure 15: Carbon 1s, Strontium 2p and Molybdenum 3d regions for $Sr_{2.0}VMoO_{6-\delta}$ tape casted samples sintered at 1100 ^{0}C (top) and 1300 ^{0}C (bottom) in a reducing atmosphere ($5\%H_2/95\%N_2$).

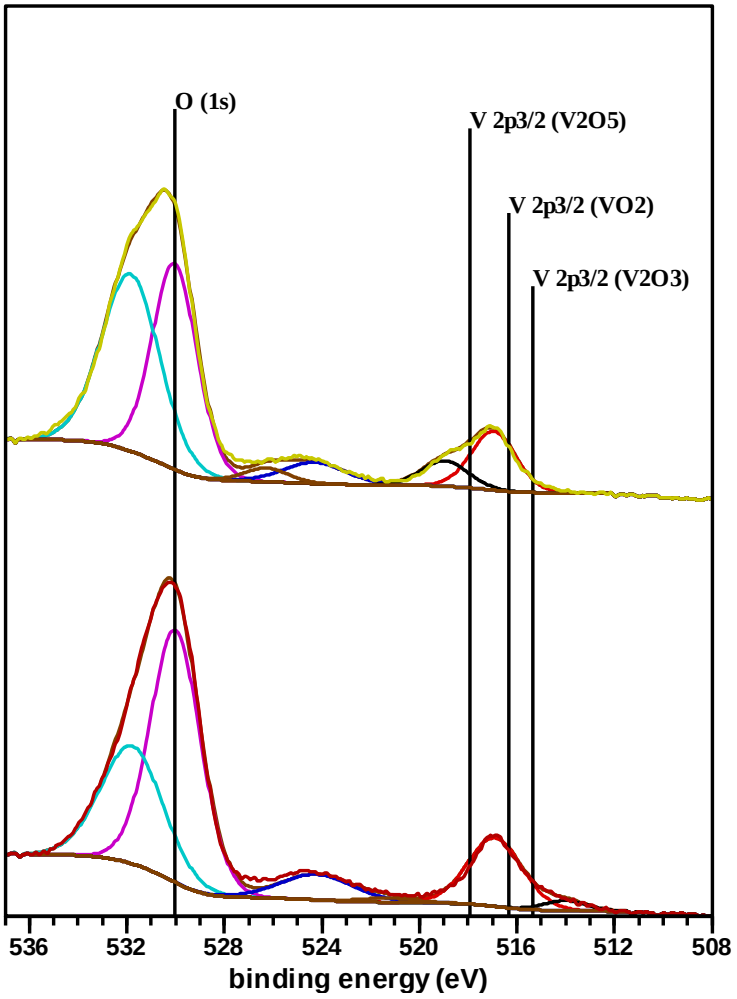


Figure 16: Oxygen 1s and vanadium 2p regions for $Sr_{2.0}VMoO_{6-\delta}$ tape casted samples sintered at 1100 ^{0}C (top) and 1300 ^{0}C (bottom) in a reducing atmosphere (5%H_2/95%N_2)

As shown in Table 3, RBS confirmed the bulk elemental compositions of samples were close to the starting ratios of Sr/Mo/V with the remainder being 60-60.4% O. Simulated bulk stoichiometries of $Sr_{2.0}VMoO_6$, $Sr_{1.9}VMoO_{5.9}$ and $Sr_{1.8}VMoO_{5.8}$ for SR20, SR19 and SR18 samples were in agreement with data from both H^+ and He^+ spectra. For the He^+ beam, Sr and Mo kinematic factors are 0.836 and 0.849 (0.958/0.962 for H^+ beam) respectively, making resolution between Sr and Mo concentrations difficult. A

simulated spectrum for $Sr_{2.0}VMoO_6$ along with the SR20 He^+ RBS spectrum is shown in Figure 17. The non-Rutherford O cross section for the H^+ beam is much larger than that of the Rutherford cross section of He^+, providing a higher signal in the proton spectrum. However, simulations between 58% and 60% oxygen volume contents are within the noise of the spectrum making these contents indistinguishable. A simulated stoichiometry of $Sr_{2.0}VMoO_6$ placed on the SR20 He+ RBS spectrum is shown in Figure 18. A large amount of pile-up is noted above the Sr/Mo edge in the H+ spectrum due to a high beam current, but this is unlikely to affect composition simulations drastically. A simulated spectrum with a carbon content of 3.5% for the first 0.05-0.1 μm on the SR20 NRA spectrum is shown in Figure 19. The carbon content falls off to less than 1% in the bulk. The only signal present in this region comes from the 12C(d,p)13C nuclear reaction. SR19 and SR18 spectra showed similar surface and bulk carbon contents.

Table 3: Elemental percentages at the surface of $Sr_{2-x}VMoO_{6-\delta}$ sintered pellets as determined by RBS

Sample	Strontium	Molybdenum	Vanadium	Oxygen
$Sr_{2.0}VMoO_{6-\delta}$	20%	10%	10%	60%
$Sr_{1.9}VMoO_{6-\delta}$	19.4%	10.2%	10.2%	60.2%
$Sr_{1.8}VMoO_{6-\delta}$	18.8%	10.4%	10.4%	60.4%

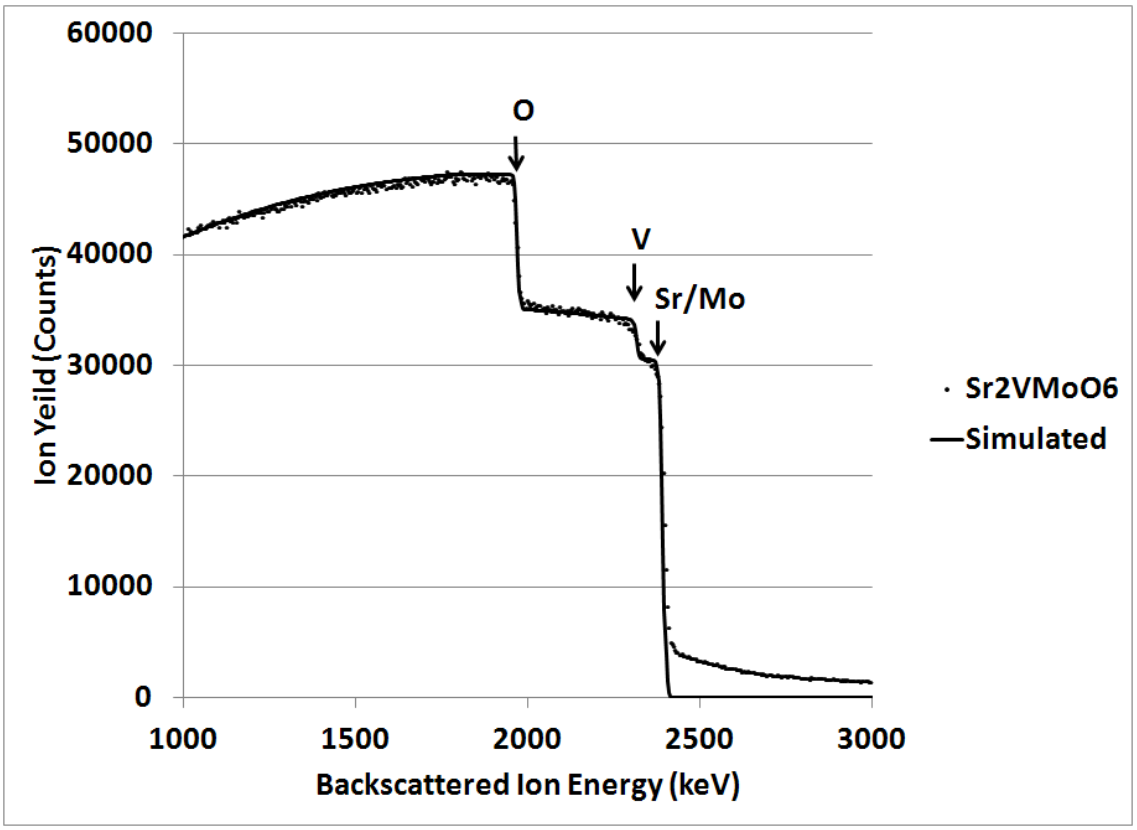


Figure 17: 2.5 MeV H+ RBS spectrum of a $Sr_{2.0}VMoO_{6-\delta}$ tape cast disc sample sintered at 1300 ^{0}C. SIMNRA software was used to simulate a composition of 20% Sr, 10% V, 10% Mo and 60%
O

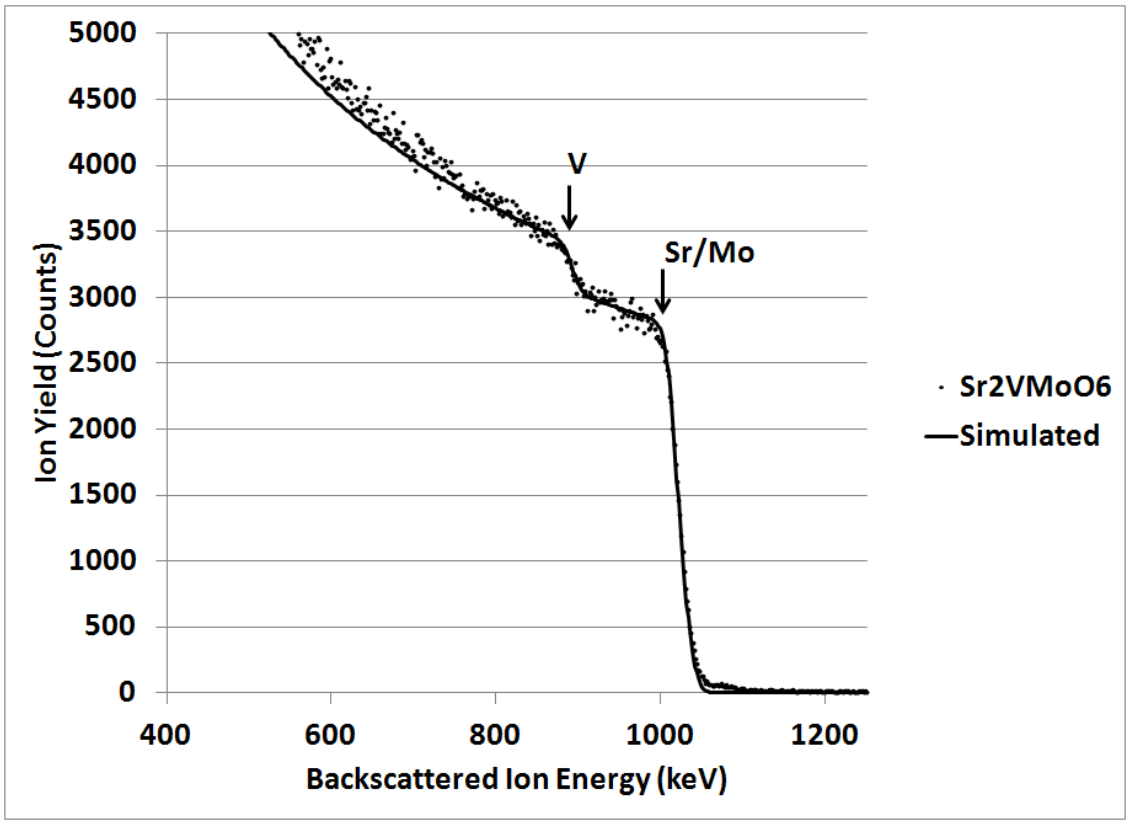


Figure 18: 1.2 MeV He+ RBS spectrum of a $Sr_{2.0-x}VMoO_{6-\delta}$ pressed pellet sample sintered at 1300 ^{0}C. SIMNRA software was used to simulate a composition of 20% Sr, 10% V, 10% Mo and 60% O

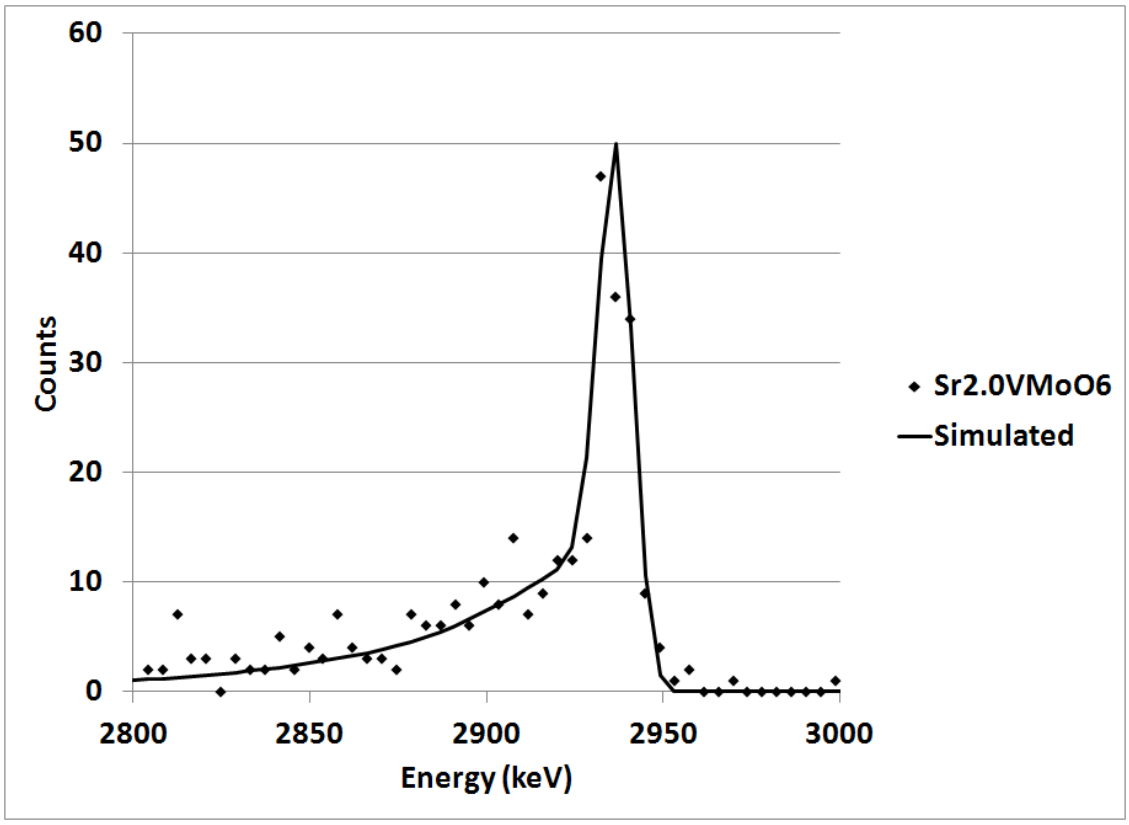


Figure 19: 0.9 MeV D+ NRA spectrum of a $Sr_{2.0}VMoO_{6-\delta}$ sample sintered at 1300 ^{0}C. The spectra indicates a 0.5-0.1 µm carbon surface layer with less than 1% carbon content in the bulk

3.3 Redox Cycling

The redox cycled $Sr_{2-x}VMoO_{6-\delta}$ pellets were cross-sectioned and then analyzed in a FESEM to investigate the change in microstructure due to the cycling of oxygen partial pressures. The original (upper left) microstructure and photo (upper right) of the redox tested pellet and resulting microstructure of $Sr_{1.9}VMoO_{6-\delta}$ is shown in Figure 20. A JEOL JSM-6100 Scanning Electron Microscope (SEM) was used for elemental mapping of the $Sr_{1.9}VMoO_{6-\delta}$ cross-section, as shown in Figure 21. The microstructure indicates that two different layers form during the redox testing of the $Sr_{1.9}VMoO_{6-\delta}$ pellet. The

microstructure of the black colored middle section of the pellet resembles the original microstructure (bottom right); however the white colored outside section shows a high level of coarsening (bottom left). The elemental mapping of the $Sr_{1.9}VMoO_{6-\delta}$ pellet indicates a vanadium rich area at the boundary of the two layers and suggests that vanadium is migrating throughout the pellet. The change in oxygen partial pressure is not a concern if the fuel cell is run in alternating power and electrolysis modes and is properly sealed, but it could affect the double perovskite adversely if exposed to air at fuel cell operating temperature, which could happen if the fuel supply is not sufficient for high fuel cell power demands (38).

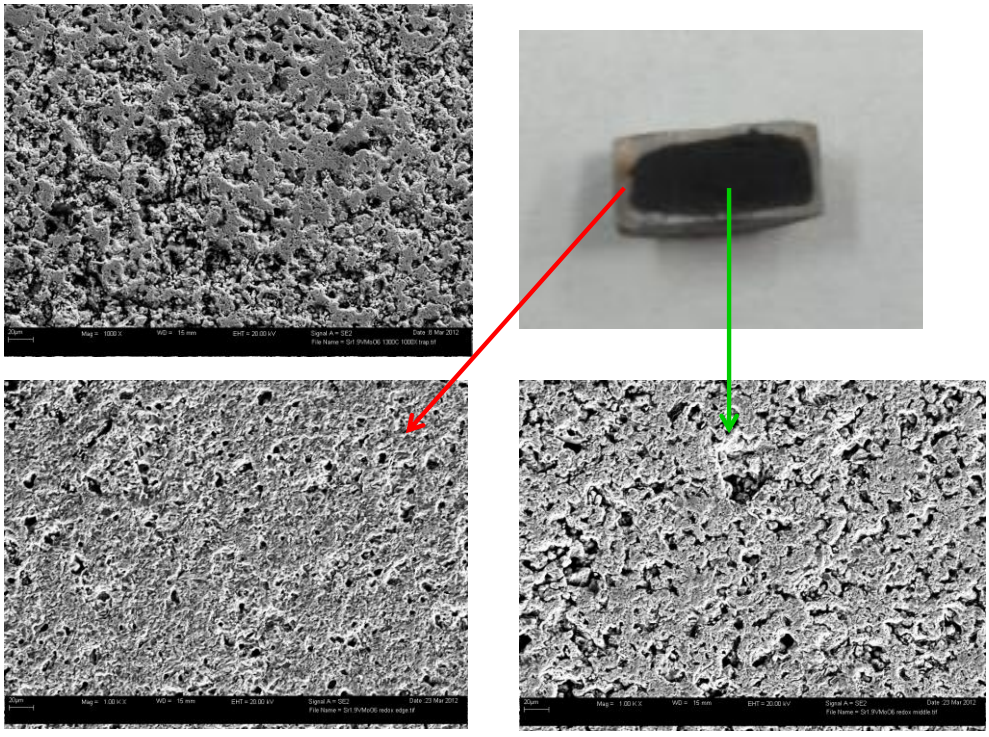


Figure 20: FESEM microstructure images of an original sintered $Sr_{1.9}VMoO_{6-\delta}$ pellet (upper left) and a redox tested $Sr_{1.9}VMoO_{6-\delta}$ pellet (bottom two images). Arrows indicate outside and inside sections of the pellets to the corresponding microstructure

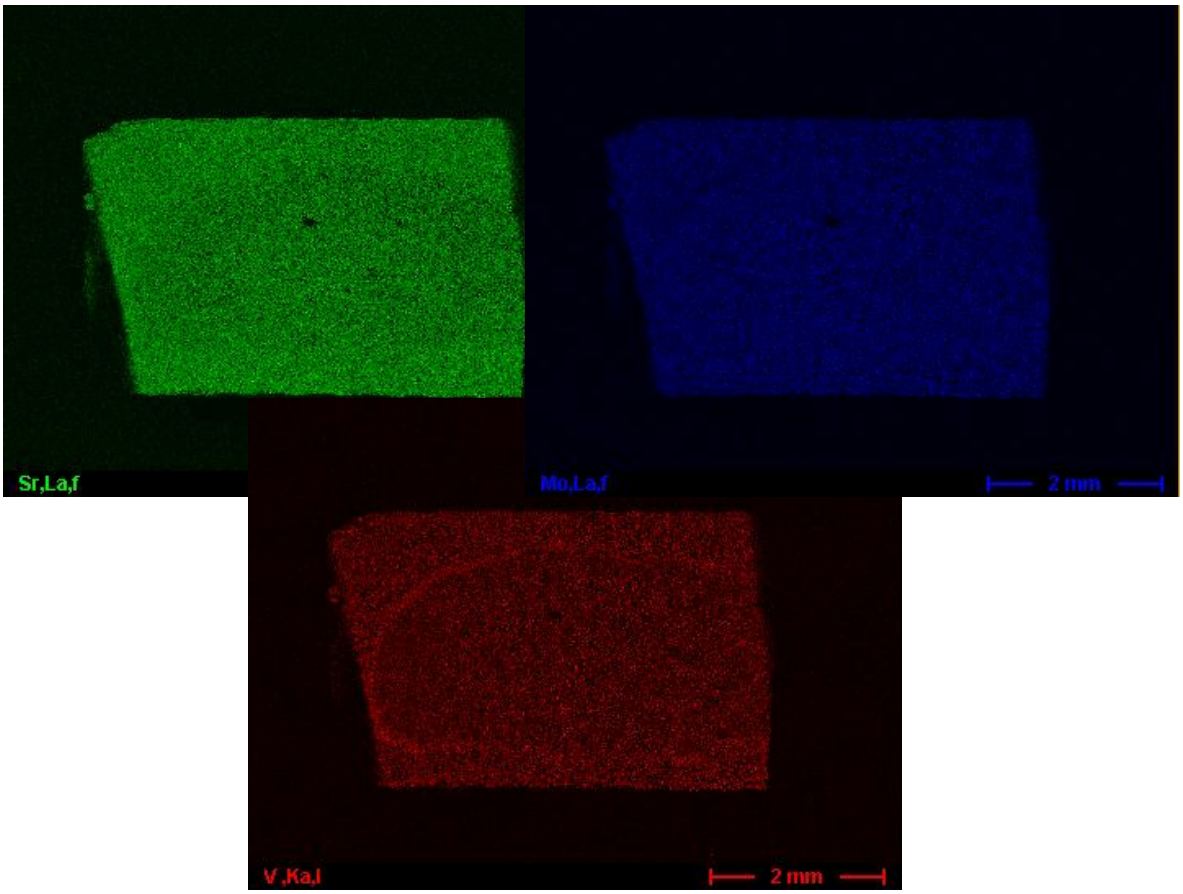


Figure 21: SEM elemental imaging of a $Sr_{1.9}VMoO_{6-\delta}$ redox tested pellet, where top left, top right, and bottom pictures represent Sr, Mo, and V, respectively

3.4 Microstructure and Micro-Hardness Testing

FESEM images of the microstructure of $Sr_{2-x}VMoO_{6-\delta}$ pellets at a magnification of 1000X are shown in Figures 22, 23, and 24. $Sr_2VMoO_{6-\delta}$ pellets sintered at 1200°C and 1100°C for 20 hours have very similar microstructures and very similar amounts of porosity, as shown in Table 4. However, the $Sr_2VMoO_{6-\delta}$ pellet sintered at 1300°C for 20 hours exhibits much more densification with reduction in porosity. The $Sr_{1.9}VMoO_{6-\delta}$ sintered pellets showed a much different microstructure than the $Sr_2VMoO_{6-\delta}$ sintered

pellets. Further, the $Sr_{1.9}VMoO_{6-\delta}$ pellet sintered at 1200°C has a much different microstructure and porosity than the pellets sintered at the two other temperatures, which could correspond to the apparent elimination of the spinel structure observed by XRD analysis. The microstructure of the $Sr_{1.8}VMoO_{6-\delta}$ sintered pellets is similar to the $Sr_2VMoO_{6-\delta}$ sintered pellets and also exhibited higher densification at the higher sintering temperatures. As shown in Table 4, $Sr_2VMoO_{6-\delta}$ showed the highest yield strength for all of the tested pellets when sintered at 1300˚C, however exhibits a drastic drop in yield strength for the 1200˚C and 1100˚C sintered pellets. This is not the same phenomena observed for $Sr_{1.9}VMoO_{6-\delta}$, where the pellets sintered at 1300˚C and 1200˚C exhibit similar yield strength and are much greater than the 1100˚C sintered pellet; however the $Sr_{1.8}VMoO_{6-\delta}$ pellets show a steady decline in strength at the sintering temperature is decreased. The average yield strength of 260.8 MPa, with an average porosity of 40.4%, for all of the $Sr_{2-x}VMoO_{6-\delta}$ pellets corresponds favorably to published values of 61.5-88.5 MPa, with a porosity of 26.3-43.0%, of traditional Ni/YSZ cermets (39). The high strength of the $Sr_2VMoO_{6-\delta}$ sintered pellets observed during hardness testing indicates that the double perovskite would be more effective when utilized in a fuel electrode supported SOFC.

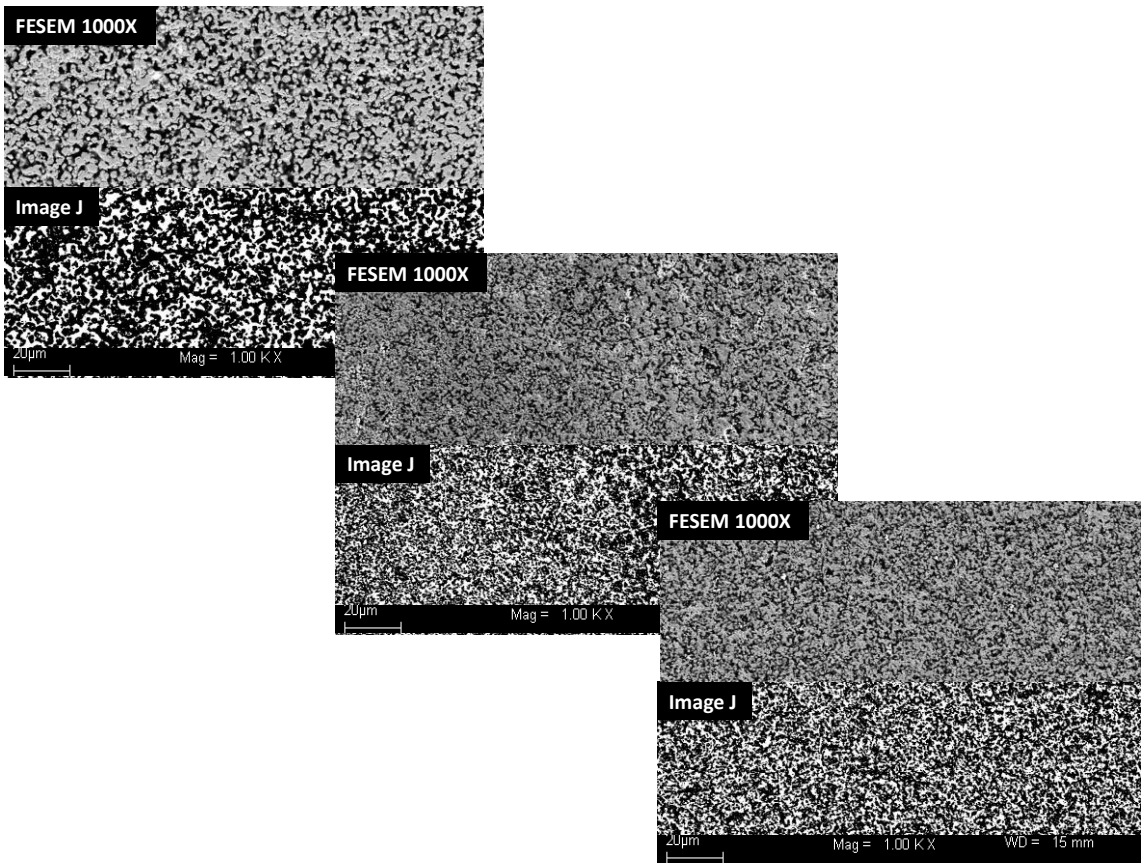


Figure 22: FESEM/ ImageJ Binary microstructure image of the 1300˚C, 1200˚C, and 1100˚C (top left to bottom right) sintered $Sr_2VMoO_{6-\delta}$ pellets

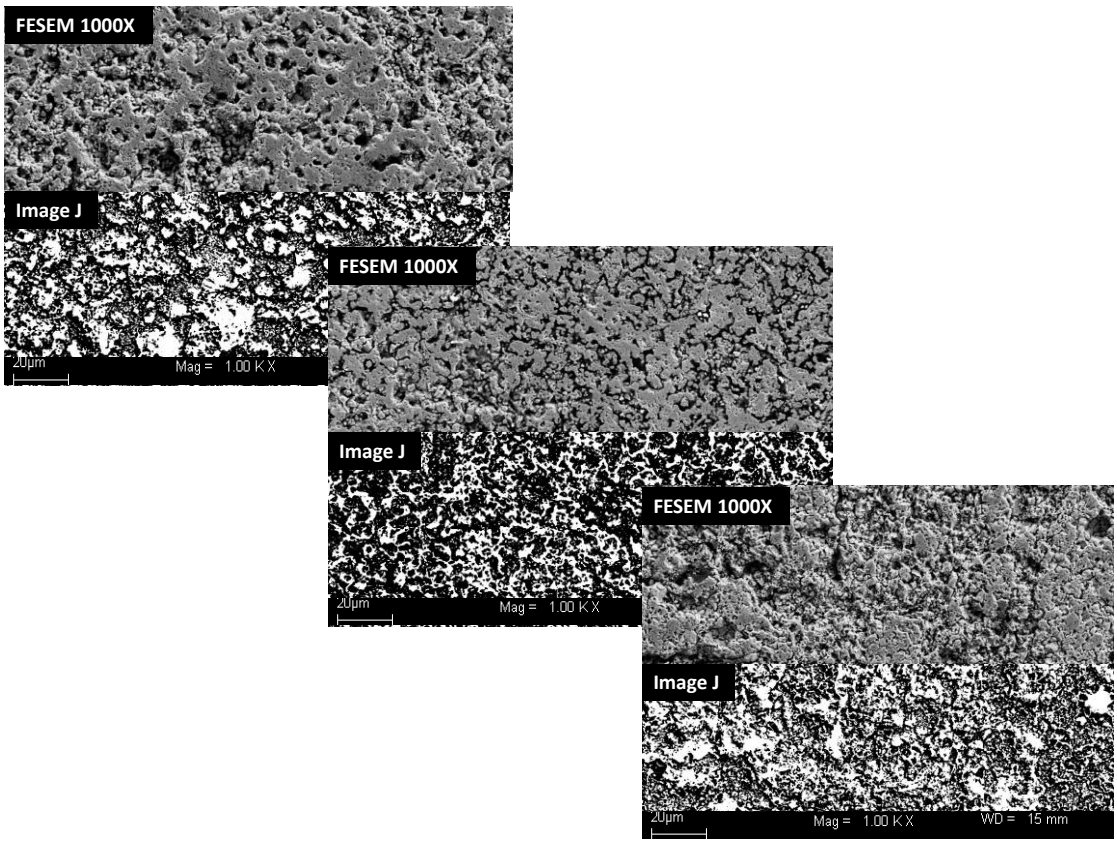


Figure 23: FESEM/ ImageJ Binary microstructure image of the 1300˚C, 1200˚C, and 1100˚C (top left to bottom right) sintered $Sr_{1.9}VMoO_{6-\delta}$ pellets

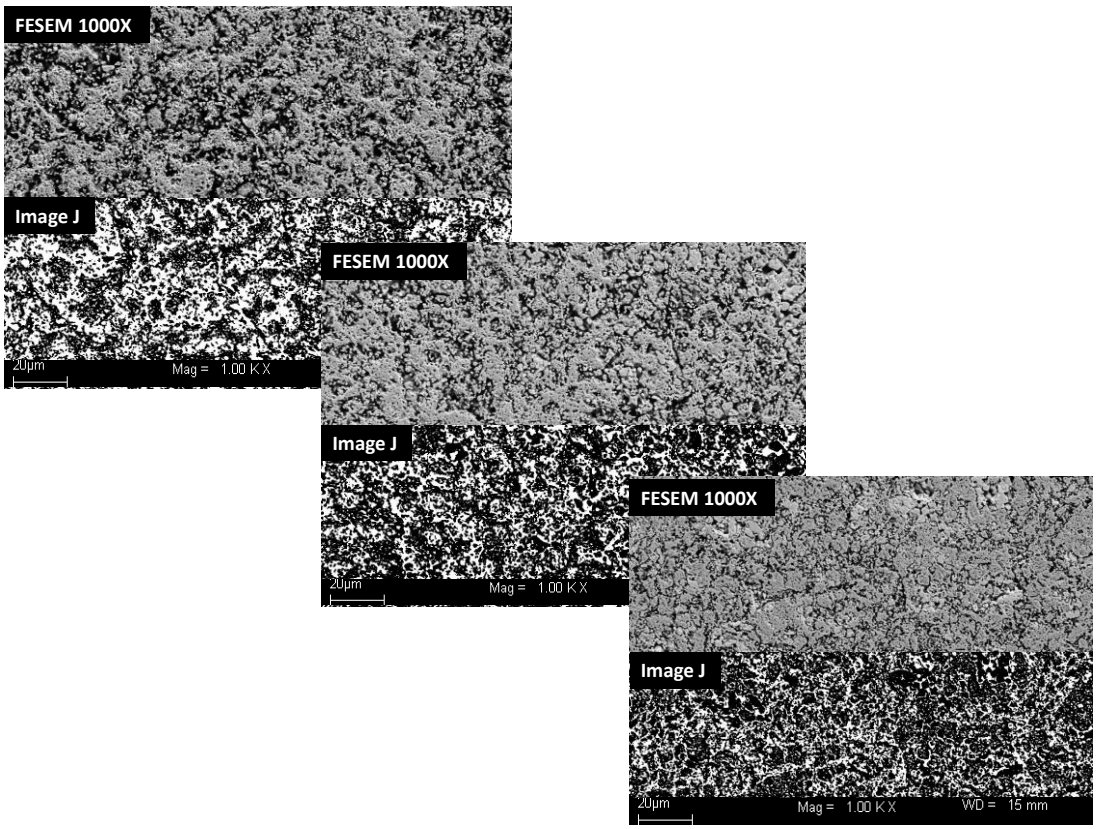


Figure 24: FESEM/ ImageJ Binary microstructure image of the 1300˚C, 1200˚C, and 1100˚C (top left to bottom right) sintered $Sr_{1.8}VMoO_{6-\delta}$ pellets

Table 4: Yield strength and porosity of $Sr_{2-x}VMoO_{6-\delta}$ sintered pellets

Sintering Temp (˚C)	Compound	Yield Strength (Mpa)	Porosity (%)
1300	$Sr_2VMoO_{6-\delta}$	391	35.3
	$Sr_{1.9}VMoO_{6-\delta}$	365	44.8
	$Sr_{1.8}VMoO_{6-\delta}$	259.2	45.8
1200	$Sr_2VMoO_{6-\delta}$	206.6	41.8
	$Sr_{1.9}VMoO_{6-\delta}$	332.4	35.0
	$Sr_{1.8}VMoO_{6-\delta}$	217.9	38.1
1100	$Sr_2VMoO_{6-\delta}$	205.2	41.7
	$Sr_{1.9}VMoO_{6-\delta}$	166.6	47.9
	$Sr_{1.8}VMoO_{6-\delta}$	203	33.2

3.5 DC Resistivity Testing

As shown in Figures 25, 26, and 27, $Sr_{2-x}VMoO_{6-\delta}$ pellets sintered at 1300°C showed the lowest resistivity at both Solid Oxide Fuel Cell (SOFC) operating temperature (800°C) and room temperature after cooling from 800°C. The minimum resistivity for $Sr_2VMoO_{6-\delta}$ was $7.965*10^{-7}\Omega*m$. The minimum resistivity for $Sr_{1.9}VMoO_{6-\delta}$ was $6.124*10^{-7}$ $\Omega*m$ and the minimum resistivity for $Sr_{1.8}VMoO_{6-\delta}$ was $4.43910^{-7}\Omega*m$. These resistivity values correspond well to the values published by Karen et al. (18), where the maximum conductivity for $Sr_2VMoO_{6-\delta}$ differs by 4% from the published room temperature values. The $Sr_2VMoO_{6-\delta}$ pellets show a significant difference in resistivity at 800°C between all three sintering temperatures. This can be attributed to a reduction in porosity and the reduction of the scheelite structure associated with change in sintering temperature. The $Sr_{1.9}VMoO_{6-\delta}$ pellets exhibit very similar resistivities for 1300°C and 1200°C sintering temperatures, which also can be explained from formation of the double perovskite phase.

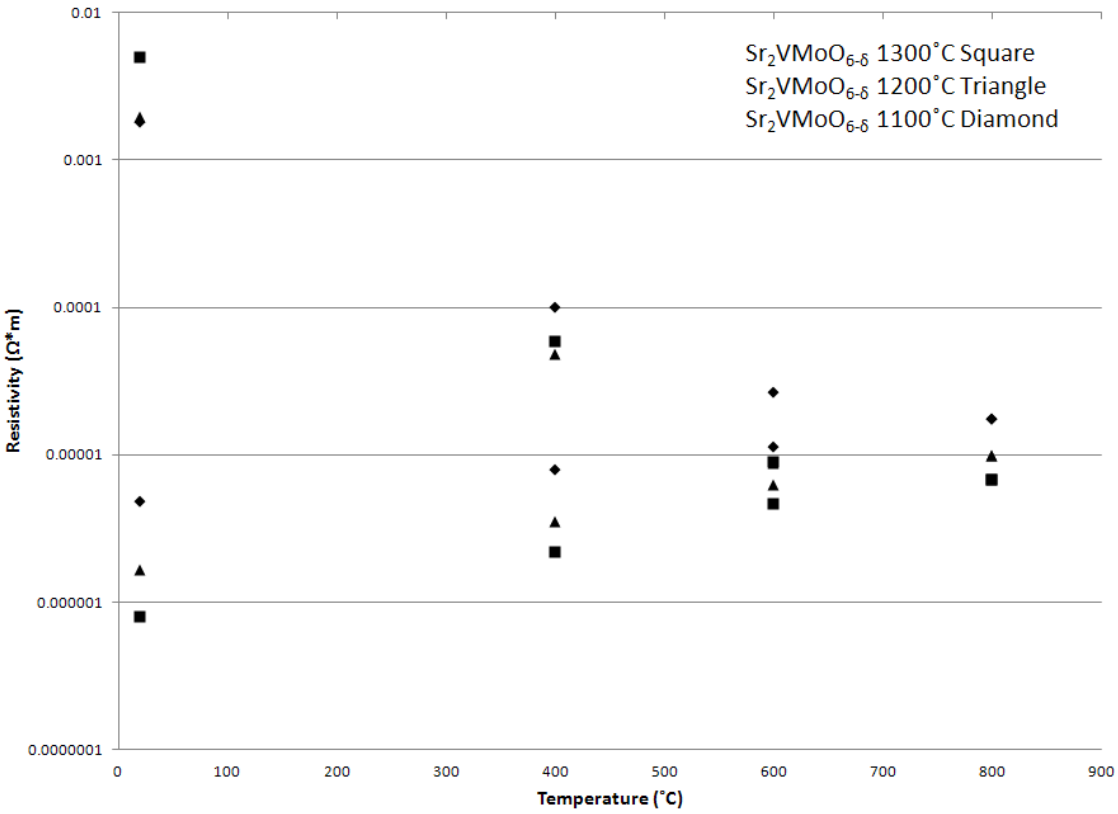


Figure 25: Resistivity vs. Temperature for sintered $Sr_2VMoO_{6-\delta}$ pellets

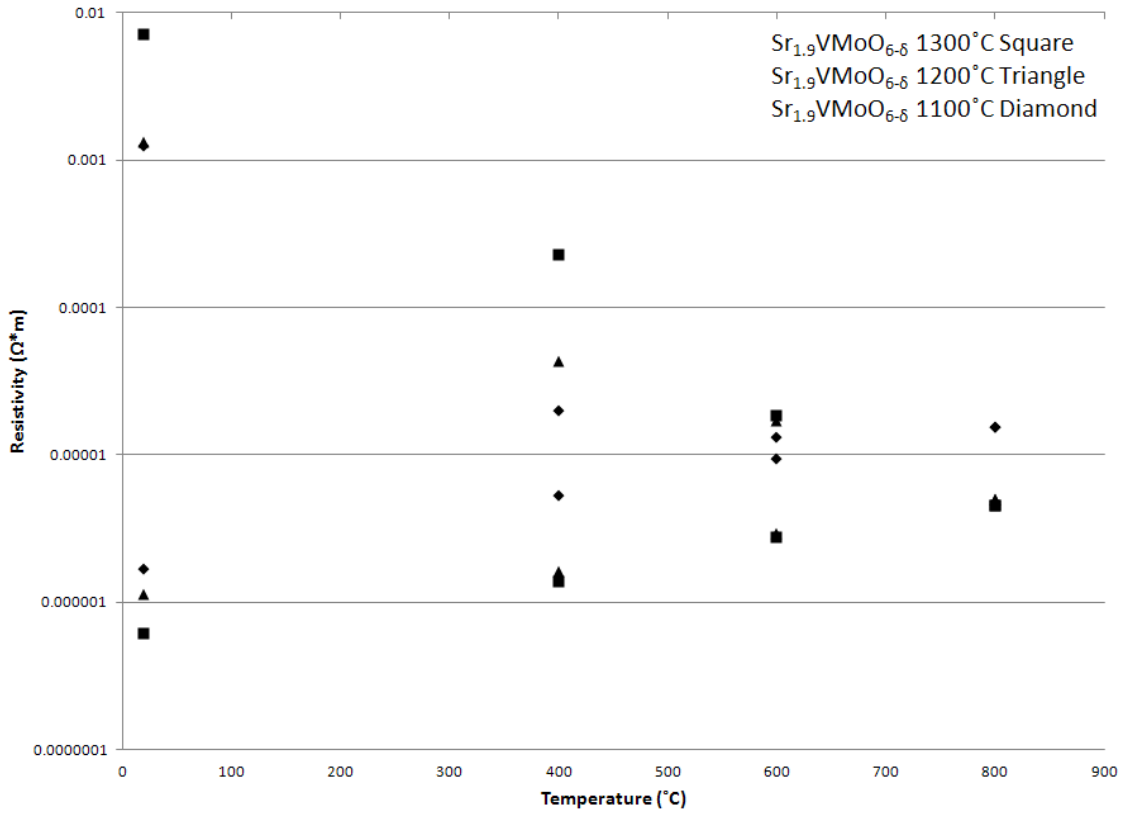


Figure 26: Resistivity vs. Temperature for sintered $Sr_{1.9}VMoO_{6-\delta}$ pellets

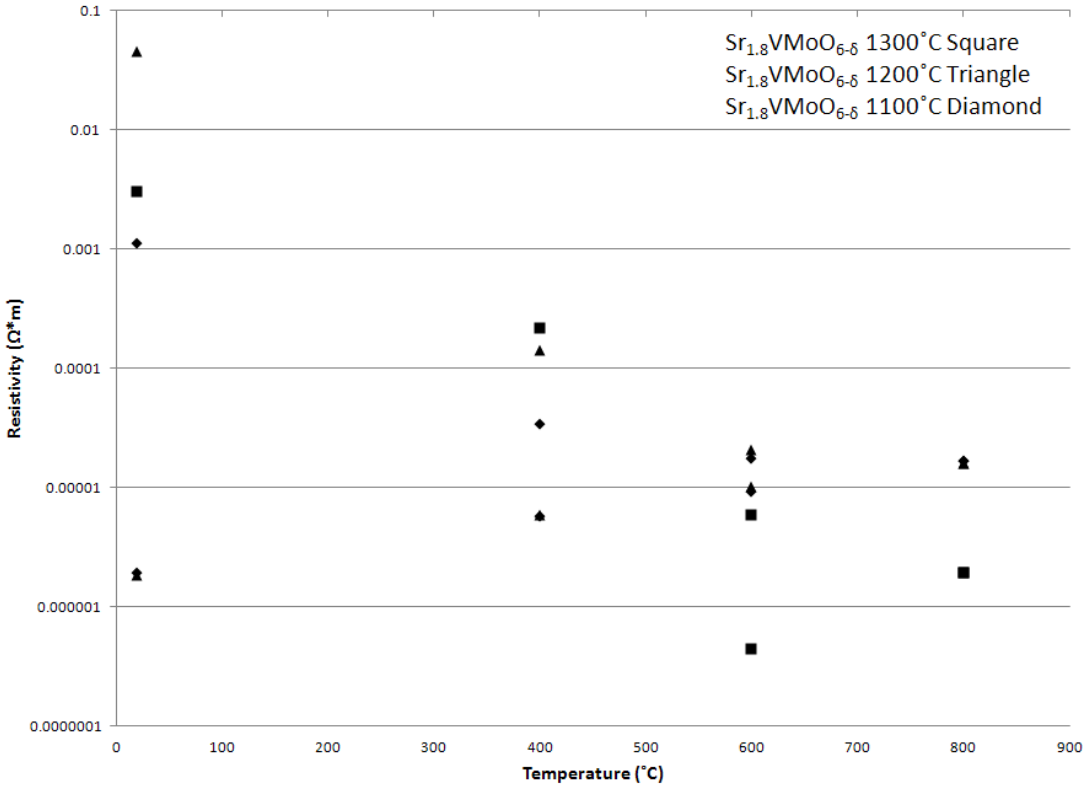


Figure 27: Resistivity vs. Temperature for sintered $Sr_{1.8}VMoO_{6-\delta}$ pellet

4. Discussion

4.1 Formation of the Double Perovskite Structure

The observed amounts of Mo(IV), Mo(VI), V(IV), and V(V) valence states from XPS, for the b-site cation species, provides some understanding on the formation of the Scheelite and double perovskite structures. The corresponding ionic radii are 0.58Å, 0.59Å, 0.65Å, and 0.54Å, for Mo(IV), Mo(VI), V(IV), and V(V) valence states, respectively. This would indicate that both Mo(IV) and Mo(VI) could substitute into the $SrVO_3$ B-site. However, the b-site cations in the double perovskite structure have a total charge of 8^+, which is only achievable with Mo(IV) and V(IV) out of the valence states observed during XPS analysis. These valence states would correspond to a Goldschmidt tolerance factor (Equation 5) of .994, which is acceptable for a cubic structure; however the low elemental percentage of V and high amount Mo(IV) at the surface of the material would indicate that a low amount of double perovskite exists at the surface of the pellet.

Equation 5: $(\boldsymbol{R_A + R_O})/\sqrt{\boldsymbol{2}}(\boldsymbol{R_B + R_O})$ [24]

Note: R_A=A-site ionic radii, R_o=Oxygen ionic radii, and R_B=Average B-site ionic radii

The low amount of the perovskite phase at the surface and higher amount in the bulk of the material can be explained from the slow reduction of Mo(VI) to Mo(IV) and the rapid oxidation of Mo(IV) to Mo(VI), therefore forming the scheelite phase rapidly at the surface of the pellet (29). The formation of $SrMoO_{4-\delta}$ at the surface could lead to the decomposition of $Sr_2VMoO_{6-\delta}$ and therefore lead to vanadium migration towards the bulk of the material. This migration corresponds to the low elemental percentage found from

surface sensitive XPS and the concentrated vanadium layer in the bulk of the material caused by high temperature oxidation during redox cycling. Kuepper et al. (40) also found that $Sr_2FeMoO_{6-\delta}$ decomposes in air to $SrMoO_{4-\delta}$ at the surface and $SrFeO_{3-\delta}$ at the lower levels, resulting in a Fe deficiency at the surface of the material. The reduction of Mo(VI) to the Mo(IV) valence state is the driving factor for the substitution of molybdenum on the vanadium site in the already formed perovskite, which indicates that a reducing atmosphere, high temperature, and long dwell time is needed to fully develop the double perovskite structure. This corresponds to the finding of Fang et al. (41) and Aguadero et al. (42), where $SrMoO_4$ was found during processing of Sr_2FeMoO_6 and Sr_2CoMoO_6, respectively. Further, Fang et al. (41) were able to form more of the double perovskite phase at higher sintering temperatures in a reducing atmosphere.

4.2 Resistivity of $Sr_{2-x}VMoO_{6-\delta}$ Double Perovskites

The total electrical conductivity of the $Sr_{2-x}VMoO_{6-\delta}$ double perovskites including both ionic and electronic contributions is driven by defects associated with attaining charge neutrality through both dopant additions as well as oxygen concentration. This in turn yields anion vacancies that facilitate oxygen ion transport, changes in cation oxidization that yield both polarons and free electrons. Polaron hopping occurs when the negatively charged polaron on the multivalent cation M^{4+} site jumps to the M^{3+} site, where M represents V or Mo for $Sr_{2-x}VMoO_{6-\delta}$. This process continues throughout the material as long as multiple oxidation states are present. Electronic conductivity produced by charge neutrality is further demonstrated by Equations 6 through 8, where the reduction of the b-site cations (V or Mo in this study) is shown in Kroger-Vink

notation. Equations 6 and 7 represent the reduction of vanadium with a 4+ oxidation state to 3+ and 2+ oxidation states, therefore producing one and two oxygen vacancies, respectively. These vacancies can generate ionic conduction and also, through charge neutrality, produce free electrons as shown in Equation 8. Equations 6 and 7 represent the possible defect scenarios of the b-site reduction, however based on the results of this study and the findings of Fotiev el al. (43), the vanadium and molybdenum 4+ states are more conductive than the vanadium 3+ and molybdenum 5+ combination. The oxygen vacancies are not limited to the reduction of b-site cations and can be produced in much of the same way by reducing the amount of a-site cations. The sub-stoichiometry would lead to oxygen vacancies, due to charge neutrality as shown in Equations 9.

Equation 6: $2(\mathrm{M} + O_2) \rightarrow 2\mathrm{M}'_{\mathrm{M}} + \mathrm{V}_O^{**} + 4O_O^X$

Equation 7: $\mathbf{M} + \boldsymbol{O_2} \rightarrow \mathbf{M}''_{\mathbf{M}} + \mathrm{V}_{\boldsymbol{O}}^{**} + \mathbf{2}\boldsymbol{O}_{\boldsymbol{O}}^{\boldsymbol{X}}$

Equation 8: $\boldsymbol{O}_{\boldsymbol{O}}^{\boldsymbol{X}} \rightarrow \mathbf{1/2}\boldsymbol{O_2 gas} + \mathrm{V}_{\boldsymbol{O}}^{**} + \mathbf{2}\boldsymbol{e}^{-}$

Equation 9: $[\boldsymbol{V}''_{\boldsymbol{sr}}] = [\mathrm{V}_{\boldsymbol{O}}^{**}]$

Note: $\mathrm{M} = \mathrm{V}, and\ \mathrm{Mo}$, V = Vacancy, ‘ = negative charge, * = positive charge, and ^{X} = neutral charge

The resistivity tests performed in a reducing atmosphere exhibit semiconductor behavior when the double perovskite is heated up to 800°C; however metallic behavior is observed when the pellets are cooled to room temperature from 800°C. The small resistance at lower temperatures in a reducing environment was reported by both Karen et al. (18) and Aguadero et al. (44), however the resulting conductivity was much higher than the results found by Aguadero et al. (44), This can also be explained through the reduction of Mo6+ to Mo4+ in the reducing atmosphere during the resistivity testing. As found by Katrib et al. (29), molybdenum trioxide (MoO_3) will start to reduce to

molybdenum dioxide in an hour of exposure to a reducing environment at 350°C which will contribute to free Mo 4d and Mo5s electrons that can exhibit metallic conductivity. This is further validated by the XRD and conductivity tests, where $Sr_{2-x}VMoO_{6-\delta}$ pellets sintered at 1300°C for 20hr exhibit the lowest resistivity and shows the double perovskite as its main phase. This suggests that the greatest conductivity can only be achieved by extending the sintering time and temperature parameters to try and facilitate the desired double perovskite structure.

5. Conclusions

The XRD patterns indicate that the double perovskite is the primary phase for $Sr_{2-x}VMoO_{6-\delta}$ pellets sintered at 1200°C and 1300°C for 20 hours; however, these pellets show a secondary phase of $SrMoO_{4-\delta}$. These tests indicate that the phase pure double perovskite $Sr_{2-x}VMoO_{6-\delta}$ structure can only be achieved in a reducing atmosphere at high temperatures (1300˚C) and the $SrBO_{4-\delta}$ scheelite phase is the main phase at lower temperatures and oxidizing atmospheres. Thus studies evaluating this or other double perovskites that utilize molybdenum must be cautious of processing conditions that are insufficient to yield phase pure materials. XPS revealed a deficiency of vanadium on the pellet surfaces, as 8 out of 9 samples had surface vanadium contents of less than 5% and the average composition over all samples analyzed was found to be 24.8%, 4.2%, 11.8%, 59.2% for Sr, V, Mo, O, respectively. The low vanadium concentration can be explained by the formation of the $SrMoO_{4-\delta}$ scheelite phase due to oxygen exposure on the surface of the pellets, which indicates vanadium migration to the bulk, and was exhibited in

redox cycling. RBS confirmed the bulk elemental compositions of samples were close to the starting ratios of Sr/Mo/V with the remainder being 58-64% O.

$Sr_{2-x}VMoO_{6-\delta}$ pellets exhibited an average yield strength of 260.8 MPa, which corresponds favorably to published values of 61.5-88.5 MPa of traditional Ni/YSZ cermets (39). The high strength of the $Sr_2VMoO_{6-\delta}$ sintered pellets observed during hardness testing indicates that the double perovskite should be sufficiently strong for the fabrication of fuel electrode supported SOFC. $Sr_{2-x}VMoO_{6-\delta}$ pellets sintered at 1300°C showed the lowest resistivity at both SOFC operating temperature (800°C) and room temperature after cooling from 800°C. This can be attributed to a reduction in porosity and the reduction of the insulating scheelite structure associated with change in sintering temperature. The resistivity tests also show a semiconductor to metallic transition for all double perovskites from heating up to 800°C to cooling down to room temperature in a reducing atmosphere. The metallic transition is indicated to be a result of the reduction of Mo6+ to Mo4+ in the reducing atmosphere during the resistivity testing, therefore liberating Mo 4d and Mo5s electrons.

Future efforts will consist of investigating the mechanisms of conductivity by utilizing temperature segmented conductivity testing, thermal gravimetric analysis, and temperature controlled in-situ XPS to further demonstrate the temperature at which reduction occurs as well as how cation oxidation states influence the observed conductivity.

Acknowledgments

This work was supported by NASA EPSCoR under grant #NNX09AP73A

Supplemental Material for "Processing and Characterization of Sr2-xVMoO6-δ Double Perovskites"

The secondary scheelite phase found in XRD testing is an ABO_4 structure, as shown in Figure 28. XRD analysis also indicated that a scheelite $SrWO_4$ structure was the secondary phase for the initially investigated $Sr_2VWO_{6-\delta}$ double perovskites, as shown in Figure 29. The scheelite structure was sintered, utilizing $SrMoO_4$ Alfa Aesar powders, and conductivity tests were performed. The results from this testing indicated that the $SrMoO_4$ structure is electrically insulating.

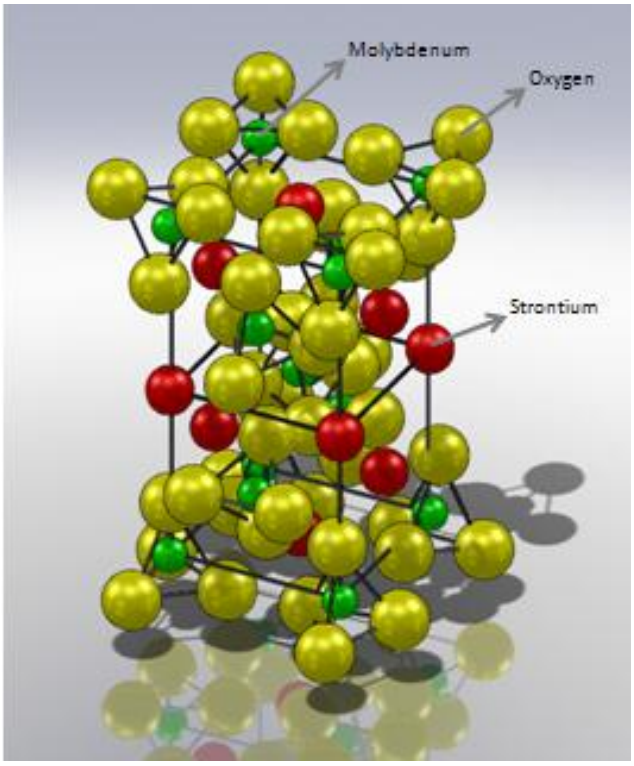


Figure 28: Representation of the Scheelite structure

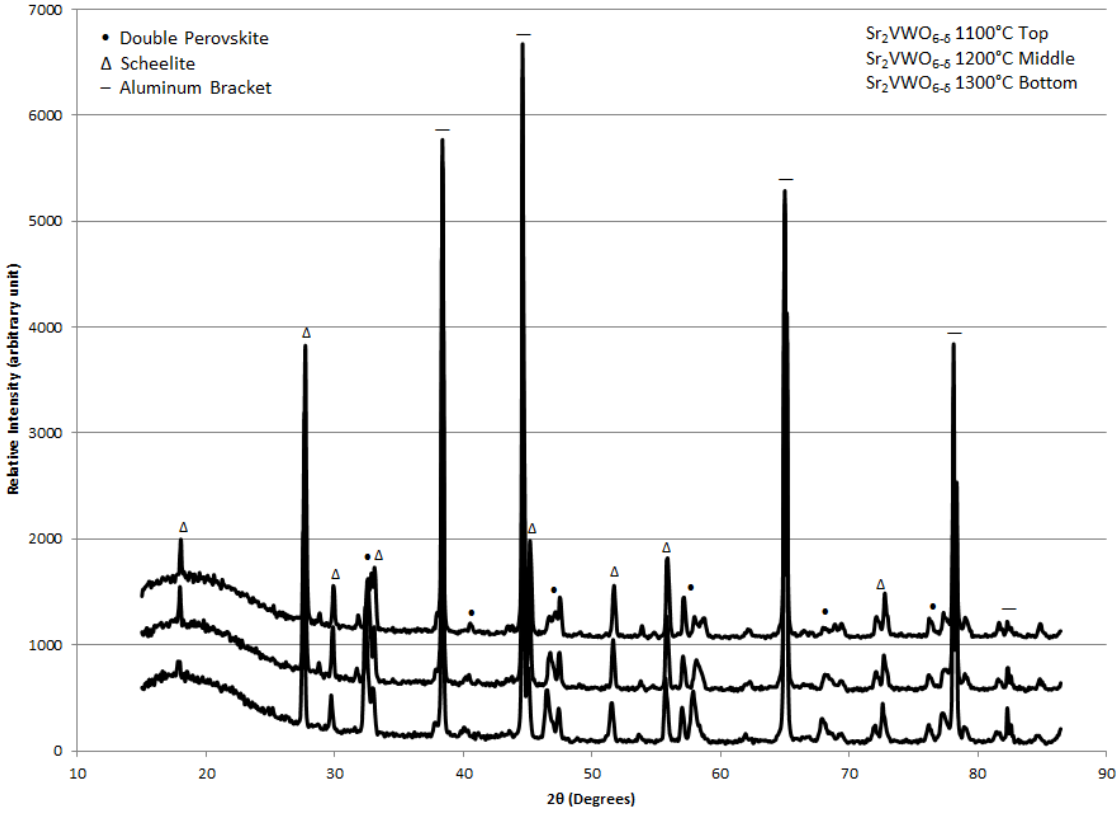


Figure 29: XRD pattern for Sr2VWO6-δ

Dilatometer tests were performed on all of the $Sr_{2-x}VMoO_{6-\delta}$ pellets sintered from 1100°C to 1300°C to determine the double perovskite sintering characteristics, as shown in Figures 30, 31, and 32. As seen in the dilatometer tests, all of the investigated double perovskites exhibit a major difference in the change in length due to sintering temperature and show larger decreases in length at increasing sintering temperatures. The $Sr_2VMoO_{6-\delta}$ pellets exhibit a quick change in length at sintering temperatures of 1200°C and 1100°C, but shows continuing densification over 20hr at 1300°C. The dilatometer tests also indicate that $Sr_{1.9}VMoO_{6-\delta}$ and $Sr_{1.8}VMoO_{6-\delta}$ do not reach their maximum change in length after the 20hr sintering time for 1200°C and 1300°C, but do reach their maximum change in length quickly for 1100°C. $Sr_{1.9}VMoO_{6-\delta}$ also has the highest

change in length overall and at both 1300°C and 1200°C. The larger decrease in length at increasing sintering temperatures corresponds to the higher coarsening effect observed in the microstructure of the sintered pellets.

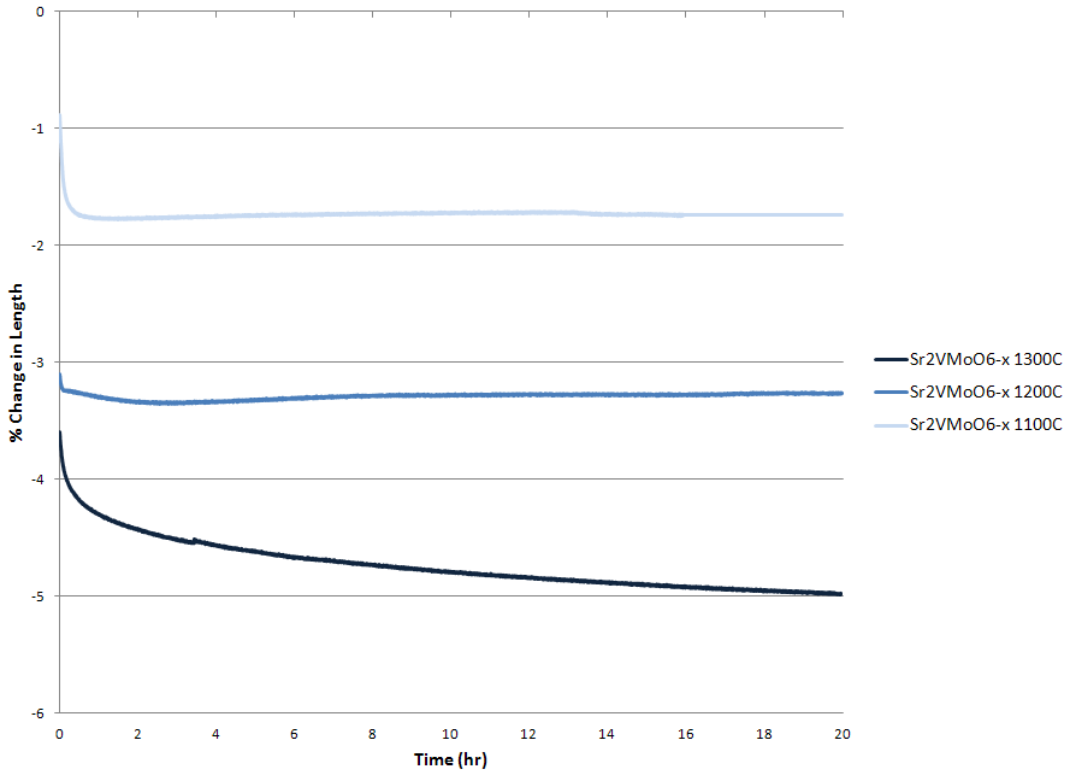


Figure 30: Percent change in length vs. time during sintering of $Sr_2VMoO_{6-\delta}$ pellets

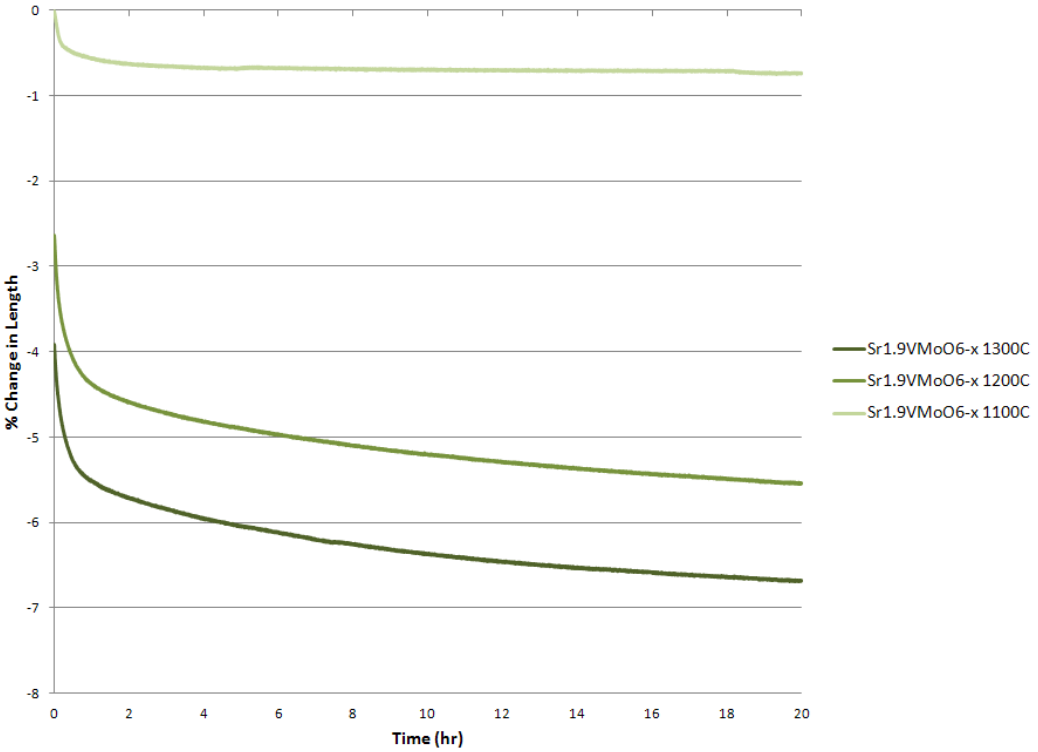


Figure 31: Percent change in length vs. time during sintering of $Sr_2VMoO_{6-\delta}$ pellets

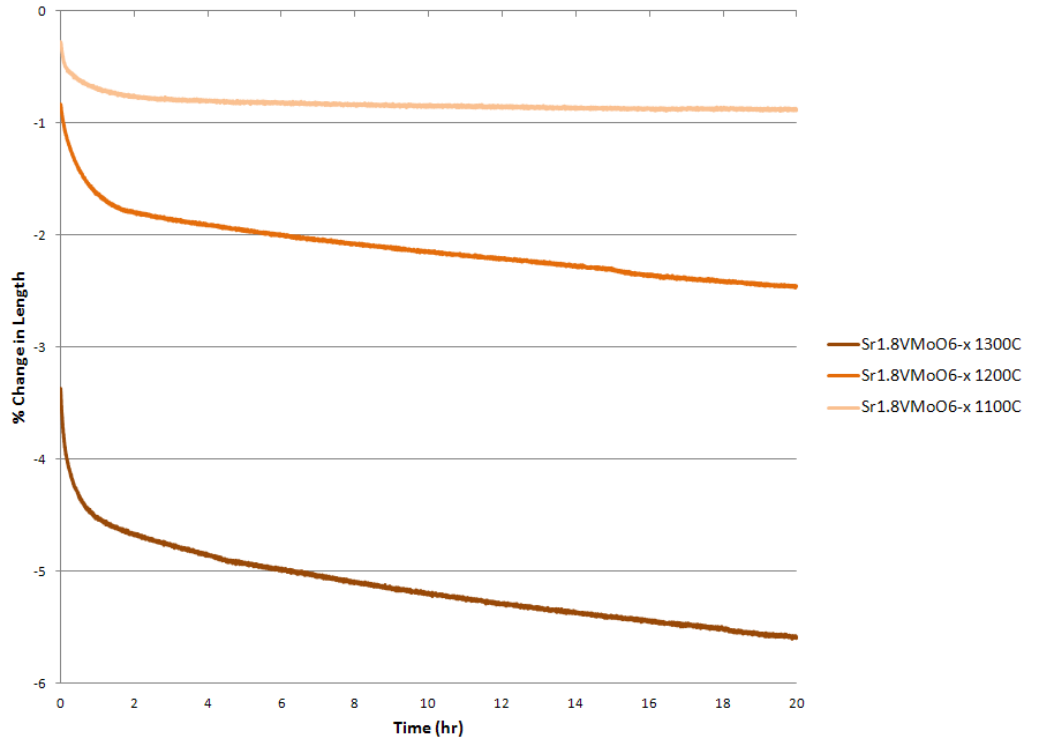


Figure 32: Percent change in length vs. time during sintering of $Sr_2VMoO_{6-\delta}$ pellets

The coarsening effect observed in the A-site deficient $Sr_{2-x}VMoO_{6-\delta}$ pellets, coincides with the coarsening effects found by Weber et al. (17) for A-site deficient lanthanum strontium magnesium oxide (LSM). As shown in Figure 33, the microstructure of the stoichiometric $Sr_2VMoO_{6-\delta}$ double perovskite matches the microstructure of the stoichiometric $La_{0.8}Sr_{0.2}MnO_{3-\delta}$ air electrode perovskite. Also, both A-site deficient materials exhibit high amounts of coarsening. This phenomenon has been attributed to an increase in a Mn_2O_3 secondary phase in the LSM air electrode (17).

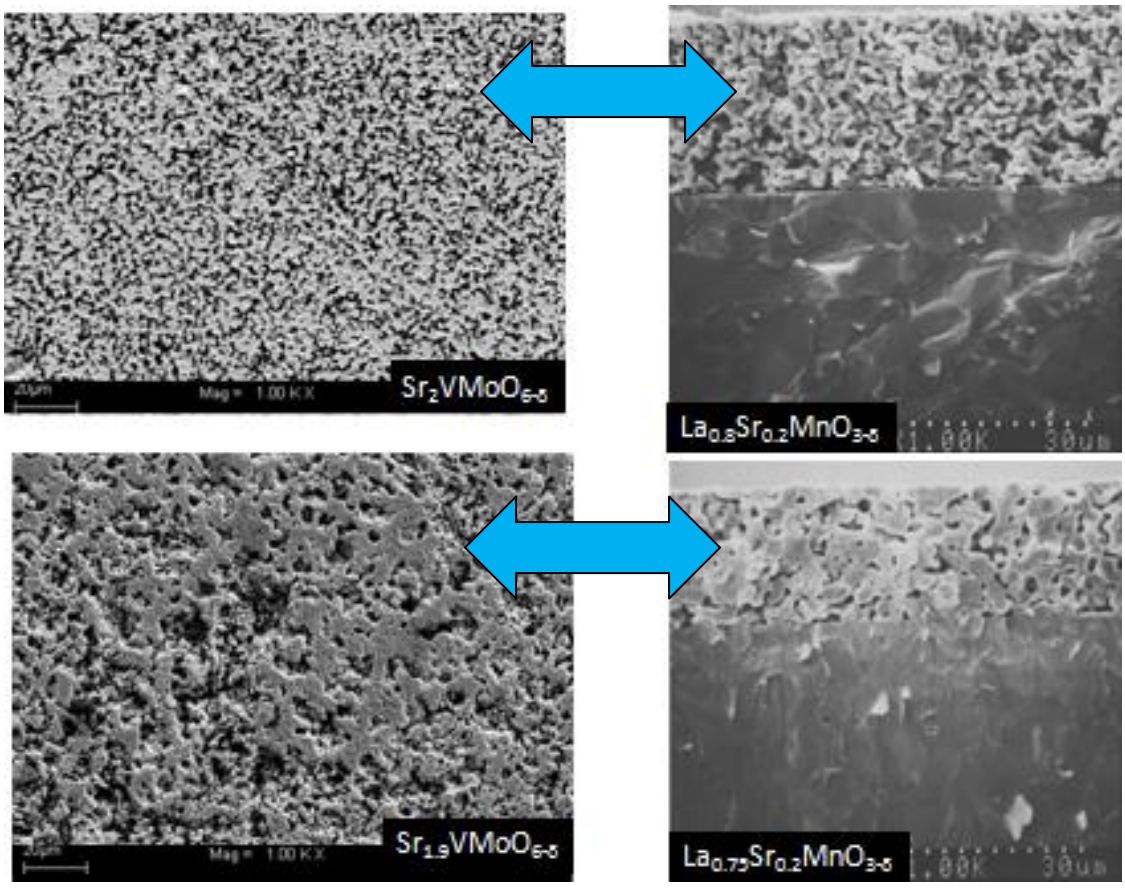


Figure 33: Comparison of A-site deficient perovskite microstructures

$Sr_2VMoO_{6-\delta}$, $Sr_{1.9}VMoO_{6-\delta}$, and $Sr_{1.8}VMoO_{6-\delta}$ redox tested pellets exhibited much different behavior during the cycling of forming gas (95%N_2/5%H_2), Nitrogen, and Air at 800˚C for one hour intervals, as shown in Figure 34. $Sr_2VMoO_{6-\delta}$ showed an initial increase in length when exposed to air and then slowly decreases in length during the redox cycling, which is in contrast to an increase in length of the $Sr_{1.8}VMoO_{6-\delta}$ pellet. The $Sr_{1.9}VMoO_{6-\delta}$ pellet rapidly increases and then decreases with initial exposure to air and then shows little to no change in length throughout the rest of the redox cycles. The overall decrease in length of the $Sr_2VMoO_{6-\delta}$ pellet and the steady nature of the $Sr_{1.9}VMoO_{6-\delta}$ pellet suggests that these two double perovskites would adapt better to change in oxygen partial pressure that could be encountered during SOFC operation.

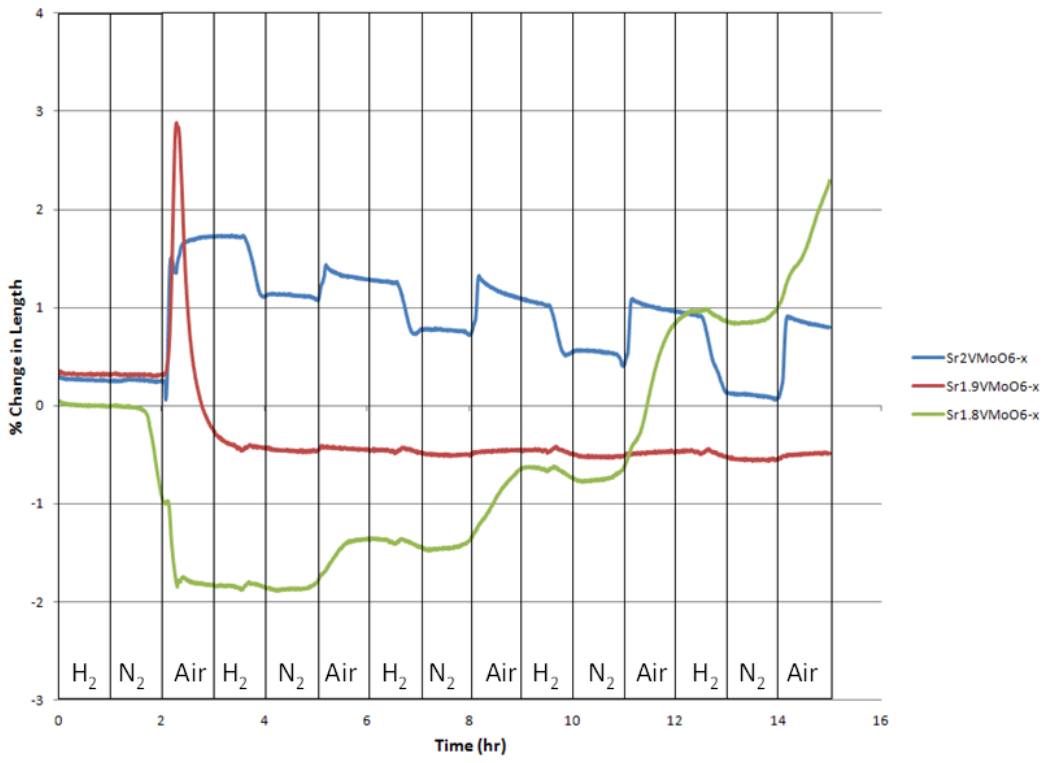


Figure 34: % Change in Length vs. Time for $Sr_{2-x}VMoO_{6-\delta}$

The microstructure of the $Sr_2VMoO_{6-\delta}$ redox cycled pellet indicates that two distinct layers form during the cycling of gasses at high temperatures, as shown in Figure 35. The microstructure of the tan colored middle section of the pellet resembles the original microstructure and the microstructure of the black outside section of the pellet shows some coarsening. However, elemental mapping of the $Sr_2VMoO_{6-\delta}$ redox cycled pellet, as shown in Figure 36, does not indicate major cation migration. The microstructure of the $Sr_{1.8}VMoO_{6-\delta}$ pellet indicates that three distinct layers form during redox testing, as shown in Figure 37. The microstructure of the black colored middle section of the pellet resembles the original microstructure. The microstructure of the grey and tan sections of the pellet show major coarsening effects from the redox testing. The elemental mapping of the $Sr_{1.8}VMoO_{6-\delta}$ pellet, as shown in Figure 38, indicates that the grey or second layer of the pellet is vanadium rich, while the black colored middle section is slightly molybdenum deficient. The vanadium rich regions between the coarsened outer layer and the porous inner layer seen in the $Sr_{1.9}VMoO_{6-\delta}$ and $Sr_{1.8}VMoO_{6-\delta}$ pellets suggest that vanadium is diffusing throughout the pellet, but is limited by the advanced coarsening on the outside of the pellet. This testing suggests that the fully stoichiometric double perovskite is more stable under redox cycling than the A-site deficient double perovskites.

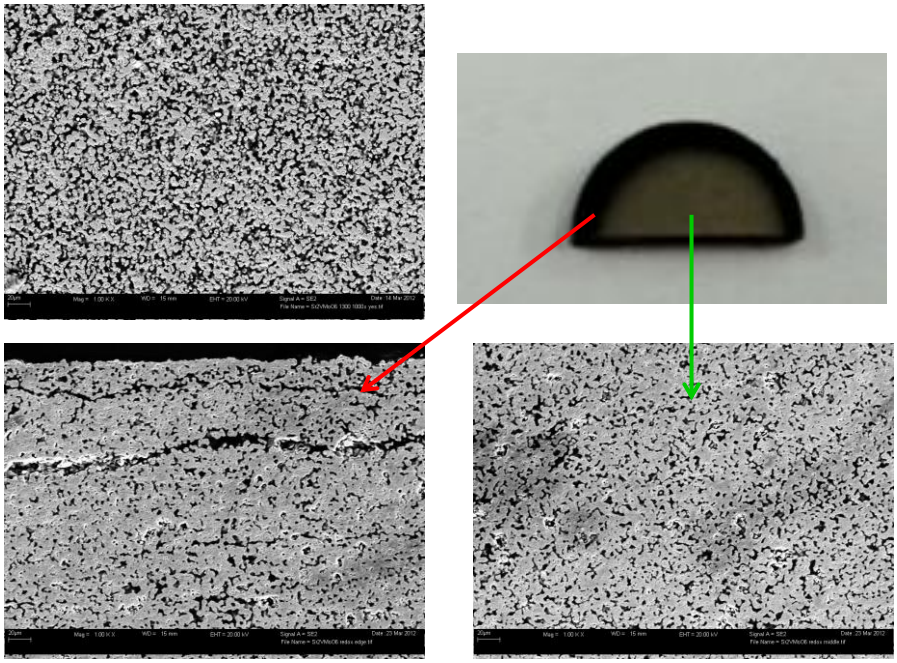


Figure 35: FESEM microstructure images of an original sintered $Sr_2VMoO_{6-\delta}$ pellet (upper left) and a redox tested $Sr_2VMoO_{6-\delta}$ pellet (bottom two images)

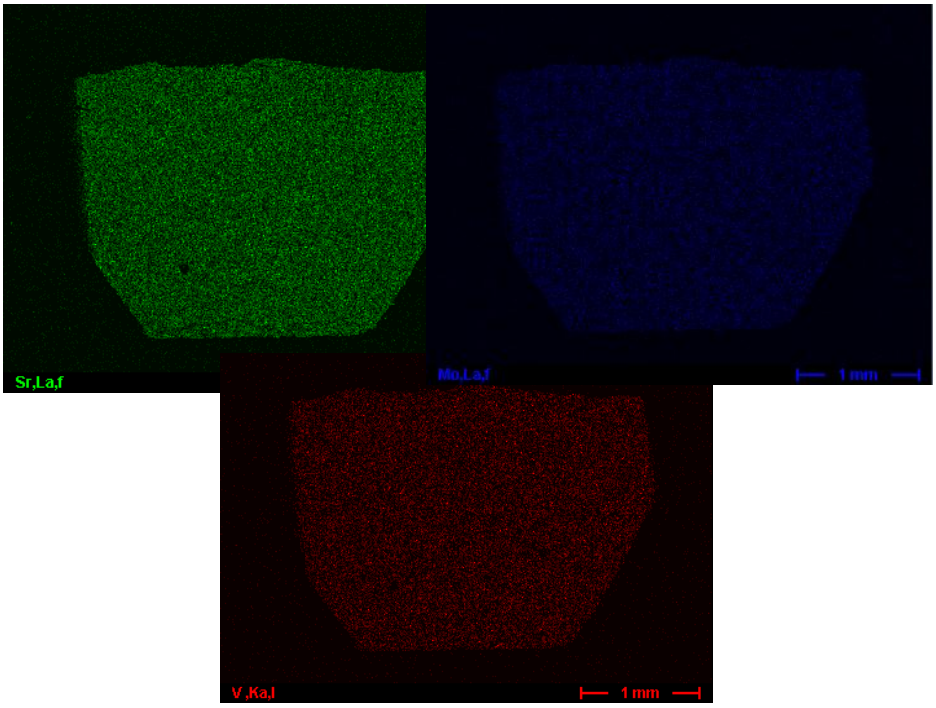


Figure 36: SEM elemental imaging of a $Sr_2VMoO_{6-\delta}$ redox tested pellet, where green, blue, and red represents Sr, Mo, and V, respectively

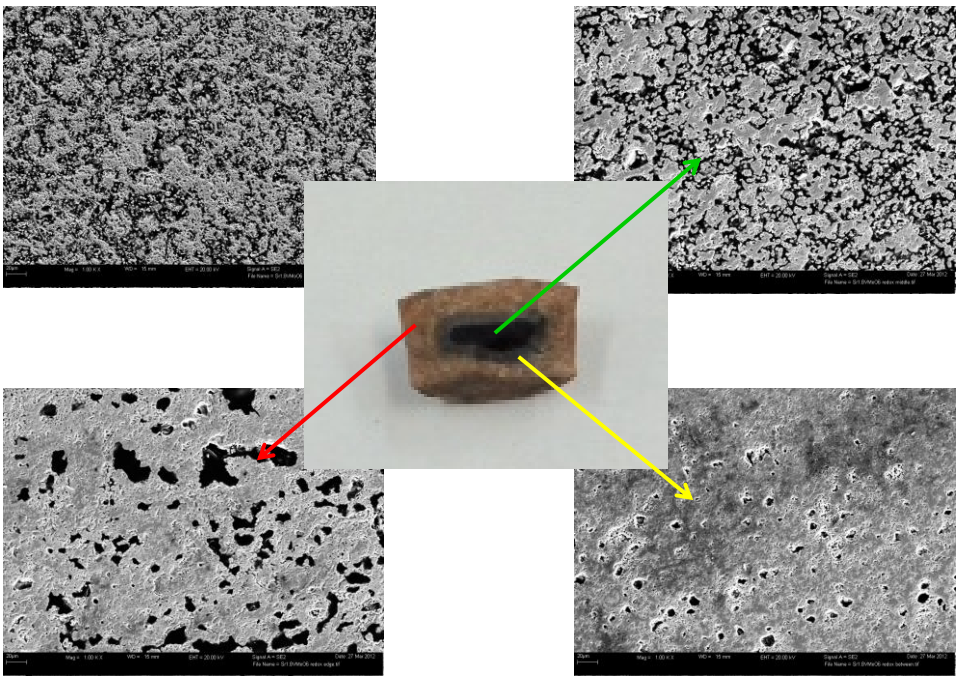


Figure 37: FESEM microstructure images of an original sintered $Sr_{1.8}VMoO_{6-\delta}$ pellet (upper left) and a redox tested $Sr_{1.8}VMoO_{6-\delta}$ pellet (bottom two and upper right images)

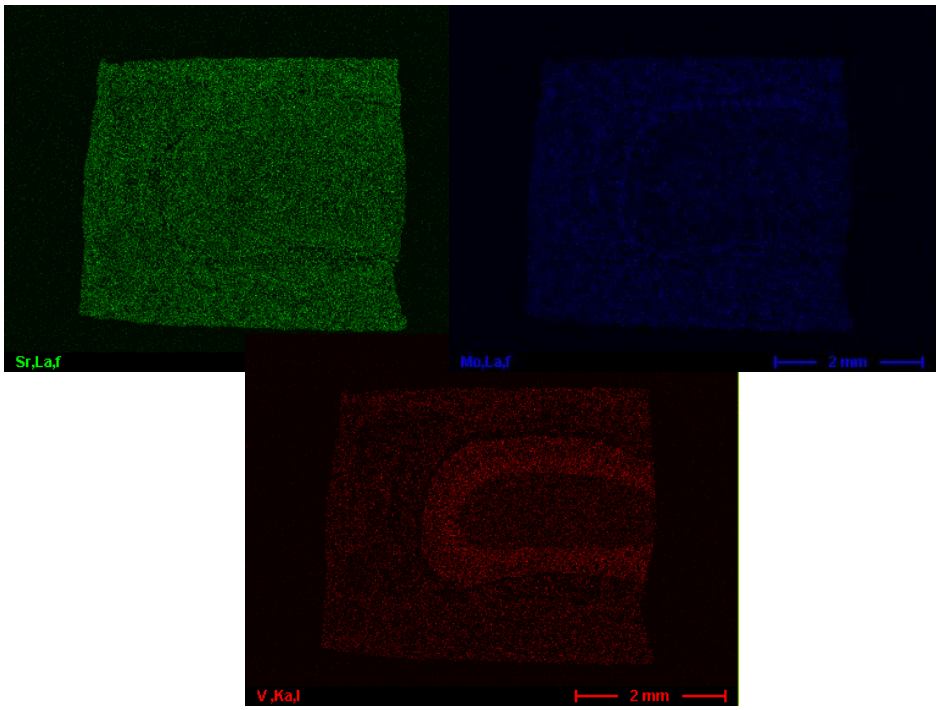


Figure 38: SEM elemental imaging of a $Sr_{1.8}VMoO_{6-\delta}$ redox tested pellet, where green, blue, and red represents Sr, Mo, and V, respectively

CHAPTER THREE

ELECTRICAL CONDUCTIVITY OF $Sr_{2-x}VMoO_6$ (x=0.0, 0.1, 0.2) DOUBLE PEROVSKITE SOLID OXIDE FUEL CELL FUEL ELECTRODE

Contribution of Authors and Co-Authors

Manuscripts in Chapters 2, 3, and 4

Author: Nick Childs

Contributions: Analyzed XPS and XRD. Provided the initial manuscript.

Co-Author: Adam Weisenstein

Contributions: Performed TGA, XPS, and conductivity testing. Also, assisted with the manuscript revisions.

Co-Author: Clay Hunt

Contributions: Performed XRD testing and assisted with manuscript revisions.

Co-Author: Richard Smith

Contributions: Collaborated on the conception and design of the investigation and provided important intellectual content to the manuscript.

Co-Author: Stephen Sofie

Contributions: Collaborated on the conception and design of the investigation and provided important intellectual content to the manuscript.

Manuscript Information Page

Nick Childs, Adam Weisenstein, Clay Hunt, Stephen Sofie, Richard Smith
Journal of Solid State Ionics
Status of Manuscript:
__X_ Prepared for submission to a peer-reviewed journal
____ Officially submitted to a peer-review journal
____ Accepted by a peer-reviewed journal
____ Published in a peer-reviewed journal

Elsevier
Prepared to be Submitted December, 2012

CHAPTER THREE

ELECTRICAL CONDUCTIVITY OF $Sr_{2-x}VMoO_6$ (x=0.0, 0.1, 0.2) DOUBLE PEROVSKITE SOLID OXIDE FUEL CELL FUEL ELECTRODE

Abstract

Electrical conductivity of $Sr_{2-x}VMoO_{6-y}$ (x=0.0, 0.1, 0.2) solid oxide fuel cell fuel elctrode material has been investigated in a reducing atmosphere at temperatures up to 800 ^{0}C. A solid state synthesis technique was used to fabricate materials and crystal structure was verified through X-ray diffraction. Elemental valence states were identified through X-ray photoemission on the double perovskite material before and after annealing in a hydrogen environment. Samples exhibited metallic conduction with electrical conductivities of 1250 S/cm ($Sr_2VMoO_{6-y'}$), 2530 S/cm ($Sr_{1.8}VMoO_{6-y''}$) and 3610 S/cm ($Sr_{1.9}VMoO_{6-y'''}$) at 800 ^{0}C in 5%H_2/95%N_2. A highly insulating phase begins to reduce between 400 and 500 ^{0}C in a 5%H_2/95%N_2 environment, as confirmed by X-ray photoemission and thermal gravimetric analysis. This reduction leads to a large increase in electrical conductivity.

Keywords: SOFC, Fuel Electrode, Conductivity, Perovskite, MEIC, Sr_2VMoO_6, XPS, XRD, TGA

1. Introduction

Fuel cells are an attractive power source due to their ability to efficiently convert chemical energy stored in fuel directly into electricity. The ability of Solid Oxide Fuel Cells (SOFCs) to reform hydrocarbons at the fuel electrode provides for fuel flexibility, an advantage over other types of fuel cell technologies (45).

Current state-of-the-art SOFC technology utilizes a porous cermet fuel electrode consisting of nickel and yttria-stabalized zirconia (YSZ). Percolated networks of nickel, YSZ and pores allow for transport of electrons, oxygen ions and gases within the fuel electrode. The junction of these three phases (Ni, YSZ, pore) form a triple phase boundary (TPB). Fuel electrode reactions are localized to the TPB in this system, limiting the active area of the electrode. Additional well know problems exist with Ni-YSZ fuel electrode materials such as agglomeration of nickel particles (46; 47), irreversible degradation due to sulfur poisoning (48) and susceptibility to coke formation (49).

Perovskite type materials are of interest as a fuel electrode material in part due to its potential as a mixed electronic and ionic conductor (MEIC). Replacing Ni and YSZ with a MEIC establishes the active fuel electrode region over a dual phase boundary (DPB) at the surface of the MEIC instead of localizing it to a TPB. Additionally the perovskite type materials have shown stability in high temperature reducing environments, catalytic ability to oxidize hydrogen and methane, tolerance to sulfur poison in and resistance to coke formation (11; 25; 26).

Electrical conductivity has been reported for a variety of Sr_2MMoO_6 (M= V, Fe, Mn, Mg, Cr, Co, Ni) double perovskite materials. A summary of the reported electrical

conductivities of these and other relevant materials is presented in Table 5 (50; 51; 52; 53; 54; 55; 56; 25; 7; 18) (57; 58; 59). Sr_2VMoO_6 has the highest reported electrical conductivity of these materials, with a value of 280 S/cm at 900 C in a reducing atmosphere. Band structure calculations for this material predict metallic like conduction (60). Polycrystalline $SrVO_3$ and $SrMoO_3$ samples have reported room temperature electrical conductivities of 400 S/cm (59) and 10,000 S/cm (58) respectively, with single crystal $SrMoO_3$ conductivity reported at 200,000 S/cm (57). These factors make the Sr_2VMoO_6 double perovskite material interesting as a highly electrically conductive oxide material.

Table 5: Reported electrical conductivities of Sr2B'MoO_6

Composition	Conductivity $\frac{S}{cm}$	Temperature ^0C	Environment	Reference
Sr_2VMoO_6	12000	25	Air	Karen 2006
Sr_2VMoO_6	280	900	10 %H_2/N_2	Aguadero 2011
Sr_2VMoO_6	256*	800	vacuum after reduction	Fortiev 1987
Sr_2FeMoO_6	222*	800	H_2	Zhang 2010
Sr_2MnMoO_6	~10	800	H_2	Huang 2006
Sr_2MgMoO_6	~10	800	H_2	Huang 2006
Sr_2MgMoO_6	7.7*	800	5%H_2/Ar	Vasala 2010
Sr_2CrMoO_6	2.54*	800	5%H_2/Ar	Yin 2011
Sr_2CoMoO_6	1.7*	800	5%H_2/Ar	Huang 2009
Sr_2CoMoO_6	4.0*	800	H_2	Huang 2009
Sr_2CoMoO_6	0.013	800	5%H_2 / N_2	Viola 2002
Sr_2CoMoO_6	0.08	800	15%H_2	Viola 2001
Sr_2NiMoO_6	0.07*	800	5%H_2/Ar	Huang 2009
Sr_2NiMoO_6	.45*	800	H_2	Huang 2009
Ni – YSZ(15vol%Ni)	.103	900	H_2	Aruna 1998
Ni – YSZ(30vol%Ni)	40	900	H_2	Aruna 1998
Ni – YSZ(50vol%Ni)	989	900	H_2	Aruna 1998
$SrVO_3$	100*	577	H_2/Ar mixture	Giannakopoulou 1994
$SrMoO_3$	10000*	27	cryostat	Hayashi 1979
$SrMoO_3$ (single crystal)	196000	27	Not reported	Nagai 2005

*Read from published graph

2. Experimental

2.1 Synthesis

$Sr_{2-x}VMoO_{6-\delta}$ powder was fabricated by solid state synthesis, utilizing Alfa Aesar $SrCO_3$ stock# 33392, VO_2 stock# 22957, and MoO_2 stock# precursor powders. This powder was then calcined at 1000°C for 6 hours. The calcined powder was uniaxially pressed into 1/4in (6.35mm) at 250MPa to form pellets. A slurry was also made from solvents, dispersants, plasticizers, and binders with the $Sr_{2-x}VMoO_{6-\delta}$ calcined powders, at a solids loading of 30%. The slurry was extruded through a doctor blade onto a Mylar film. The slurry was dried and disks were punched out of the green tapes in preparation for sintering and testing. The double perovskite structure was formed by thermally treating the green tape disks and pellets in a reducing wet ($5\%H_2$ $95\%N_2$) atmosphere ($10^{-11}pO_2$) at 1300°C for 20 hours in a tube furnace. The density of the uniaxially pressed pellets exhibited a much higher density (3.0g/cc), than the tape cast disks (2.63g/cc). The changes in A-site amounts also contributed to variations in the microstructure and porosity, as shown in Figure 39. Porosity was also calculated from analysis of the images in Figure 39.

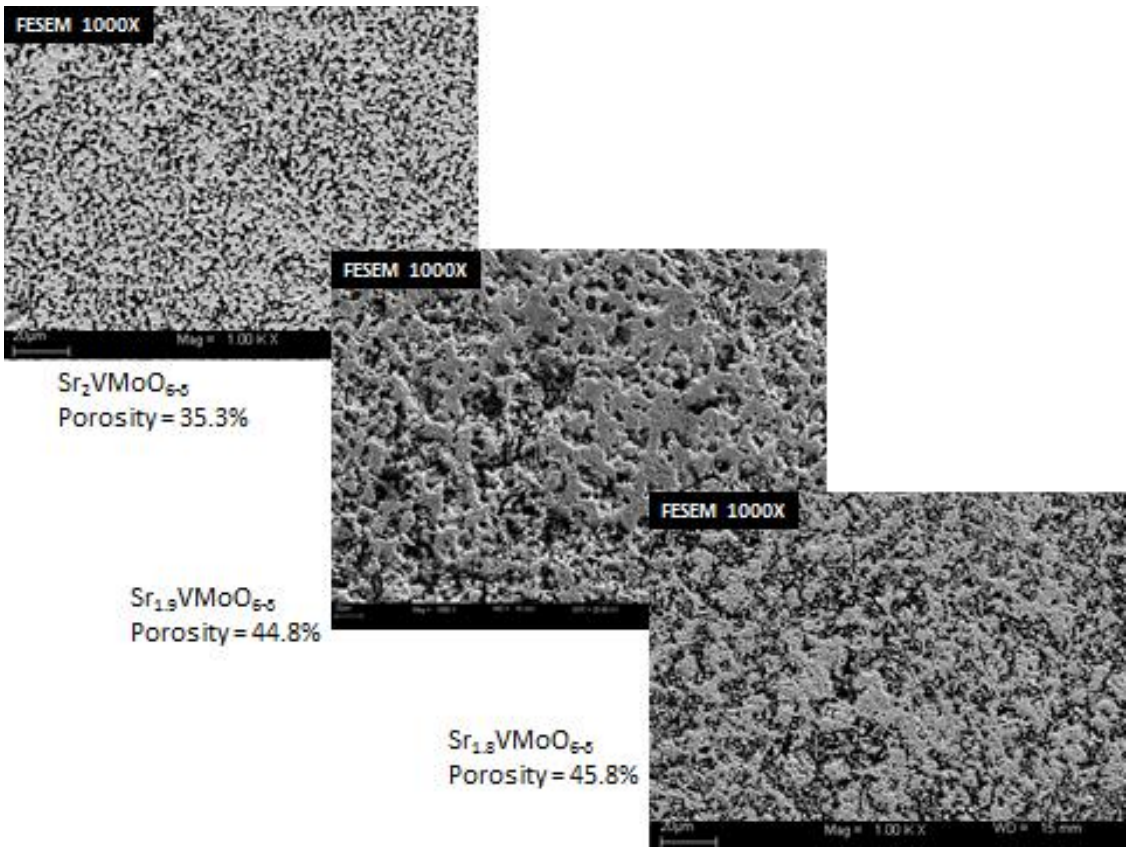


Figure 39: Microstructure and porosity of $Sr_{2-x}VMoO_{6-\delta}$ double perovskites sintered at 1300°C

2.2 X-Ray Diffraction

X-ray powder diffraction (XRD) was used to verify the double perovskite crystal structure in Sr_2VMoO_{6-y}, pellets. Powder for XRD was ground from pellets after the sintering process and from pellets placed in the furnace during conductivity measurements. A Cu Kα source was used over an angular range of $25\text{-}60^0$ 2θ with a step size of 0.01^0. Measurements were taken at room temperature in air.

2.3 Electrical Conductivity

DC conductivity tests were performed on the 1300°C sintered $Sr_{2-x}VMoO_{6-\delta}$ double perovskite pressed pellets using a modified 4-probe measurement technique, utilizing an Agilent 34420A Nano Volt Meter. The conductivity tests were set up by attaching two silver wire leads to the top and two to the bottom of the double perovskite disks. Silver electrodes were painted on the top and the bottom of the disks to create a uniform conducting layer across the face of the double perovskite pellets. The silver wire/electrode assembly was then clamped between electrical insulating alumina plates by a stainless steel fixture. The conductivity tests were conducted inside a tube furnace (Lindberg/Blue TF55035A-1) for which a controlled wet reducing atmosphere of (2.9% H_2O, 4.9%H_2 and 92.2%N_2) could be introduced. The conductivity testing apparatus is shown in Figure 40. Temperature segmented tests from room temperature to 200˚C, 400˚C, 600˚C, and 850˚C at a heating rate of 2˚C/min were performed on the 1300°C sintered $Sr_{2-x}VMoO_{6-\delta}$ double perovskite pressed pellets to further demonstrate the effects of temperature and reduction on conductivity. These tests were continuous with samples being cycled in a wet reducing environment from room temperature -> 200 ˚C -> RT -> 400 ˚C -> 50 ˚C ->600 ˚C -> 50 ˚C -> 850 ˚C -> 50 ˚C. Conductivity measurements were made every minute during this cycle. The error in calculated conductivity is dominated by the sample geometry measurement at low conductivities (+/-0.5 S/cm at 10 S/cm) and by the resistance measurement at high conductivities (+/- 60 S/cm at 10,000 S/cm).

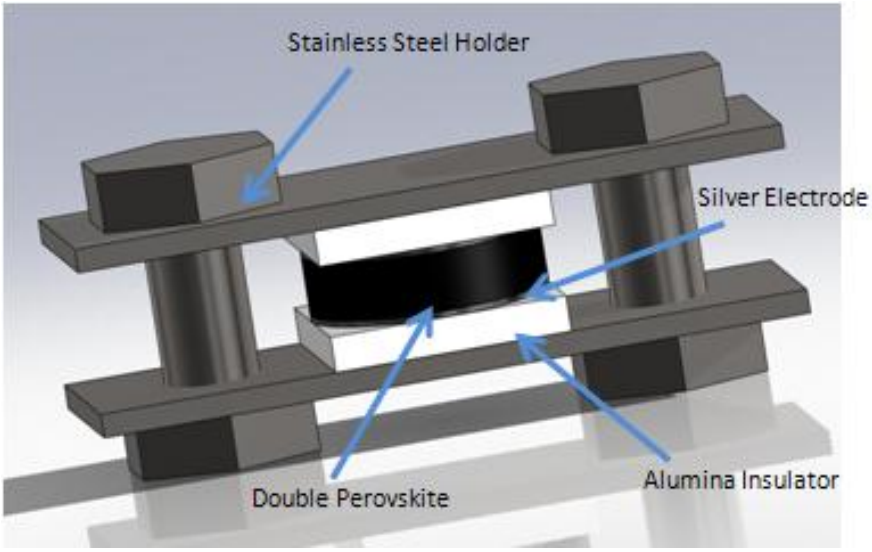


Figure 40: Conductivity testing apparatus

2.4 Thermal Gravitational Analysis

Thermal Gravimetric Analysis (TGA) was utilized to determine the total weight loss due to reduction of the $Sr_{2-x}VMoO_{6-\delta}$ samples, in a dry reducing atmosphere (5%H_2 and 95%N_2), from room temperature to 800˚C then cooled back to room temperature. This was done with a heating and cooling rate of 2˚C/min.

2.5 X-Ray Photoelectron Spectroscopy

X-ray photoelectron spectroscopy (XPS) was used to determine elemental valence states before and after electrical conductivity measurements. XPS was also conducted before and after 30 minute anneals in 10^{-6} torr H_2 at temperatures ranging from 200-700 ^{0}C. The tape casting technique produced much thinner samples than the pressed pellets (0.8 mm vs 3.0 mm). The heating characteristics for the thinner more porous samples allowed for the investigation of the effects of annealing at higher temperatures and thus were used. These annealings were performed in a ultra-high vacuum chamber by raising

the base chamber pressure of less than 10^{-9} torr to a pressure of 10^{-6} torr by introducing research grade H_2. The sample was then heated to the desired temperature and held for 30 minutes. The sample temperature was brought to room temperature in less than 10 minutes by flowing liquid nitrogen through the sample holder. Once the sample temperature was below room temperature, the H_2 flow was stopped and a chamber pressure of less than 10^{-9} torr was obtained before XPS was conducted. A magnesium X-ray source (Mg Kα = 1253.6 eV, 0.7 eV FWHM) operated at 15 kV and 15 mA was used to stimulate electron emission from depths up to 1.0 nm. The C 1s, O 1s, V 2p, Sr 2p and Mo 3d regions were recorded. The spectrometer energies were calibrated to the O 1s (530.0 eV) peak for the V 2p region and the C 1s (284.6 eV) peak was used for the Sr 2p and Mo 3d regions. Binding energies obtained were precise within +/- 0.3 eV. A Shirley background was used during peak fitting and a Marquardt-Levenberg (31) optimization algorithm was implemented by the CasaXPS software program to deconvolute emission peaks into different valence contributions.

3. Results

3.1 X-Ray Diffraction

The majority phase for powders ground from $Sr_{2.0}VMoO_{6-\delta}$ pressed pellets and tape cast discs was found to be in agreement with reflections based on the crystal information provided by Karen et. al. for the double perovskite $Sr_2VMoO_{6.0}$. (18). The main contaminate phase was found to be $Sr_3V_2O_8$ (space group R-3m a=b=5.620 A c=7.445 A) (61) with a small signal from $SrMoO_4$ (space group $I4_1/a$ a=b=5.394 and c =12.010 A) (62). No significant changes were noted in the crystal structure or the

amounts of contaminate phases when comparing powders ground before and after thermal cycling in a wet reducing atmosphere. An XRD pattern from powders ground from pellets after the sintering process is shown in Figure 41.

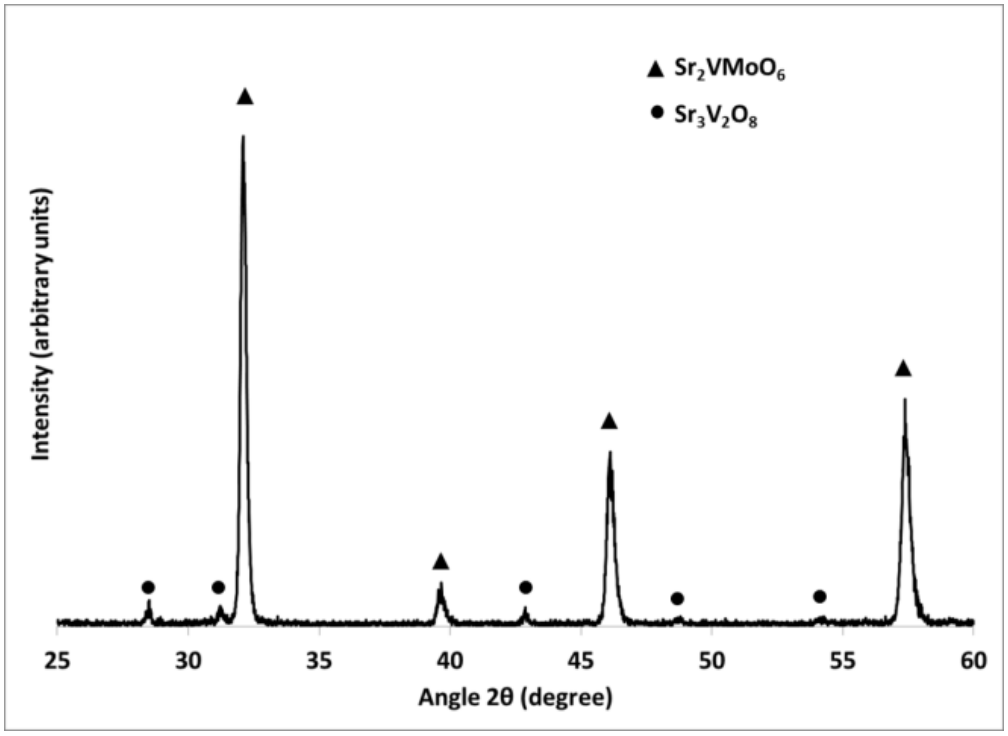


Figure 41: XRD pattern of a Sr_2VMoO_6 pressed pellet at room temperature in air. A contaminate phase of $Sr_3V_2O_8$ is noted with circles, a small signal can also be found for the $SrMoO_4$ phase

3.2 Electrical Conductivity

The initial room temperature conductivity measurements for SR20, SR19 and SR18 pellets were 3.2 S/cm, 4.6 S/cm and 9.4 S/cm respectively, as shown in Figure 42. Conductivities measured during and after cycling from RT-> 200 ˚C -> 50 ˚C showed no significant changes. The measured conductivity for the three tested stoichiometries on the cycle from 50 ˚C -> 400 ˚C -> 50 ˚C is shown in Figure 43. Semi-conductor like

conduction is shown throughout the cycle, however a significant change was observed in the behavior. Upon heating the average conductivity of the three samples increased from 11 S/cm to 435 S/cm. After cooling from 400 ˚C to 50 ˚C the measured conductivities were 159 S/cm, 219 S/cm and 265 S/cm for the SR20, SR19 and SR18 pellets.

Heating to 600 ˚C from 50 ˚C resulted in an increase of conductivity to an average of 1423 S/cm for the three samples, after cooling conductivities returned to the approximate values found after the 400 ˚C cycle, as shown in Figure 44. The final heating from 50 ˚C-> 850 ˚C resulted in conductivities of SR20 = 1250 S/cm, SR18 = 1800 S/cm and SR19 = 3000 S/cm at 800 ˚C in a wet reducing atmosphere (Figure 45). When cooled from 850 ˚C all samples exhibited metallic conduction. Final 50 ˚C conductivities for the SR20 and SR18 samples were 9300 S/cm and 18000 S/cm respectively. The SR19 conductivity was superior to other stoichiometries and reached the limits of the meter as can be seen by the scatter as the sample approaches 50 ˚C. A linear extrapolation on the calculated slope during cooling from 850 ˚C to 600 ˚C results in a 50 ˚C conductivity of ~30,000 S/cm for the SR19 sample.

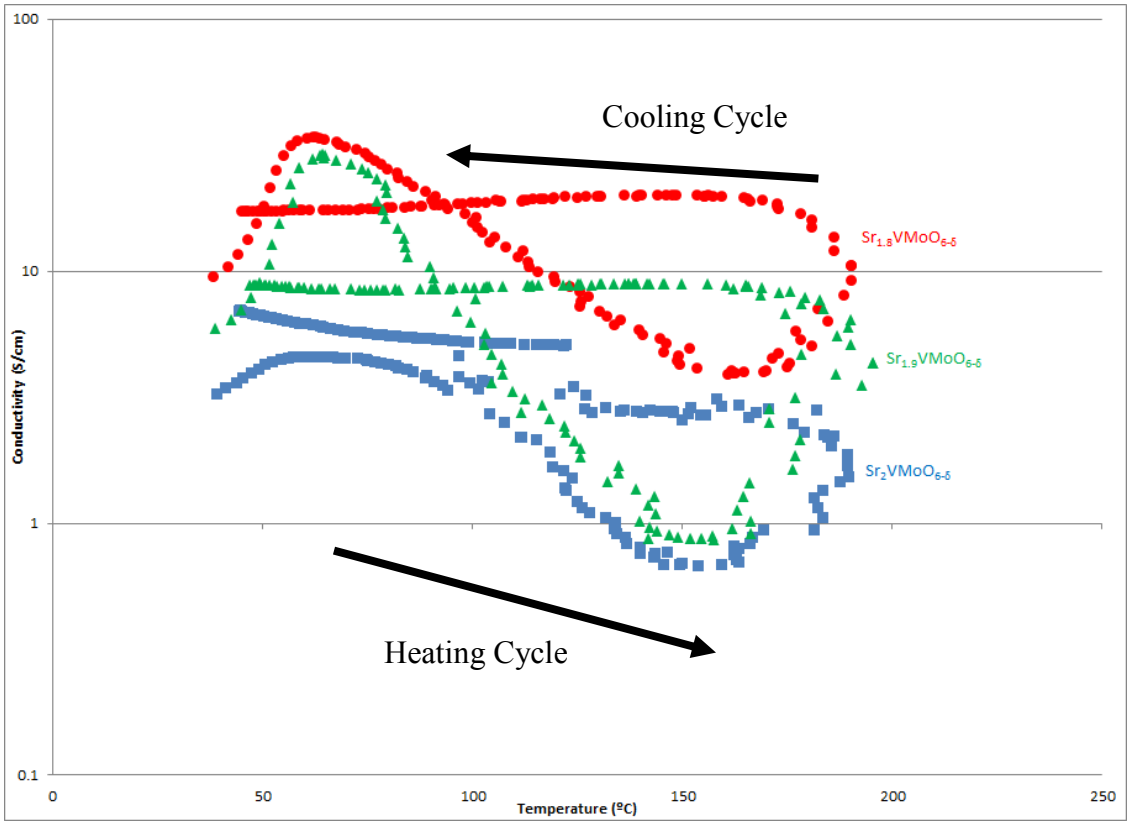


Figure 42: Electrical conductivity of $Sr_{2-x}VMoO_{6-y}$ pressed pellets vs. temperature upon heating to and cooling from 200 ^{0}C in a nitrogen environment with 2.9% H_2O/4.9% H_2 content

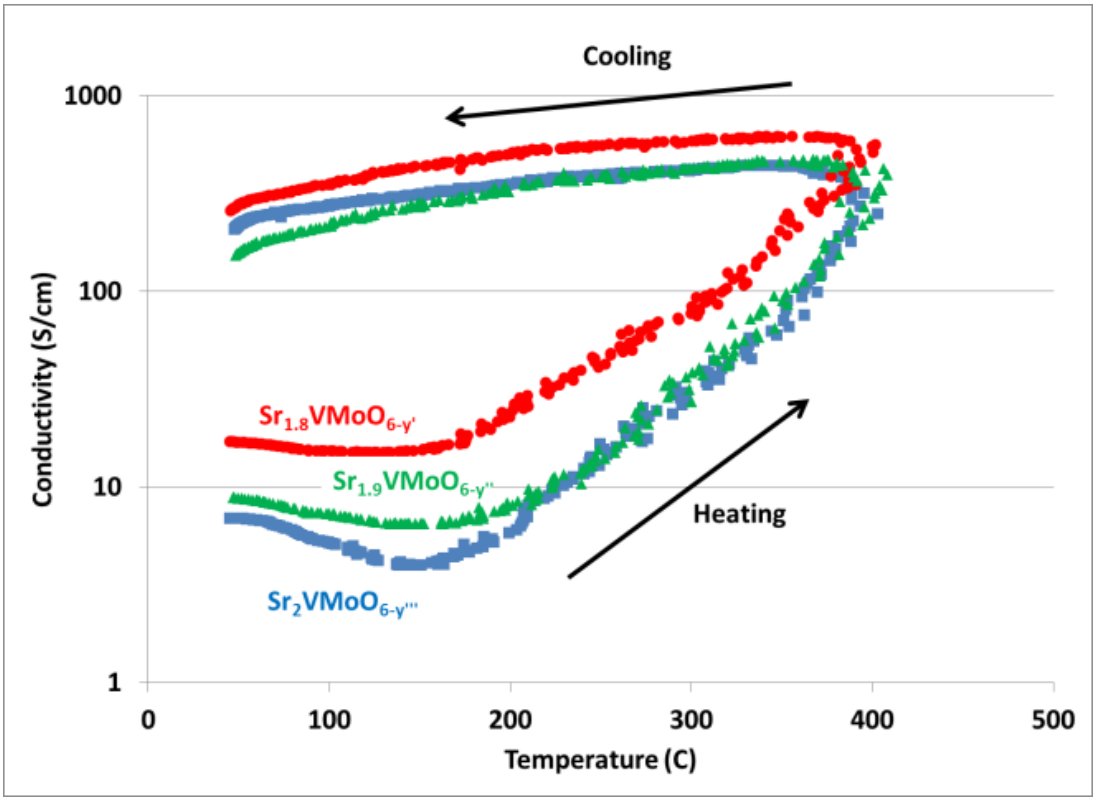


Figure 43: Electrical conductivity of $Sr_{2-x}VMoO_{6-y}$ pressed pellets vs. temperature upon heating to and cooling from 400 ^{0}C in a nitrogen environment with 2.9% H_2O/4.9% H_2 content

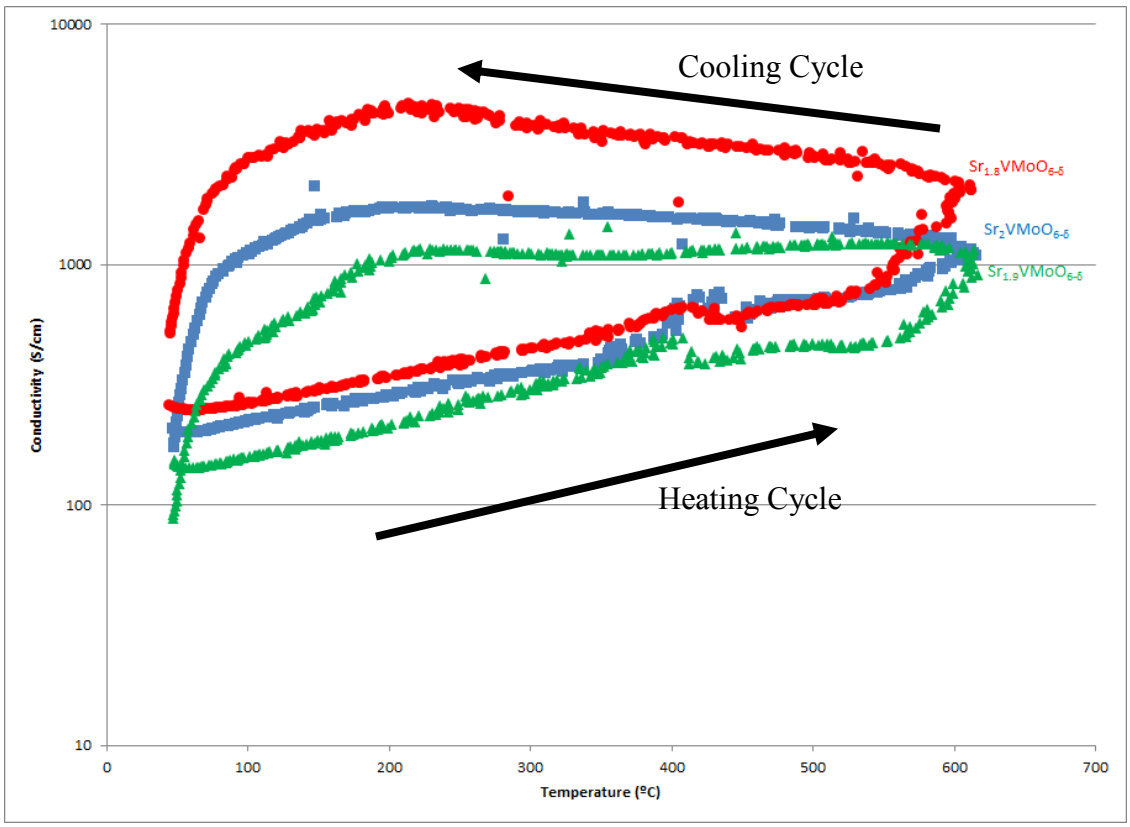


Figure 44: Electrical conductivity of $Sr_{2-x}VMoO_{6-y}$ pressed pellets vs. temperature upon heating to and cooling from 600 ^{0}C in a nitrogen environment with 2.9% H_2O/4.9% H_2 content

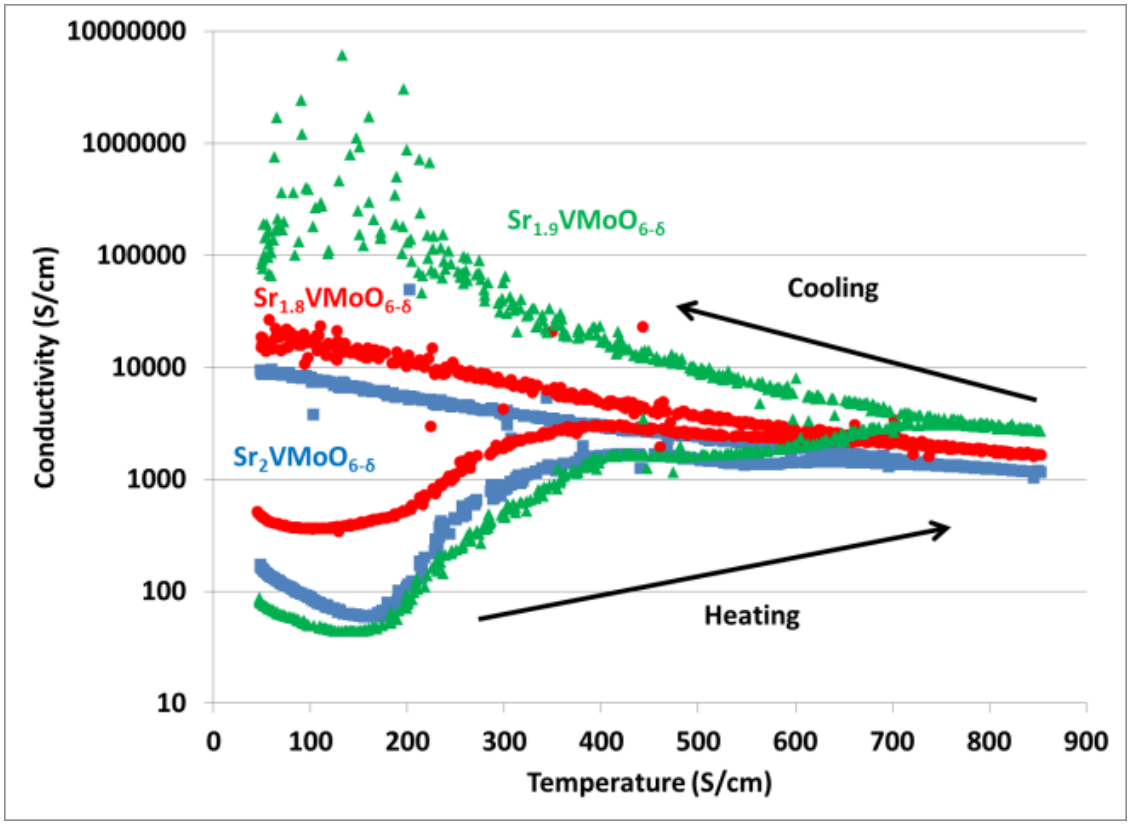


Figure 45: Electrical conductivity of $Sr_{2-x}VMoO_{6-y}$ pressed pellets vs. temperature upon heating to and cooling from 850 ^{0}C in a nitrogen environment with 2.9% H_2O/4.9% H_2 content. The scatter in data as the $Sr_{1.9}VMoO_{6-y}$, cools below 300 ^{0}C is due to instrument limitation in measuring such high conductivity

3.3 Thermal Gravitational Analysis

TGA was utilized to determine the total weight loss due to reduction of $Sr_{2-x}VMoO_{6-\delta}$ sintered powders on a cycle from room temperature to 850 ˚C and back to room temperature. The total weight loss for the three samples averaged over three separate runs was 0.223%, 0.124% and 0.087% for the SR20, SR18 and SR19 powders, as shown in Figure 46.

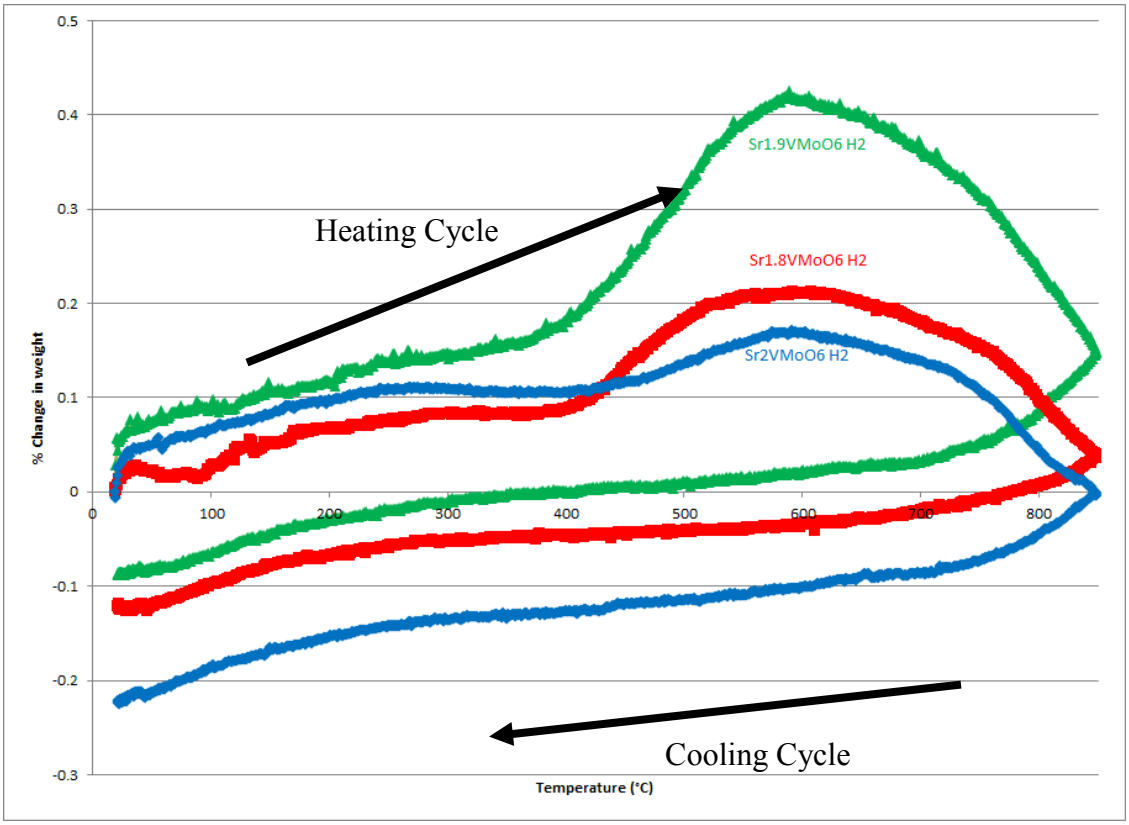


Figure 46: % change in weight of $Sr_{2-x}VMoO_{6-\delta}$ of sintered powder from 30°C up to 850°C and back down to 30°C at 2°C/min

3.4 X-ray Photoelectron Spectroscopy

XPS analysis was performed on SR20, SR19 and SR18 pressed pellets and tape cast discs. Comparison of XPS spectra from the two preparation techniques as prepared and after a 400 ˚C anneal yielded no significant differences. The tape cast discs are much thinner (0.8 mm vs 3.0 mm) than the pellets. The heating characteristics for the thinner more porous samples allowed for the investigation of the effects of annealing at higher temperatures and thus are reported.

As prepared samples exhibited a vanadium valence state dominated by V^{+5} (88.3% for SR20), with the remainder being in the V^{+4} state (11.7% for SR20). The

molybdenum valence state in the as prepared samples was dominated by the Mo^{+6} state (85.4% for SR20), with the remainder made up of Mo^{+5}/Mo^{+4} (3.7% Mo^{+5}/10.9% Mo^{+4} for SR20). The strontium and oxygen had expected valence states of +2 and -2 as expected and did not change state throughout the experiment.

A 30 minute anneal at 400˚C in 10^{-6} Torr H_2 (-log(pO_2/bar)= 47.5) resulted in a reduction of both the vanadium and molybdenum valence states. The vanadium valence distribution was 48.2% V^{+5}/27.3% V^{+4}/24.5% V^{+3}. The molybdenum valence distribution was 64.9% Mo^{+6}/9.5% Mo^{+5}/25.6% Mo^{+4}. An additional 30 minute anneal at 550 ˚C in 10^{-6} Torr H_2 (-log(pO_2/bar)= 40.6) resulted in a further reduction of both the vanadium and molybdenum valence states. The vanadium valence distribution was 32.6% V^{+5}/30.4% V^{+4}/37.0% V^{+3}. The molybdenum valence distribution was 66.1% Mo^{+6}/5.6% Mo^{+5}/28.3% Mo^{+4}. The deconvolution used to determine valence states for V $2p_{3/2}$ region and Mo 3 d region after the 550˚C annealing is presented in Figure 47. An additional 30 minute anneal at 700 ˚C in 10^{-6} Torr H_2 (-log(pO_2/bar)= 35.7) did not produce any further changes. The O 1s and the V 2p region progression through anneals up to 700˚C is presented in Figure 48 and the C 1s to Mo 3d region progression in Figure 49. A summary of all three stoichiometry valence distribution results and associated measured binding energies is summarized in table 6.

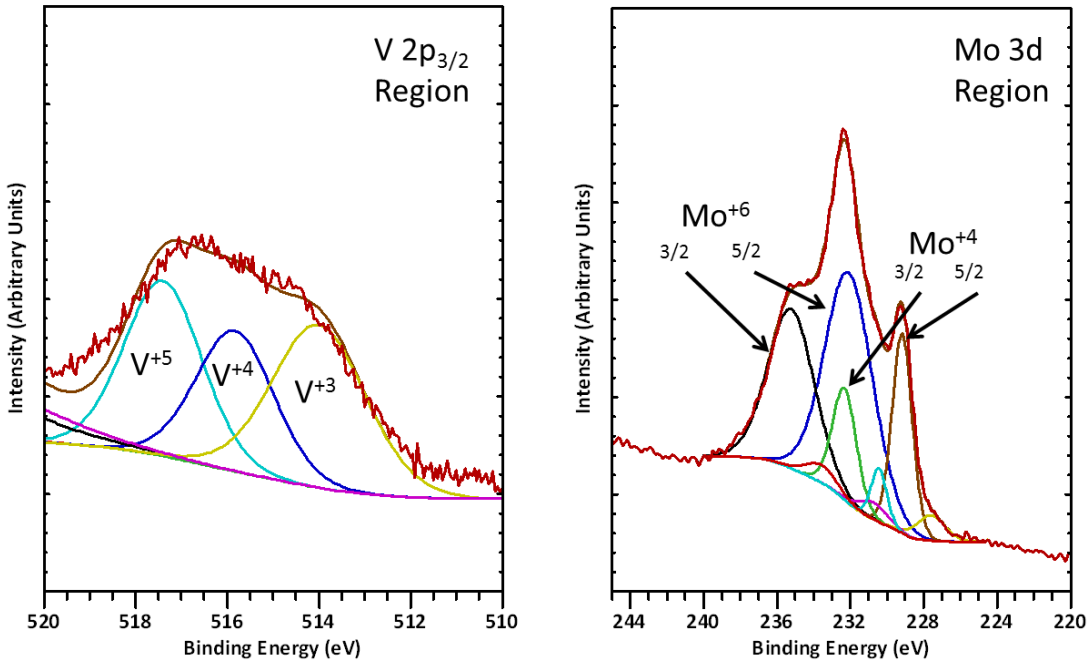


Figure 47: V $2p_{3/2}$ (left) and Mo 3d (right) core-level region XPS spectra of a Sr_2VMoO_6 tape cast pellet after 30 minute annealings at 400 C and 550 C_2. The deconvolution of signal into various valence contributions is shown

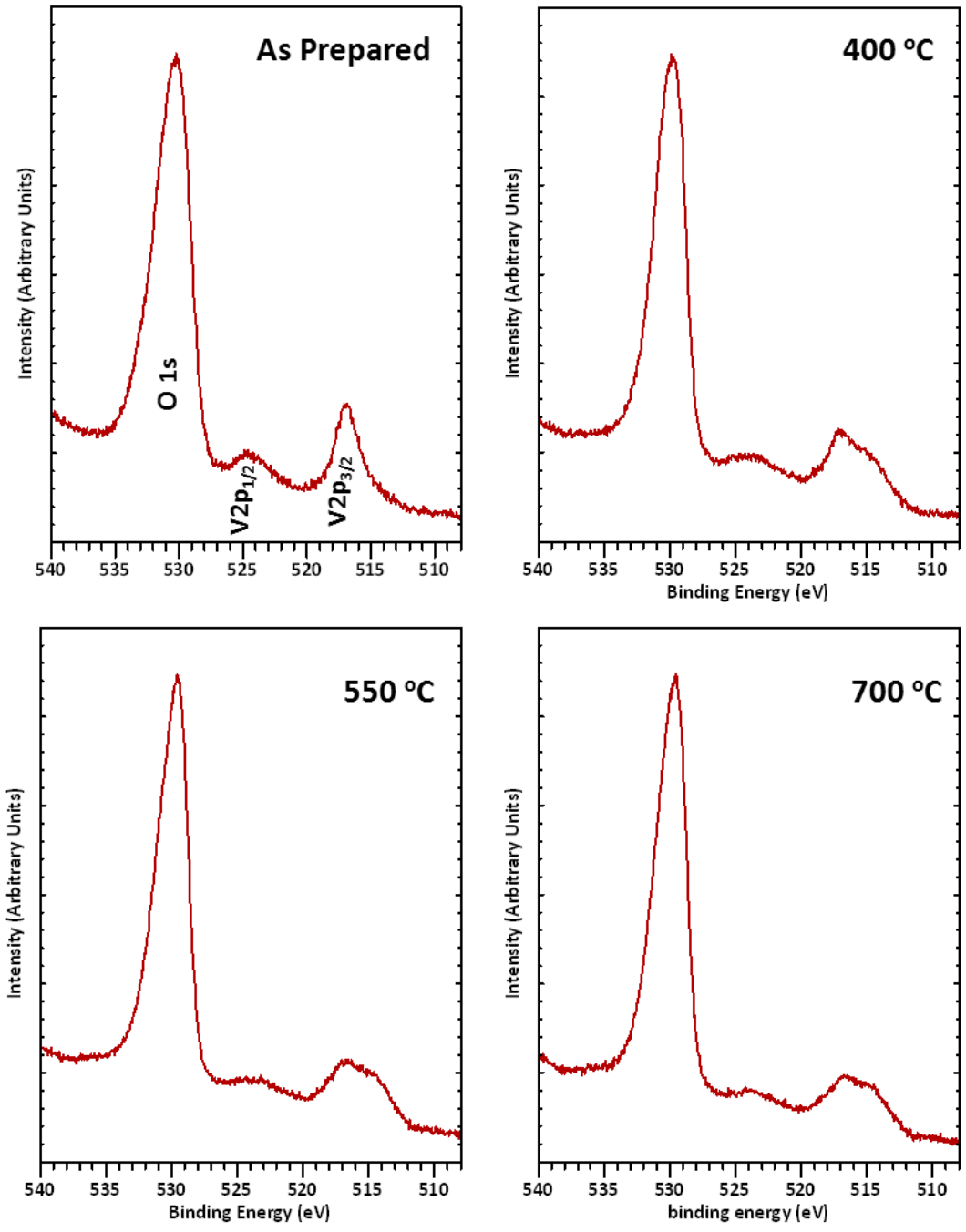


Figure 48: Left to Right: O 1s and V 2p core-level region XPS spectra of a Sr_2VMoO_6 tape cast pellet as prepared, and after 30 minute annealings at 400 C, 550 C and 700 C in 10^{-6} Torr H_2.

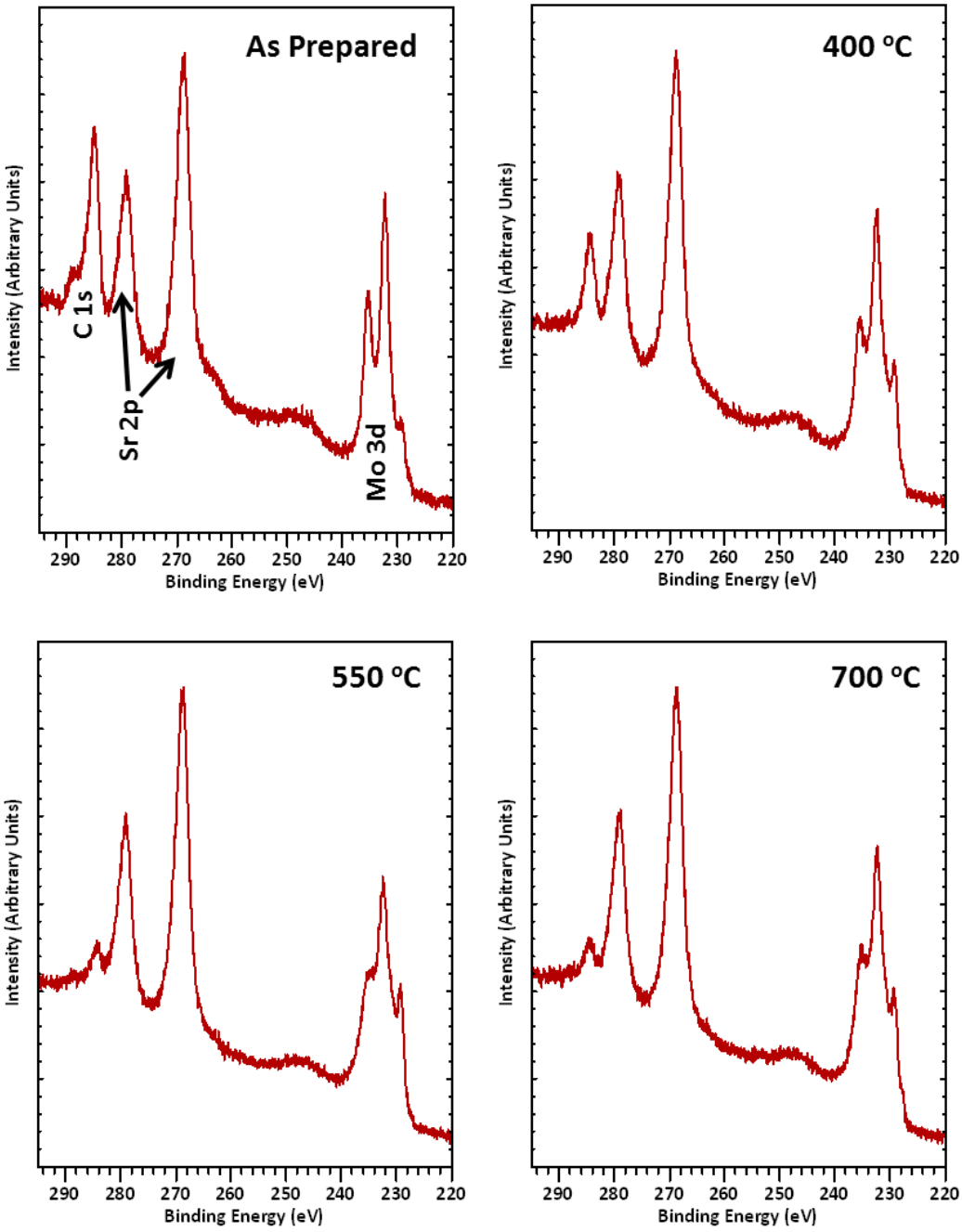


Figure 49: C 1s, Sr, 2p and Mo 3d core-level region XPS spectra of a Sr_2VMoO_6 tape cast pellet a) as prepare and after 30 minute annealings at b) 400 C, c) 550 C and d) 700 C in 10^{-6} Torr H_2

Table 6: XPS binding energies and valence contributions for $Sr_{2-x}VMoO_{6-\delta}$ tape cast discs as prepared and after annealing in a hydrogen environment

		Vanadium $2p_{3/2}$			Molybdenum $3d_{5/2}$		
Sample Condition	Compound	V(+5) BE = 517.2 eV	V(+4) BE = 515.8 eV	V(+3) BE = 515.3 eV	Mo(+6) BE = 235.5 eV	Mo(+5) BE = 231.0 eV	Mo(+4) BE = 230.0 eV
Prior to Annealing	$Sr_{2.0}VMoO_{6-y'}$	88.3%	11.7%	0.0%	85.4%	3.7%	10.9%
	$Sr_{1.9}VMoO_{6-y''}$						
	$Sr_{1.8}VMoO_{6-y'''}$						
400 C	$Sr_{2.0}VMoO_{6-y'}$	48.2%	27.3%	24.5%	64.9%	9.5%	25.6%
	$Sr_{1.9}VMoO_{6-y''}$						
	$Sr_{1.8}VMoO_{6-y'''}$						
550 C	$Sr_{2.0}VMoO_{6-y'}$	32.6%	30.4%	37.0%	66.1%	5.6%	28.3%
	$Sr_{1.9}VMoO_{6-y''}$						
	$Sr_{1.8}VMoO_{6-y'''}$						

4. Discussion

Solid state synthesis of $Sr_{2-x}VMoO_{6-\delta}$ samples exhibited high (1250-3000 S/cm @ 800˚C) metallic like conduction after thermal cycling in a wet reducing atmosphere. After thermal cycling in an environment of 2.9% H_2O/ 4.9%H_2/92.2%N_2, the conductivity values measured agree best with that reported at room temperature by Karen et. al. (18) as opposed to other referenced conductivities.

XRD of powders ground from samples before and after being subjected to the same conditions as conductivity tests indicate minor contributions from the $Sr_3V_2O_8$ and $SrMoO_4$ contamination phases in the bulk of the $Sr_{2-x}VMoO_{6-\delta}$ samples. However, XPS spectra of the surface of these samples prior to any additional treatment after sintering revealed a high (85-90%) content of the V^{+5} and Mo^{+6} valence states. These valence states are consistent with the presence of the highly insulating $Sr_3V_2O_8$ and $SrMoO_4$ phases. These valence states were found to be reduced upon annealing at temperatures

ranging between 400-500˚C, which would contradict the finding of Hui et al. (14), where $Sr_3V_2O_8$ was found to be redox stable. For vanadium during reduction the increase of the V^{+4} is consistent with the $SrVO_3$ system as well as the oxidation-state couple V^{+4}/Mo^{+4} in $Sr_{2.0}VMoO_{6.0}$, the increase of V^{+3} is consistent with the oxidation-state couple V^{+3}/Mo^{+5} in $Sr_{2.0}VMoO_{6.0}$. For molybdenum during reduction the increase of Mo^{+4} is consistent with the $SrMoO_3$ system, while the increase of Mo^{+5} is consistent with the oxidation-state couple V^{+3}/Mo^{+5} in $Sr_{2.0}VMoO_{6.0}$. The DC electrical conductivities of $Sr_3V_2O_8$ and $SrMoO_4$ are semi-conductor like, while $SrVO_3$, $SrMoO_3$ and $Sr_{2.0}VMoO_{6.0}$ exhibit metallic conduction with values many orders of magnitude higher than their oxidized counterparts.

During the thermal cycle from 50˚C-> 400˚C -> 50˚C a transition was observed in the trend of conductivity values. All samples exhibited semi-conductor like conduction, however settle to an average value ~4000% higher than at the start of the cycle. This temperature region is consistent with the temperature region reported for the reduction of MoO_4 to MoO_3 in a reducing environment (29). During the thermal cycle from 50˚C-> 850˚C -> 50˚C all samples exhibited semi-conductor like conduction upon heating and metallic like conduction upon cooling. This could correspond to the findings of Hiu et al. (16), were the doping of $SrTiO_3$ greatly increased the conductivity and produced metallic like behavior of the perovskite due to the reduction of B-site cation valance states. The higher conductivity exhibited by $Sr_{1.8}VMoO_{6-\delta}$ at temperatures up to 600˚C, where semiconductor behavior is dominate, can be explained through the greater amount of A-site deficiencies leading to a greater amount of ionic conduction. However, as found by

Li et al. (15), A-site deficiencies can also lead to lower amounts of electronic conductivity. This can explain higher conductivity exhibited by $Sr_{1.9}VMoO_{6-\delta}$ after 600˚C, where metallic behavior is dominate, and indicates that an optimized A-site deficient double perovskite structure could exist between $Sr_2VMoO_{6-\delta}$ and $Sr_{1.8}VMoO_{6-\delta}$.

TGA measurements confirm that samples are reducing in weight over a cycle from room temperature to 800 ˚C and back to room temperature. It is unclear if this final change is due to a new phase of reduction and/or a continuation of the reduction seen in lower temperature cycles. It is important to note that the partial pressure of oxygen ranges from ~10^{-33} to ~10^{-19} bar between 400 ˚C and 850 ˚C. XRD, XPS, TGA and referenced publications are consistent with the conclusion that reduction of highly insulating impurity phases for $Sr_{2-x}VMoO_{6-\delta}$ materials synthesized by methods described here leads to a metallic like material with high conductivity. The variability in reported conductivities for these materials is most likely due to the amount of these contaminate phases related to differences in processing techniques and the environmental conditions of the conductivity tests.

5. Conclusions

Electrical conductivity of $Sr_{2-x}VMoO_{6-y}$ (x=0.0, 0.1, 0.2) solid oxide fuel electrode material has been investigated in a reducing atmosphere at temperatures up to 800 ^{0}C. Elemental valence states were identified through X-ray photoemission on the double perovskite material before and after annealing in a hydrogen environment. Samples exhibited metallic conduction with electrical conductivities of 1250 S/cm ($Sr_2VMoO_{6-y'}$),

2530 S/cm ($Sr_{1.8}VMoO_{6-y''}$) and 3610 S/cm ($Sr_{1.9}VMoO_{6-y'''}$) at 800 ^{0}C in 5%H_2/95%N_2. A highly insulating phase begins to reduce between 400 and 500 ^{0}C in a 5%H_2/95%N_2 environment, as confirmed by X-ray photoemission and thermal gravimetric analysis. This reduction leads to a large increase in electrical conductivity.

The electrical conductivity of $Sr_{2-x}VMoO_{6-\delta}$ materials at 800 ˚C in a 2.9% H_2O/ 4.9%H_2/92.2%N_2 environment exceeds that reported for state of the art Ni-YSZ fuel electrodes by a factor of ~1.25-3 at the same temperature in similar environments. Polycrystalline $Sr_{1.9}VMoO_{6-\delta}$ samples exhibited higher conductivity than that reported for $SrMoO_3$ polycrystalline samples. A single crystal sample of $Sr_{1.9}VMoO_{6-\delta}$ would be a candidate for exhibiting the highest known conducting oxide.

Acknowledgements

This work was supported by NASA EPSCoR under grant #NNX09AP73A

Supplemental Material for "Electrical Conductivity of Sr2-xVMoO6 (x=0.0, 0.1, 0.2) Double Perovskite Solid Oxide Fuel Cell Fuel Electrode"

The conductivity tests indicate that all $Sr_{2-x}VMoO_{6-\delta}$ pellets are stable over 100 hours of exposure to a reducing environment at 800°C, as shown in Figure 50. All of the tested pellets indicate that there is a rapid gain in conductivity when 800°C is reached and the rapid gain lasts for less than 24hr. $Sr_{1.9}VMoO_{6-\delta}$ and $Sr_{1.8}VMoO_{6-\delta}$ pellets continue to slightly increase in conductivity over the 100 hour exposure, while the $Sr_2VMoO_{6-\delta}$ pellet is steady after the initial rapid gain. The results of the 100hr conductivity tests suggest

that $Sr_{2-x}VMoO_{6-\delta}$ can provide adaquate conduction as a SOFC fuel electrode without the degridation in electrical conductivity observed in Ni/YSZ cermets.

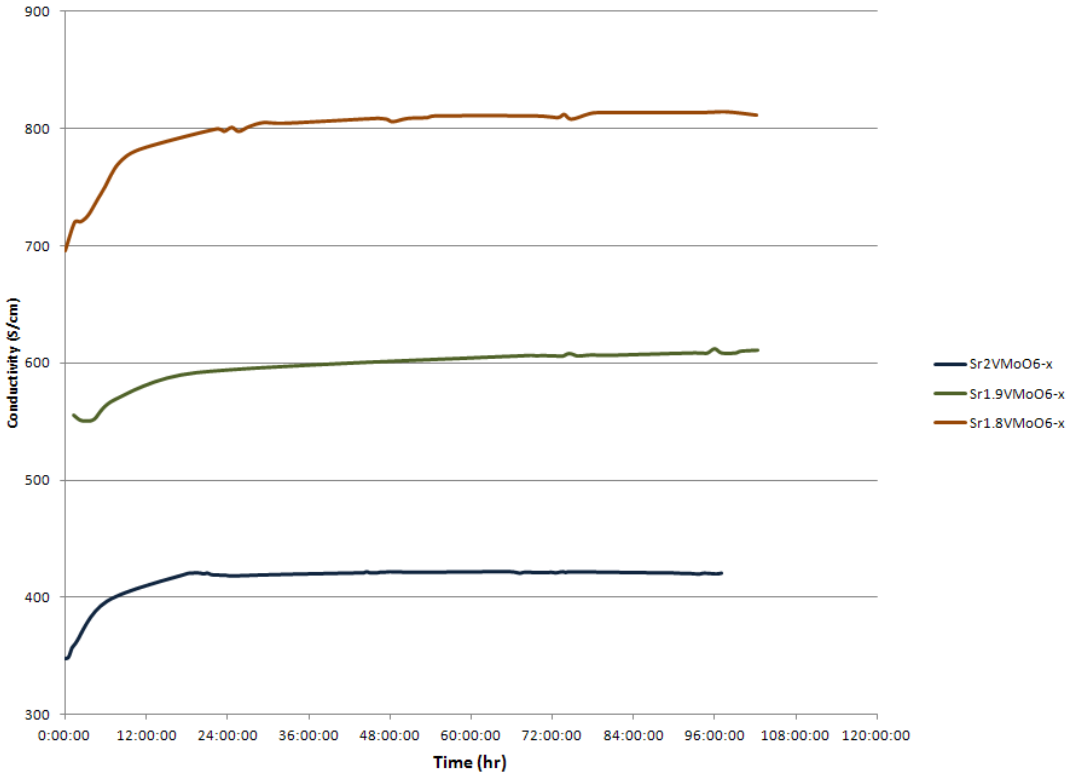


Figure 50: Conductivity vs. Time for sintered $Sr_{2-x}VMoO_{6-\delta}$ pellets

A Linseis Thermowaage L 81, with a resolution of 1µg, was utilized to perform thermal gravimetric analysis (TGA) to determine the weight loss due to the reduction of the $Sr_{2-x}VMoO_{6-\delta}$ sintered powder. A Pfeiffer Vacuum ThermoStar Gas Analysis System, with a resolution of 1 amu was also utilized for mass spectroscopy during this testing for oxygen level observation. The experiment was performed in a reducing atmosphere (5%H_2 and 95%N_2), from room temperature to 850˚C and back down to room temperature at a heating rate of 2˚C/min. Multiple tests were performed, for each of varying double perovskite stoichiometries due to differing oxygen partial pressures,

and an average value was found. An example of TGA tested $Sr_{1.9}VMoO_{6-\delta}$ sintered powder is shown in Figure 51. This indicates that the weight gain and loss is influenced greatly by oxygen partial pressure.

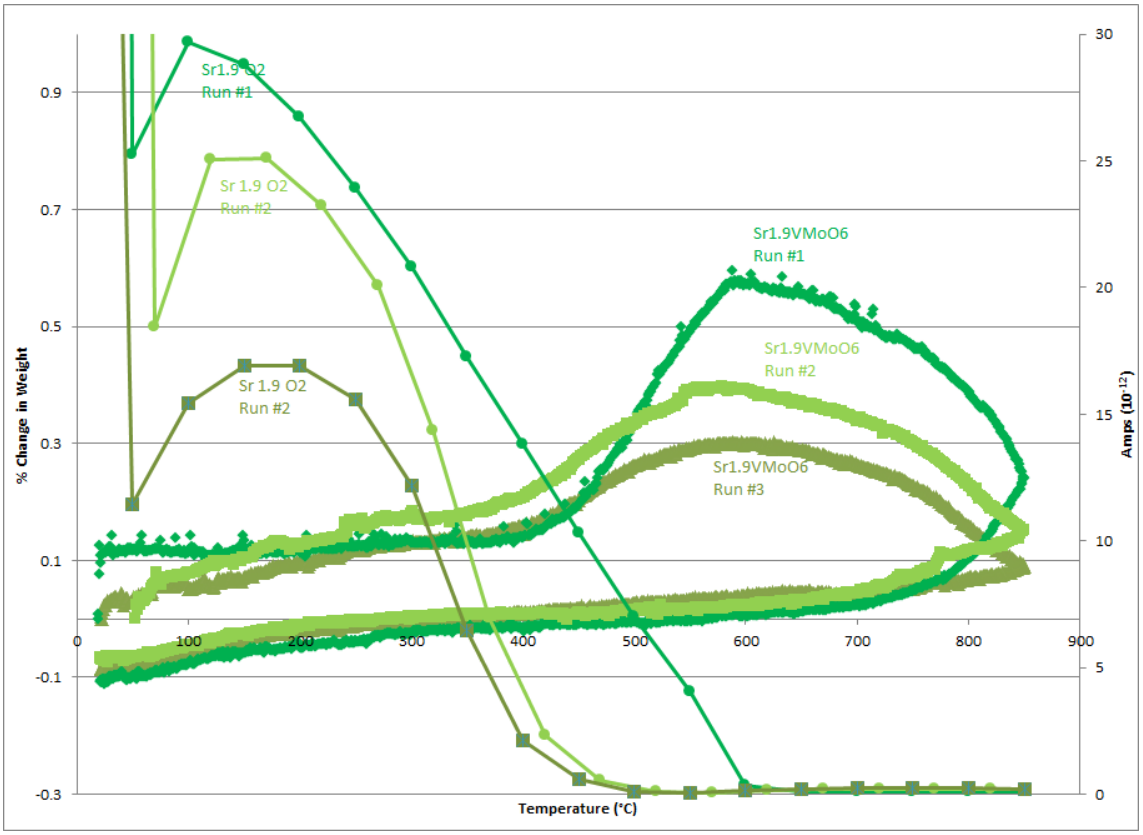


Figure 51: % change in weight of $Sr_{1.9}VMoO_{6-\delta}$ of sintered powder from 30°C up to 850°C and back down to 30°C at 2°C/min. Oxygen level in amps (10^{-12}) vs. temperature in the furnace is also shown

CHAPTER FOUR

FUEL ELECTRODE PERFORMANCE OF Sr_2VMoO_6 DOUBLE PEROVSKITES

Contribution of Authors and Co-Authors

Manuscripts in Chapters 2, 3, and 4

Author: Adam Weisenstein

Contributions: Performed the synthesis and testing of the SOFCs. Provided the initial manuscript.

Co-Author: Stephen Sofie

Contributions: Collaborated on the conception and design of the investigation and provided important intellectual content to the manuscript.

Manuscript Information Page

Adam Weisenstein, Stephen Sofie
Journal of the Electrochemical Society
Status of Manuscript:
_X__ Prepared for submission to a peer-reviewed journal
____ Officially submitted to a peer-review journal
____ Accepted by a peer-reviewed journal
____ Published in a peer-reviewed journal

Journal of the Electrochemical Society
To be submitted December, 2012

CHAPTER FOUR

FUEL ELECTRODE PERFORMANCE OF Sr_2VMoO_6 DOUBLE PEROVSKITES

Abstract

In this study, the fabrication and testing of $Sr_2VMoO_{6-\delta}$ perovskites as fuel electrodes was investigated. $Sr_2VMoO_{6-\delta}$ fuel electrodes were synthesized utilizing both solid state synthesis and solution synthesis. The solid state synthesized powders were applied by screen printing, however a problem that was encountered when utilizing the double perovskite fuel electrode with the YSZ electrolyte was the delamination of the electrode from the electrolyte during the sintering of the two layers. The SEM elemental line scans indicated that there is no major migration of the cation elements around the interface. This would indicate that there is not a large amount of $SrZrO_3$ formation between the YSZ and $Sr_2VMoO_{6-\delta}$. However, an anion reaction between YSZ and $Sr_2VMoO_{6-\delta}$ layers could result in the formation of the $SrMoO_4$ scheelite structure. The infiltrated SOFC with the solution $Sr_2VMoO_{6-\delta}$ was able to produce max power density of 194.8mW/cm^2 at 0.87V. However, upon further XRD analysis, the perovskite phase was not fully developed at 850°C, which lead to the investigation into the infiltration of $SrBO_{4-\delta}$ fuel electrodes. Both of these electrodes performed well despite the lack of cation infiltration.

Keywords: Solid Oxide Fuel Cell; Double Perovskite; Infiltration; Scheelite

1. Introduction

Single phase Mixed Ionic and Electronic Conductors (MIEC) have been investigated to replace the traditional Ni/Yttria-Stablized Zirconia (YSZ) cermet fuel electrodes. The most intriguing of these MIEC's is the double perovskite structure. The double perovskite structure has 12 coordinate A-sites and 6 coordinate B-sites, including two ordered cations. The double perovskite structures, $Sr_2Mg_{1-x}Mn_xMoO_{6-\delta,}$ and $Sr_2Fe_{4/3}Mo_{2/3}O_{6-\delta}$, have shown electrical conductivity at high as 10 S/cm and 16 S/cm at 800ºC, respectively (25; 26). Double perovskites $Sr_2Mg_{1-x}MnMoO_6$ were tested as fuel electrodes in an electrolyte supported SOFC with a 300µm Lanthanum Strontium Gallium Magnesium Oxide (LSGM) electrolyte and a $SrCo_{0.8}Fe_{0.2}O_{3-\delta}$ cathode. Sr_2MgMoO_6 produced a maximum power density of 968mW/cm^2 at 850°C, 838mW/cm^2 at 800°C, and 642mW/cm^2 at 750°C and Sr_2MnMoO_6 produced a maximum power density of 658mW/cm^2 at 800°C and 467W/cm^2 at 750°C (25). $Sr_2Fe_{4/3}Mo_{2/3}O_{6-\delta}$ was also tested in an electrolyte supported SOFC with a 300µm LSGM electrolyte and a Lanthanum Strontium Cobalt Ferrite (LSCF) cathode. $Sr_2Fe_{4/3}Mo_{2/3}O_{6-\delta}$ produced a maximum power density of 547mW/cm^2 at 800°C, 392mW/cm^2 at 750°C, and 268mW/cm^2 at 700°C (26). These power densities compare very favorably to H.C. Starck semi-commercial fuel electrode supported fuel cells that produce power densities in the 200 to 500mW/cm^2 range (63). The double perovskite $Sr_2VMoO_{6-\delta}$ has demonstrated superior conductivity to $Sr_2Mg_{1-x}Mn_xMoO_{6-\delta,}$ and $Sr_2Fe_{4/3}Mo_{2/3}O_{6-\delta}$ at 12,000 S/cm, however has not been investigated as a fuel electrode in an electrolyte

supported SOFC design (18). Therefore, the implementation of $Sr_2VMoO_{6-\delta}$ double perovskite as a fuel electrode will be the focus of this investigation.

2. Experimental Procedure

As received Alfa Aesar $Sr_2VMoO_{6-\delta}$, precursor powders were prepared by solid state synthesis, as shown in Table 7, for use as fuel electrode screen printing ink. These powders were calcined for 6 hours at 1000°C, reground and then sintered at 1300°C for 20 hours in a wet reducing (5%H_2 95%N_2) atmosphere, utilizing a MTI GSL 1500X tube furnace. The powder was then combined with carbon spheres, alpha terpineol, ethyl cellulose, and oleic acid to form and ink for electrode application. As received LSCF, was also made into a screen printing paste using the same method. The solution synthesis was a combination deionized water, molybdenum chloride, vanadium chloride, and strontium nitrate, as shown in Table 7. The air electrode infiltration was a solution of lanthanum nitrate, strontium nitrate, and manganese nitrate, shown in Table 7.

Table 7: Fuel Electrode Precursors

Precursor	**Chemical Formula**	**Company**	**Stock #**
Strontium Carbonate	$SrCO_3$	Alfa Aesar	33392
Vanadium Dioxide	VO_2	Alfa Aesar	22957
Molybdenum Dioxide	MoO_2	Alfa Aesar	48117
Molybdenum Chloride	$MoCl_5$	Alfa Aesar	11832
Vanadium Chloride	VCl_3	Alfa Aesar	14039
Strontium Nitrate	$Sr(NO_3)_2$	Alfa Aesar	12232
Manganese Nitrate Hydrate	$Mn(NO_3)_2 *XH_2O$	Alfa Aesar	87848
Lanthanum Nitrate Hexahydrate	$La(NO_3)_2 *6H_2O$	Alfa Aesar	12915

Purchased YSZ electrolytes, from Fuel Cell Materials Inc., were used for both screen printing and infiltration methods. The infiltrated cell required a porous YSZ scaffold which was accomplished by aerosol spraying the YSZ electrolyte with a 50/50 volume percentage of carbon spheres and YSZ. The scaffold was then sintered at 1220°C for 1 hour at a rate of 2°C/min. An example of a porous YSZ scaffold applied by aerosol spraying is shown in Figure 52. The scaffold was then infiltrated with the solution precursors by capillary effects and then decomposed at 500°C for 30 seconds for each infiltration. The air electrode and fuel electrode was screen printed onto the YSZ electrolyte and sintered at 1100°C for 2 hours. The SOFC testing was accomplished by connecting inconel platens to silver mesh via silver oxide paste and connecting the SOFC to the silver mesh porous silver oxide ink. Power testing was conducted at a temperature of 850°C, where voltage verses current was measured to determine the power per area output of the fuel cell.

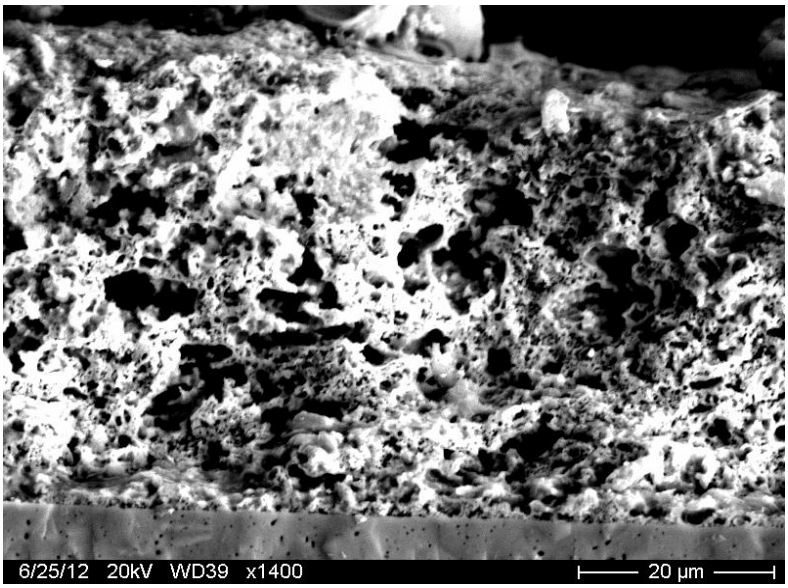


Figure 52: Porous YSZ scaffold

3. Results and Discussion

3.1 YSZ Electrolyte Supported SOFC

A problem that was encountered when utilizing the double perovskite fuel electrode with the YSZ electrolyte was the delamination of the electrode from the electrolyte during the sintering of the two layers, as shown in Figure 53. The delamination could be caused by a reaction between the YSZ electrolyte and the $Sr_2VMoO_{6-\delta}$ fuel electrode, and/or a difference in coefficient of thermal expansion (CTE) between the two materials. To investigate the reaction between the electrode and the electrolyte, a dual layer pellet was pressed containing YSZ and $Sr_2VMoO_{6-\delta}$ and then sintered in a reducing (5%H_2 and 95%N_2) atmosphere for 10hr. The pellet was then cross sectioned and analyzed in a JEOL JSM-6100 Scanning Electron Microscope (SEM), where elemental line scans were performed at the interface of the YSZ and $Sr_2VMoO_{6-\delta}$ layers. The SEM elemental line scan, as shown in Figure 54, indicates that there is no major migration of the cation elements around the interface. This would indicate that there is not a large amount of $SrZrO_3$ formation between the YSZ and $Sr_2VMoO_{6-\delta}$ layers, which would agree with the findings of Aguadero et al. (64). However, an anion reaction between YSZ and $Sr_2VMoO_{6-\delta}$ layers could result in the formation of the $SrMoO_4$ scheelite structure as observed by Lopez et al. (65), which cannot be detected through elemental line scans. Aguadero et al. also found that the CTE of the $Sr(V_{0.5}Mo_{0.}5)O_3$ perovskite was 12.6 ppm/K, which would correspond well to the CTE of YSZ (66).

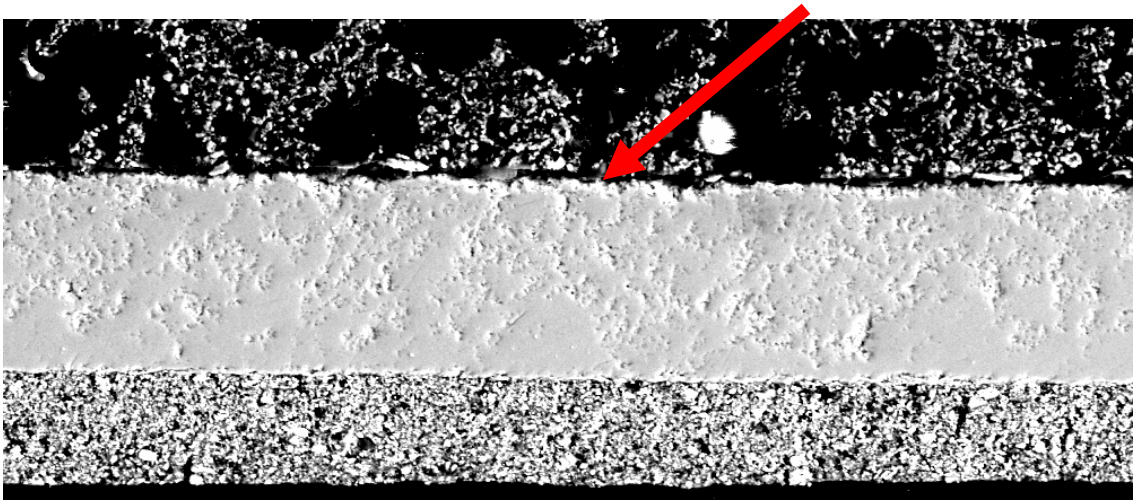


Figure 53: Delamination of the Sr_2VMoO_6 fuel electrode from the YSZ electrolyte after sintering, as indicated by the red arrow

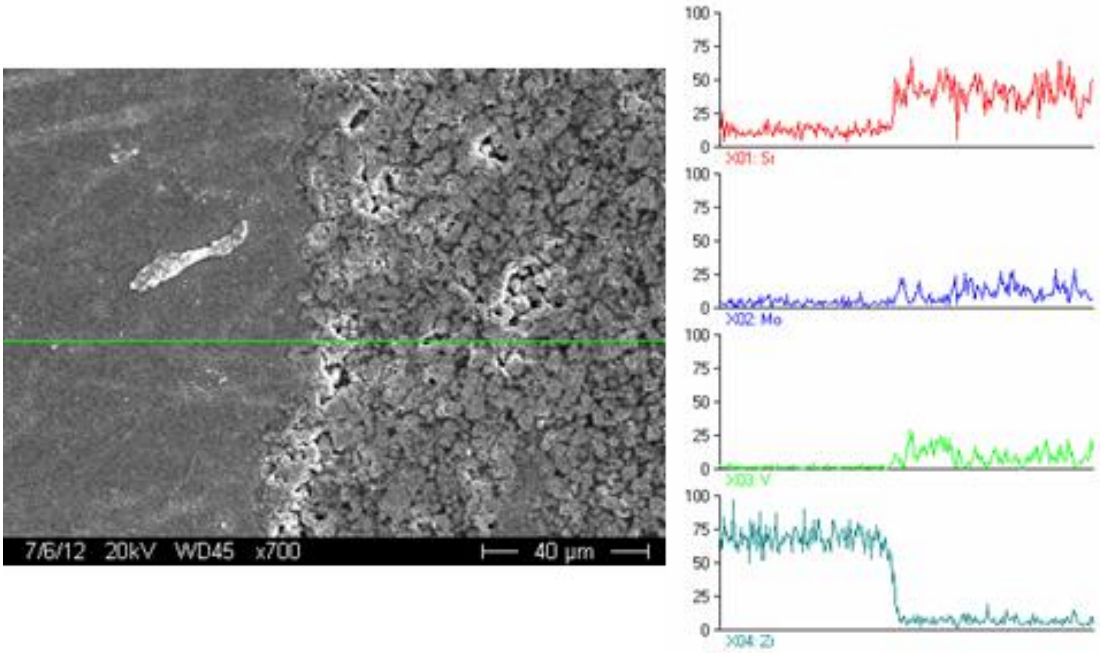


Figure 54: SEM elemental line scan of the interface between the YSZ and double perovskite layer

3.2 $Sr_{2-x}VMoO_{6-\delta}$ Infiltration

The delamination problem can be overcome by utilizing an infiltration process for applying an aqueous solution of $Sr_{2-x}VMoO_{6-\delta}$ precursors to a porous YSZ scaffold, therefore eliminating any CTE mismatch or shear stress caused by phase transition between the fuel electrode material and the electrolyte. The power density vs. voltage was calculated and graphed, as shown in Figure 55, for the $Sr_{2-x}VMoO_{6-\delta}$ chloride precursor infiltrated SOFC. The SOFC was able to produce a peak power output of 917.5mW and a max power density of 194.8mW/cm^2 at 0.87V. These initial results were very encouraging and compare well to commercial SOFCs. SEM elemental mapping was also conducted on the infiltrated cells. As shown in Figure 56, an SOFC was fabricated with a $Sr_2VMoO_{6-\delta}$ infiltrated fuel electrode and aerosol sprayed $Sr_2VMoO_{6-\delta}$ top coat for elemental contrasting purposes. As shown in Figure 57, vanadium and molybdenum are prevalent in the aerosol sprayed layer; however the elemental mapping indicates that the infiltrated layer contains little amounts of the B-site cations after 15 infiltrations.

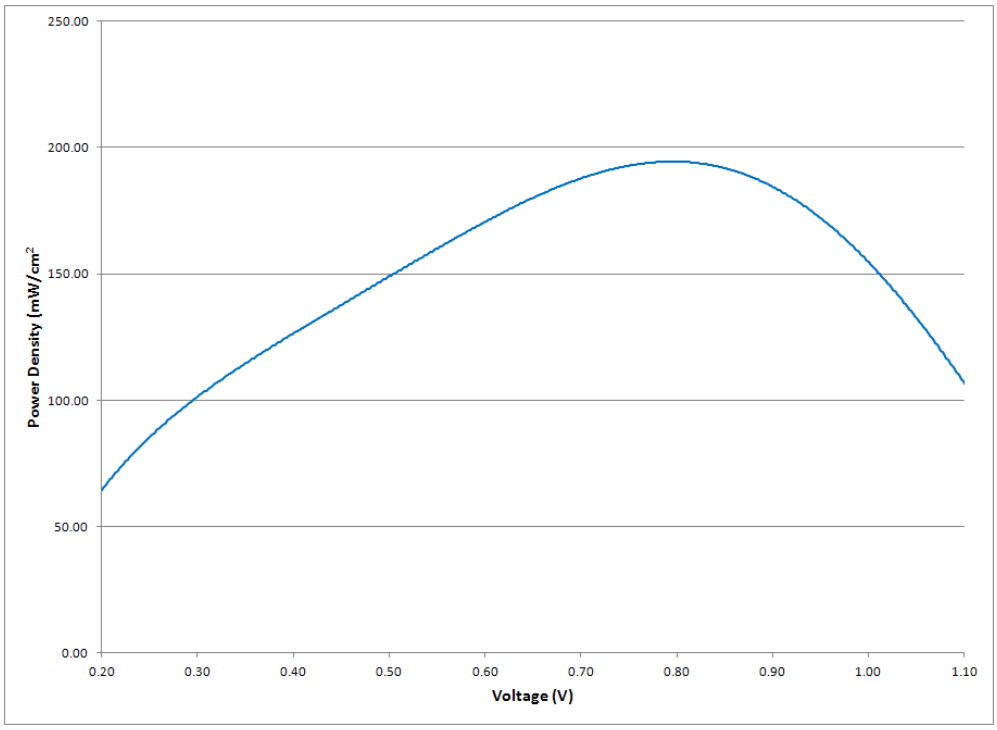


Figure 55: Voltage vs. Current for a Sr_2VMoO_6/YSZ/LSM SOFC at 850°C

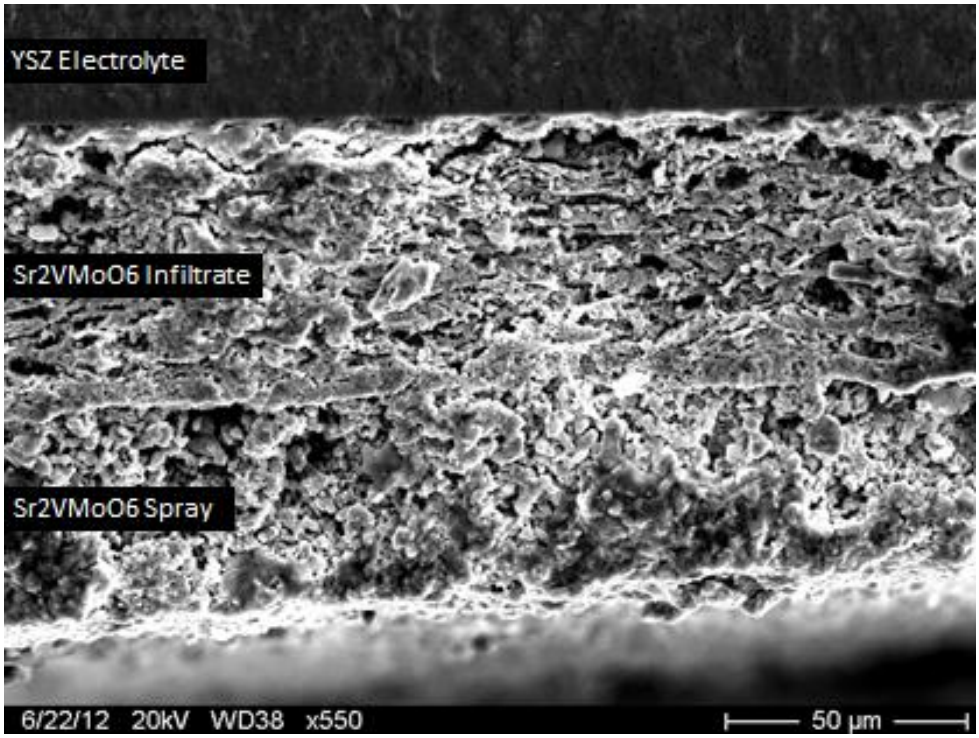


Figure 56: Microstructure of a Sr_2VMoO_6 dual layer fuel electrode

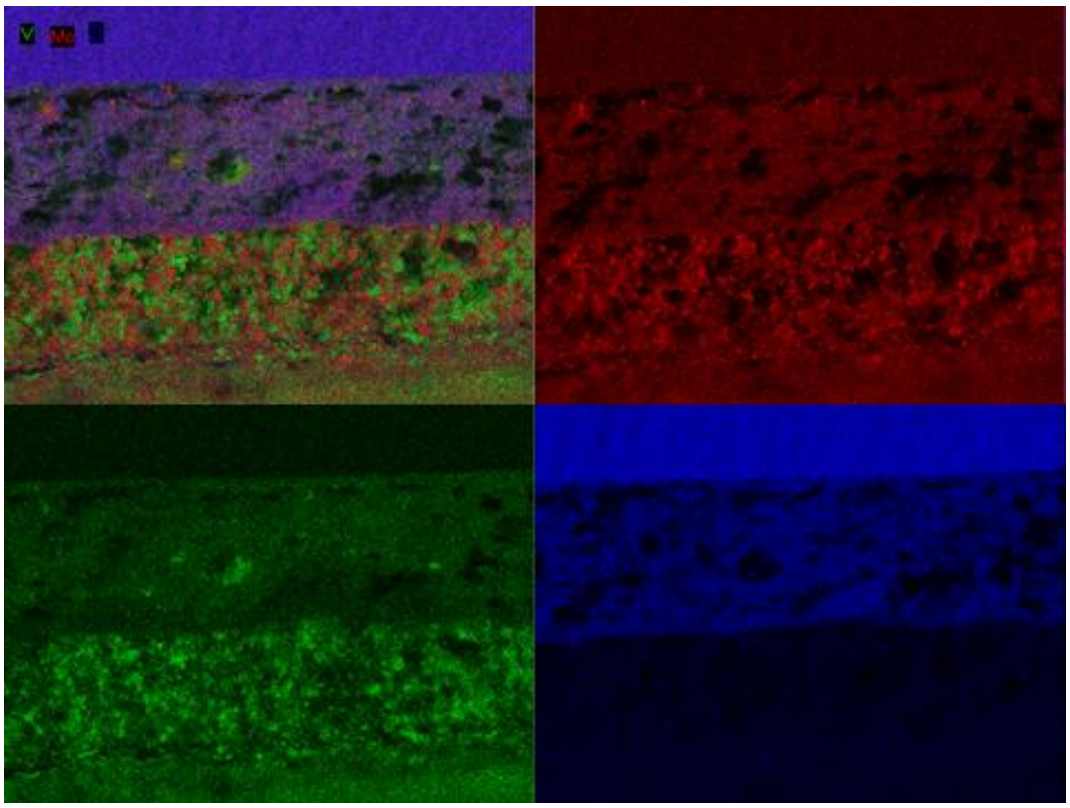


Figure 57: Elemental mapping of the dual layer fuel electrode

XRD was conducted on the $Sr_{2-x}VMoO_{6-\delta}$ infiltration solution after drying and reducing the powders for 10 hours at 850˚C, which would represent the conditions in SOFC operation. As shown in Figure 58, the XRD pattern for the reduced $Sr_{2-x}VMoO_{6-\delta}$ solution indicates that mostly the scheelite structure is formed along with small amounts of double perovskite and molybdenum vanadium oxides. This indicates that the double perovskite structure is not achievable with in-situ heating.

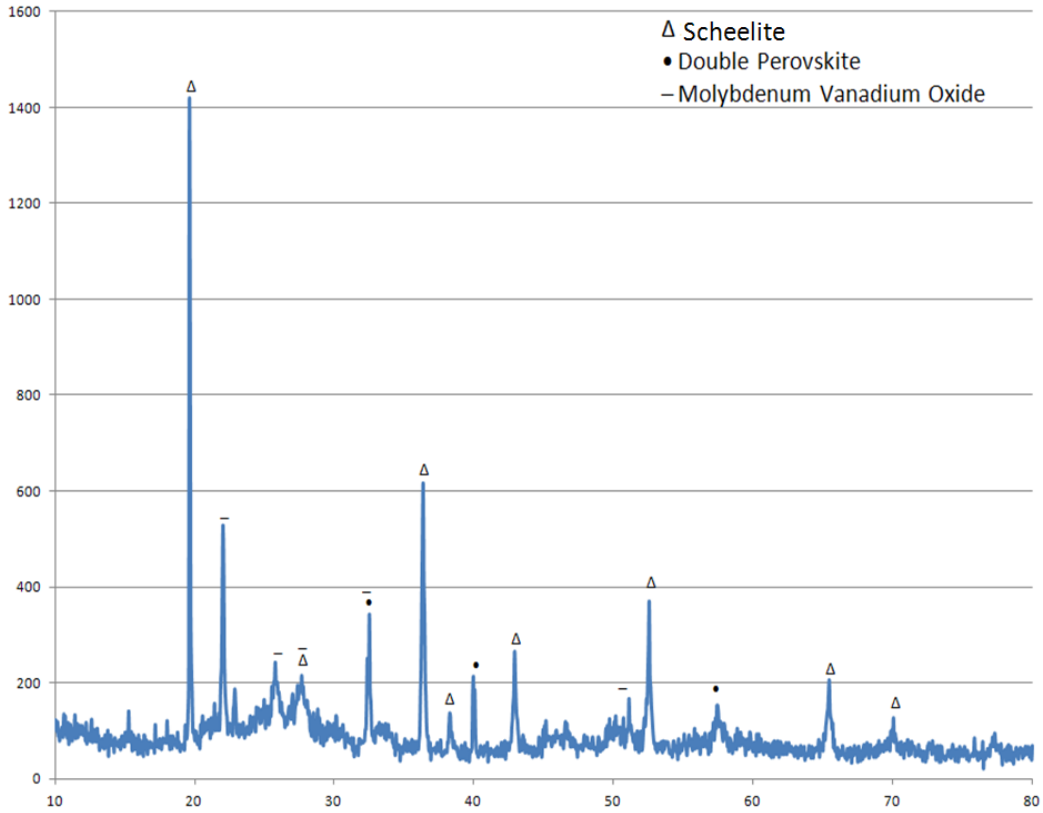


Figure 58: XRD pattern for the $Sr_{2-x}VMoO_{6-\delta}$ solution

Another method of synthesizing the desired $Sr_{2-x}VMoO_{6-\delta}$ double perovskite at lower sintering temperatures is to introduce a metal element that will act as a reduction agent. The reduction agent would form an oxide from reacting with the aqueous precursors, therefore inducing the desired oxidation states needed to form the double perovskite, as discussed in the development of the all ceramic fuel electrode section. An example of this reaction is shown in Equation 8. For this reaction to happen, the Gibbs free energy of the oxidation of the introduced element needs to be much lower than the MoO_3 formation that leads to the undesired scheelite structure. The Gibbs free energy of MoO_3 is -668.017 KJ/mol (67), which is higher than Ti to TiO, as shown in Figure 59. A 19.05mm (3/4in) pellet containing a mixture of MoO_3 and TiH_2 in equal weight

percentages was uniaxially pressed at 250Mpa and then thermally treated at 850°C for 10 hours in a reducing environment, as would be encountered during SOFC operation. The pellet was then ground into a powder with the use of a mortar and pestle and analyzed through XRD. As shown in Figure 60, MoO_3 was still present, however the desired reduction to MoO_2 was observed along with the oxidation of Ti.

Equation 8: $MoO_3 + Ti \rightarrow MoO_2 + TiO$

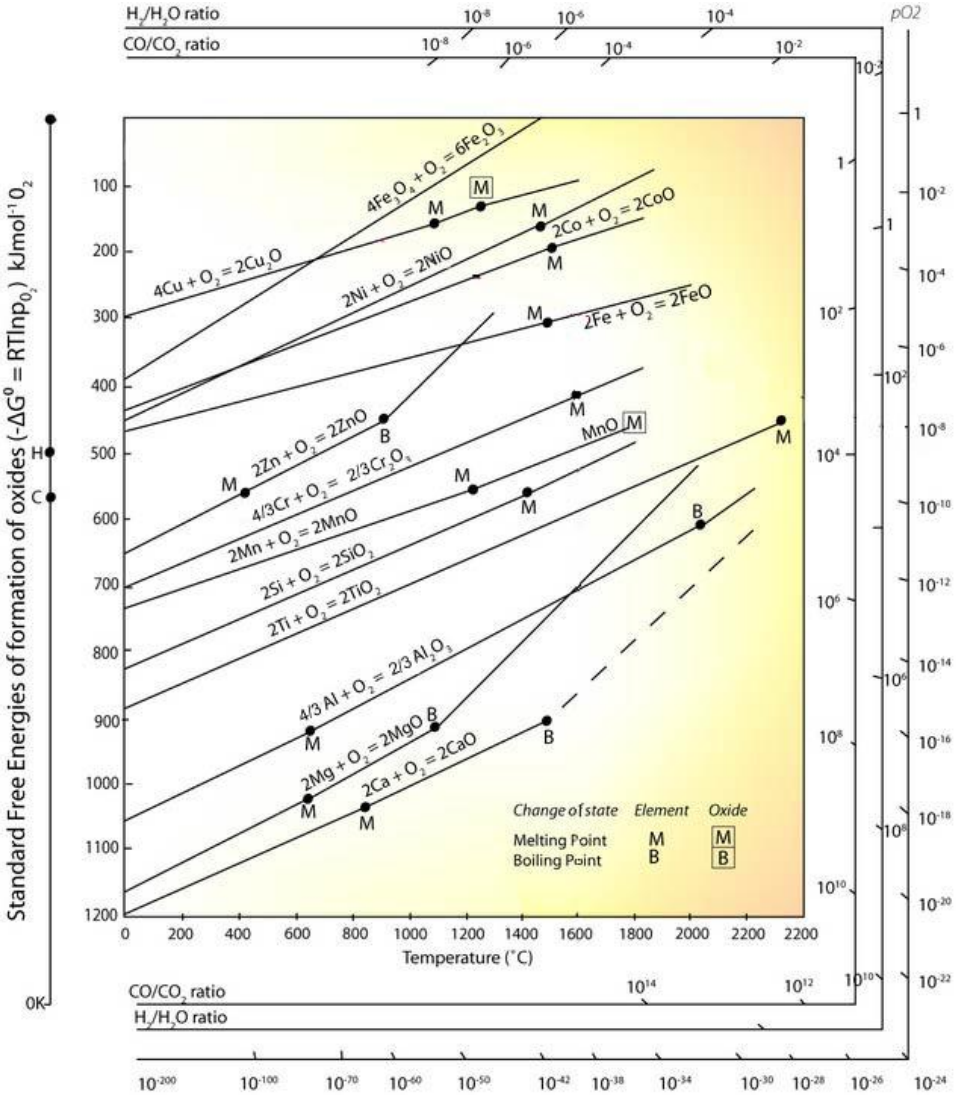


Figure 59: Ellingham Diagram (68)

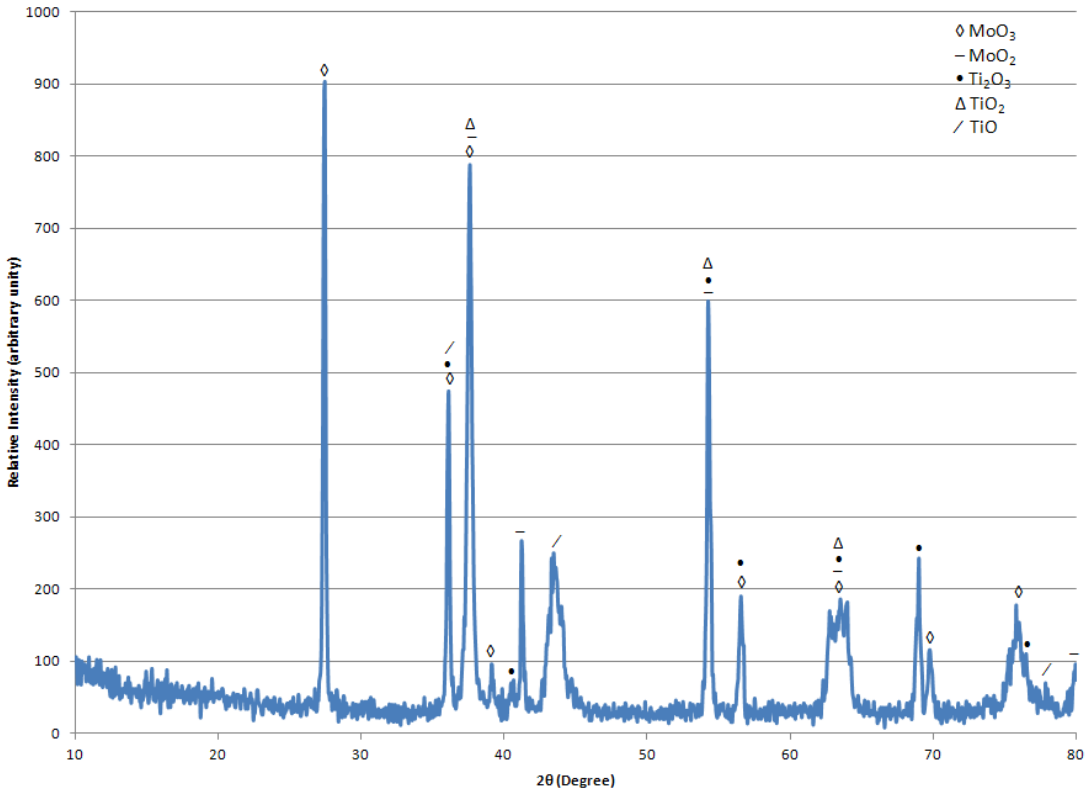


Figure 60: XRD pattern for MoO_3 + TiH_2

3.3 $SrMoO_{4-\delta}$ and $SrVO_{4-\delta}$ Infiltration

Due to the XRD results and initial SOFC testing; an investigation into SOFC testing of $SrMoO_{4-\delta}$ and $SrVO_{4-\delta}$ scheelite-type aqueous chloride solutions for infiltration of the fuel electrode was conducted. As shown in Figures 61 and 62, $SrMoO_{4-\delta}$ and $SrVO_{4-\delta}$ performed well in initial testing and should be further investigated as fuel electrode materials. However, as found in the testing of $Sr_2VMoO_{6-\delta}$, the infiltration of the elements was very low. As shown in both Figures 63 and 64, the elemental line scans of the fuel electrodes indicate relatively small amounts of molybdenum and vanadium, respectively.

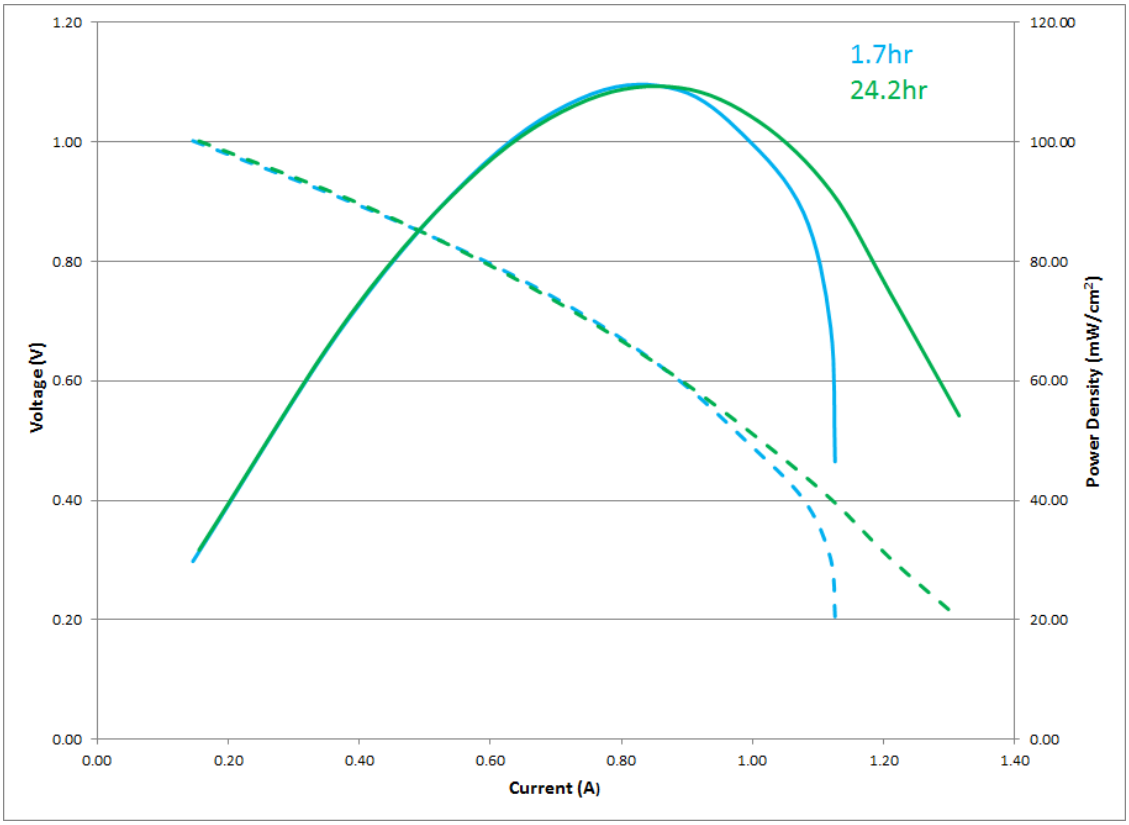


Figure 61: SOFC performance of $SrMoO_{4-\delta}$ infiltrated fuel electrode

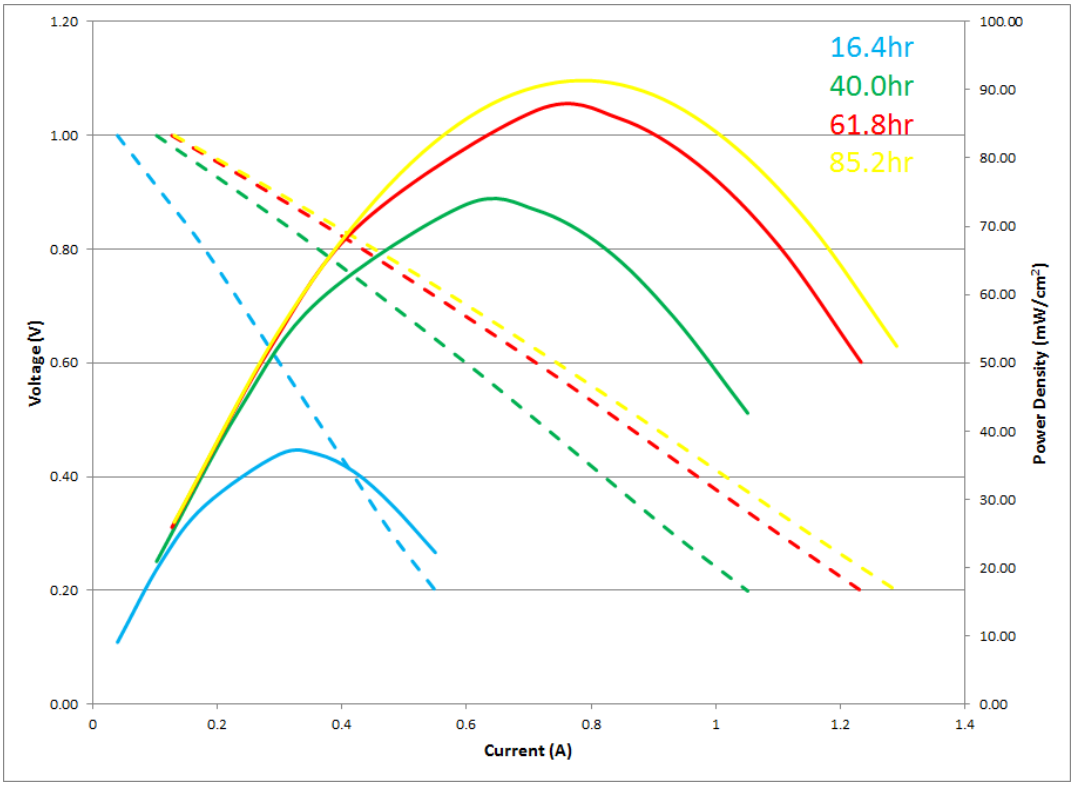


Figure 62: SOFC performance of $SrVO_{4-\delta}$ infiltrated fuel electrode

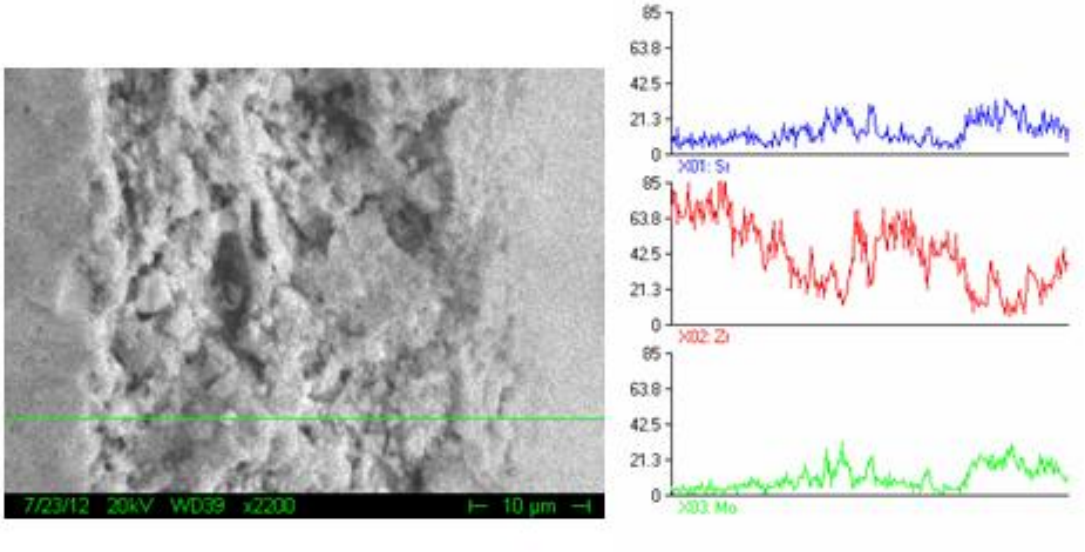


Figure 63: Elemental line scan of an infiltrated $SrMoO_{4-\delta}$ fuel electrode

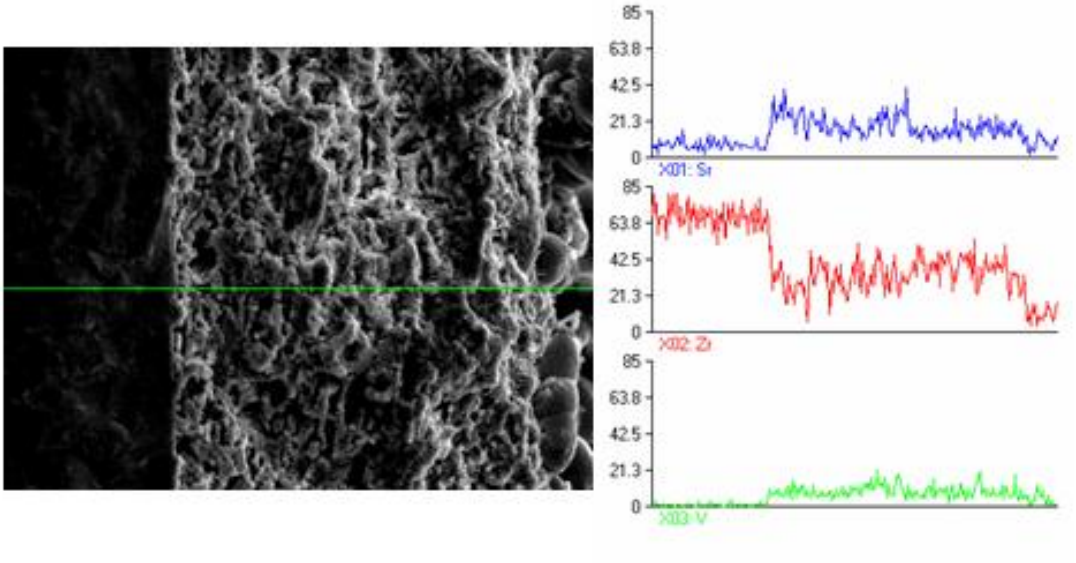


Figure 64: Elemental line scan of an infiltrated $SrVO_{4-\delta}$ fuel electrode

4. Conclusion

$Sr_2VMoO_{6-\delta}$ fuel electrodes were synthesized utilizing both solid state synthesis and solution synthesis. A problem that was encountered when utilizing the screen printed double perovskite fuel electrode with the YSZ electrolyte was the delamination of the electrode from the electrolyte during the sintering of the two layers. The SEM elemental line scans indicated that there was no major migration of the cation elements around the interface. This would indicate that there is not a large amount of $SrZrO_3$ formation between the YSZ and $Sr_2VMoO_{6-\delta}$. However, an anion reaction between YSZ and $Sr_2VMoO_{6-\delta}$ layers could result in the formation of the $SrMoO_4$ scheelite structure.

The infiltrated SOFC with the solution $Sr_2VMoO_{6-\delta}$ was able to produce max power density of 194.8mW/cm^2 at 0.87V. However, upon further XRD analysis, the perovskite phase was not fully developed at 850°C, which lead to the investigation into

utilizing a reduction agent and the infiltration of $SrBO_{4-\delta}$ fuel electrodes. A 19.05mm (3/4in) pellet containing a mixture of MoO_3 and TiH_2 was sintered in a reducing environment and MoO_3 was still present, however the desired reduction to MoO_2 was observed along with the oxidation of Ti. $SrMoO_{4-\delta}$ and $SrVO_{4-\delta}$ infiltrated fuel electrodes performed well in initial testing and should be further investigated as fuel electrode materials, as the infiltration of the elements was very low.

Supplemental Material for "Fuel Electrode Performance of Sr2VMoO6 Double Perovskites"

Physical Vapor Deposition of YSZ

YSZ was also applied to the double perovskite surface through the use of Physical Vapor Deposition (PVD) to combat the issue of high temperatures sintering of YSZ. An SEM image of an YSZ vapor deposition coated pellet is shown in Figures 65 and 66, where Figure 65 shows the top of the pellet and Figure 66 shows the elemental mapping of the same section. The elemental mapping indicates that a dense layer of 0.5μm thick YSZ, as shown in red, is achievable by the vapor deposition method. However, initial SOFC testing showed low open circuit voltage, which is an indication of gas diffusion through the electrolyte. These problems led to the determination that the physical vapor deposition of YSZ on a double perovskite substrate would not be a viable option.

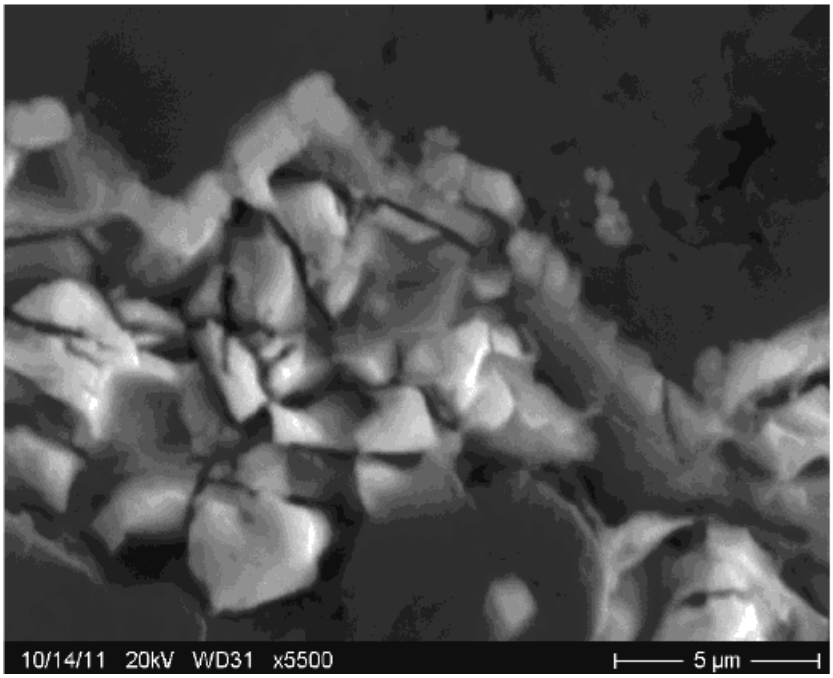


Figure 65: SEM image of a YSZ PVD layer on a Sr_2VMoO_6 pellet

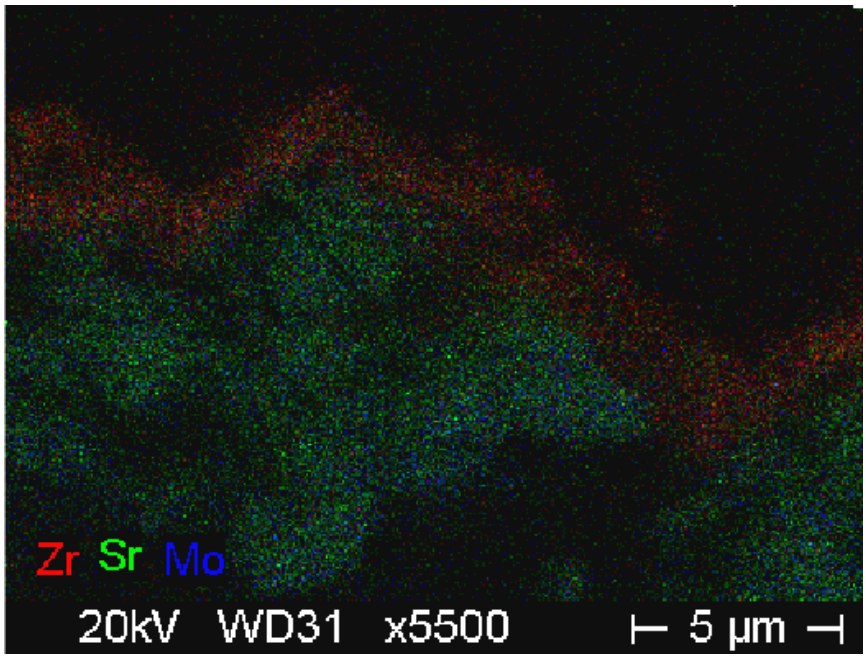


Figure 66: SEM elemental mapping of a YSZ PVD layer on a Sr_2VMoO_6 pellet

YSZ Electrolyte Supported Fabrication

Electrolytes for electrolyte supported SOFC's were fabricated by tape casting partially stabilized 3% and 8% yttrium doped YSZ (3YSZ and 8YSZ) and were also purchased from Fuel Cell Materials Inc. Electrolytes made of 3YSZ were first investigated due to the high associated strength due to the combination of cubic and tetragonal phases. As shown in Figure 67, when a crack and associated stress field is applied to the partially stabilized 3YSZ, the induced tetragonal to monoclinic phase change produces a volumetric expansion, which resists the crack propagation. This phenomenon can lead to high flexibility and added strength in thin YSZ electrolytes. The flexibility of a 30μm 3YSZ tape cast electrolyte is shown in Figure 68. While the tetragonal phase can increase strength in the electrolyte, it can lead to lower ionic conductivity at SOFC operating temperatures (850°C) (69; 70). As shown in Figure 69, 3YSZ will mostly form the tetragonal phase during sintering while 8YSZ will mostly form tetragonal and cubic phases during sintering. However, sintering aids such as Ni and Mn can help stabilize the cubic phase in YSZ and help densification at lower temperatures (71; 72).

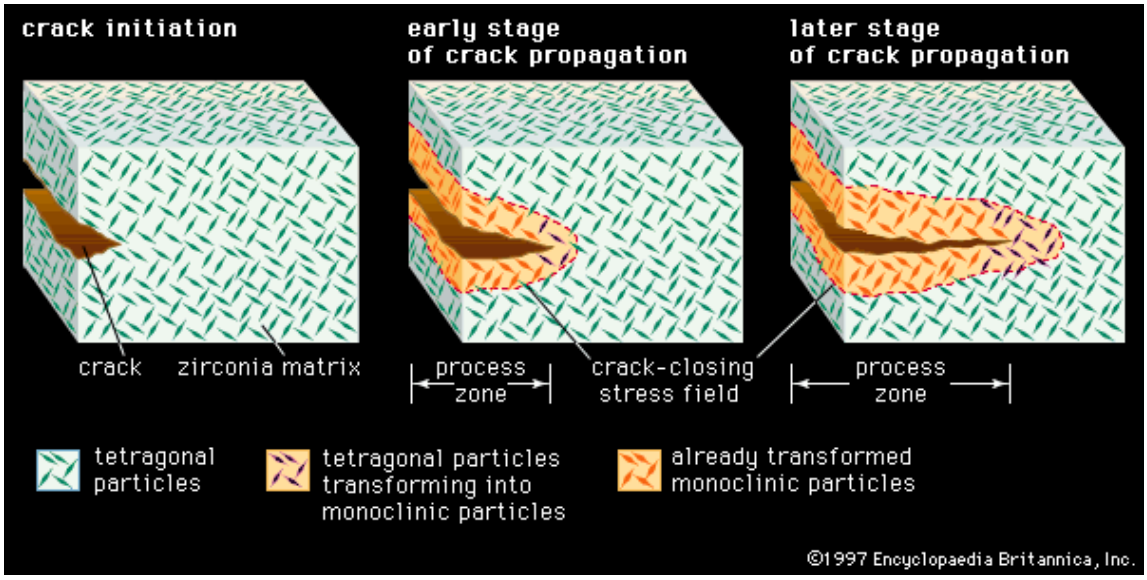


Figure 67: Transformation of tetragonal to monoclinic phase due to crack propagation (73)



Figure 68: Flexibility of a 30µm 3YSZ tape cast electrolyte

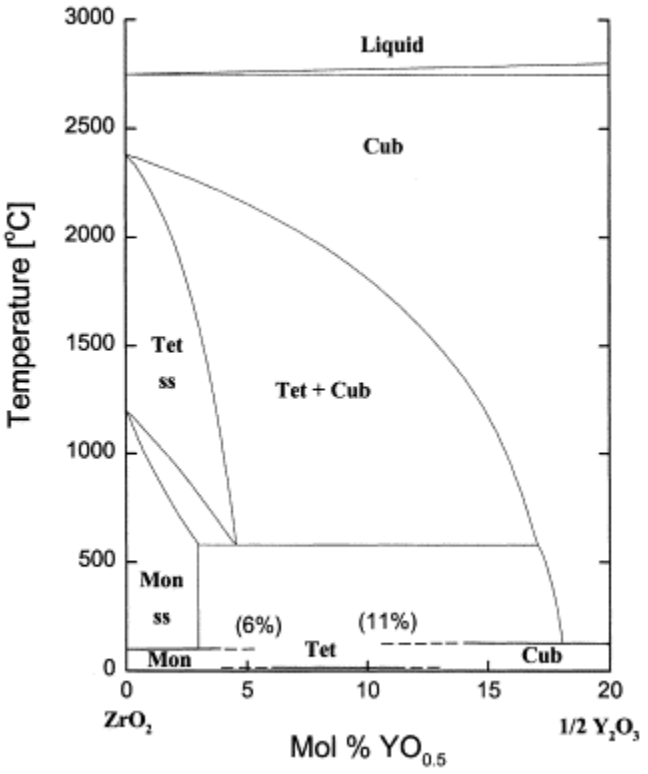


Figure 69: YSZ phase diagram (74)

1% Ni and 2% Mn doped 3YSZ was investigated at various sintering temperatures and dwell times. As shown in Figures 70 and 71, the Ni doped 3YSZ did not densify to the extent of the Mn doped 3YSZ. XRD was also performed on these tape casted disks to determine the amount of tetragonal and cubic phases present in the sintered samples. As shown in Figure 72, the XRD pattern from 70° to 77° 2θ can be used to determine the amount of tetragonal and cubic phases present in YSZ (69). The XRD pattern, as shown in Figure 73, for Ni and Mn doped 3YSZ indicates that only the tetragonal phase is present in the sintered substrates, which would not provide adequate ionic conduction for high temperature SOFC applications.

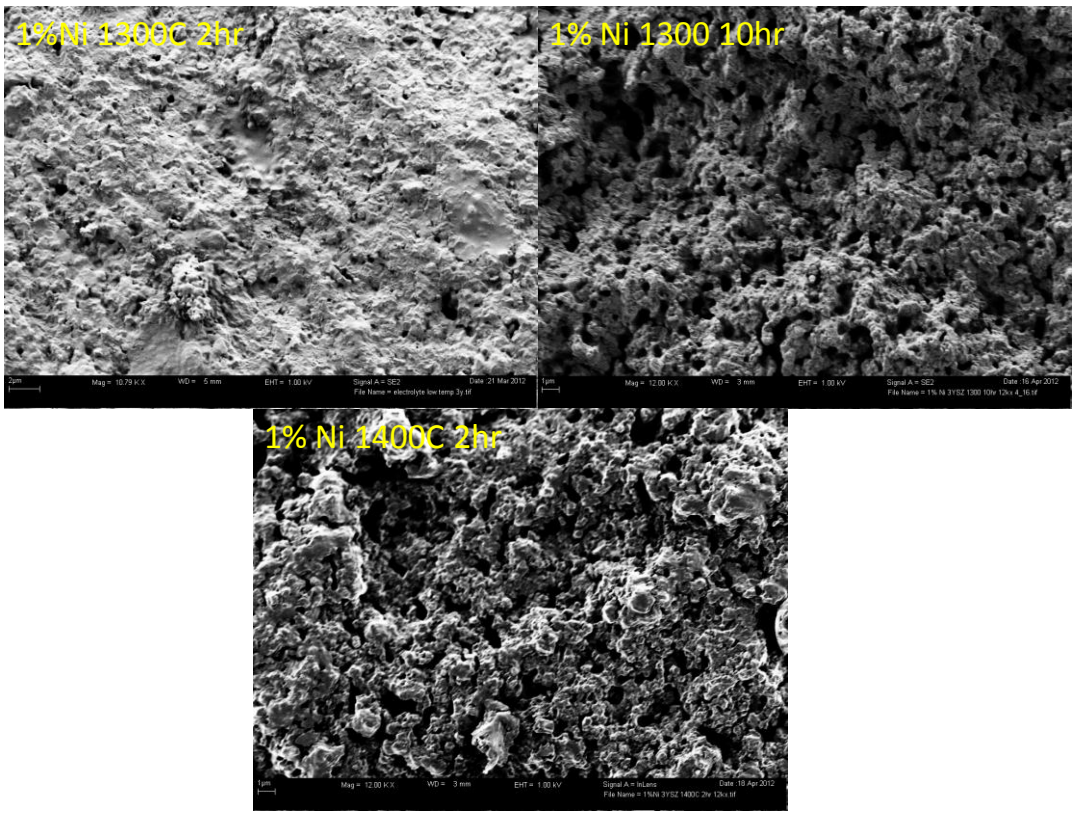


Figure 70: Microstructure of 1%Ni doped 3YSZ

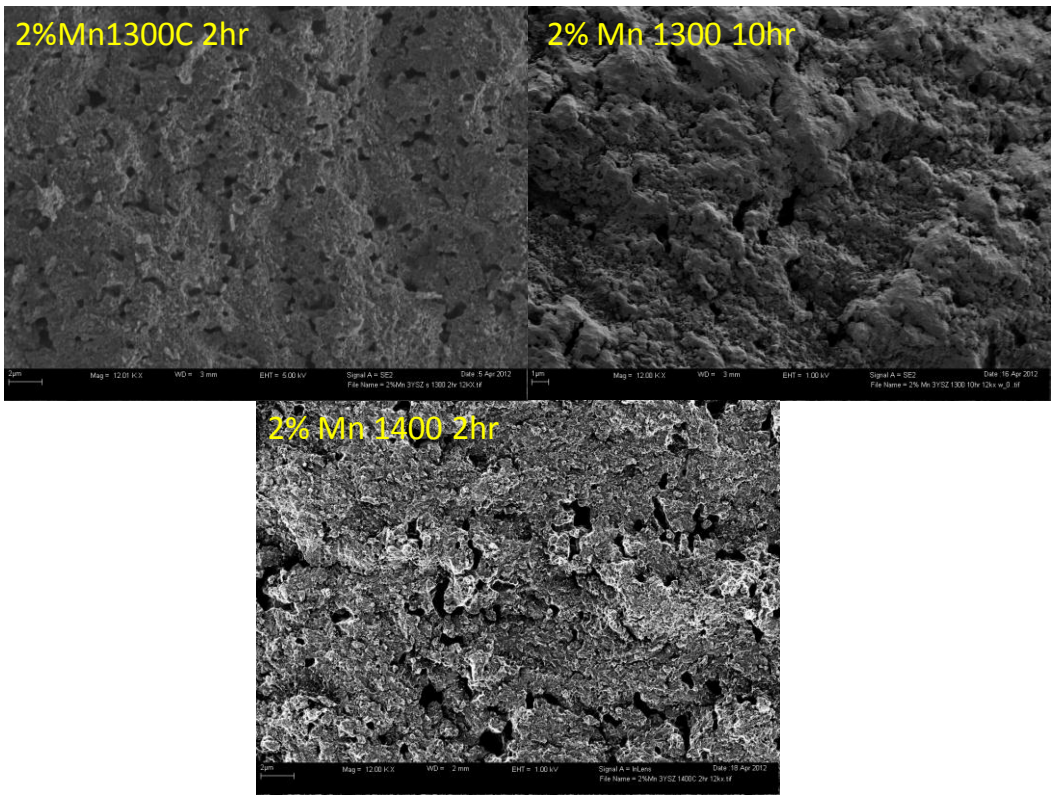


Figure 71: Microstructure of 2%Mn doped 3YSZ

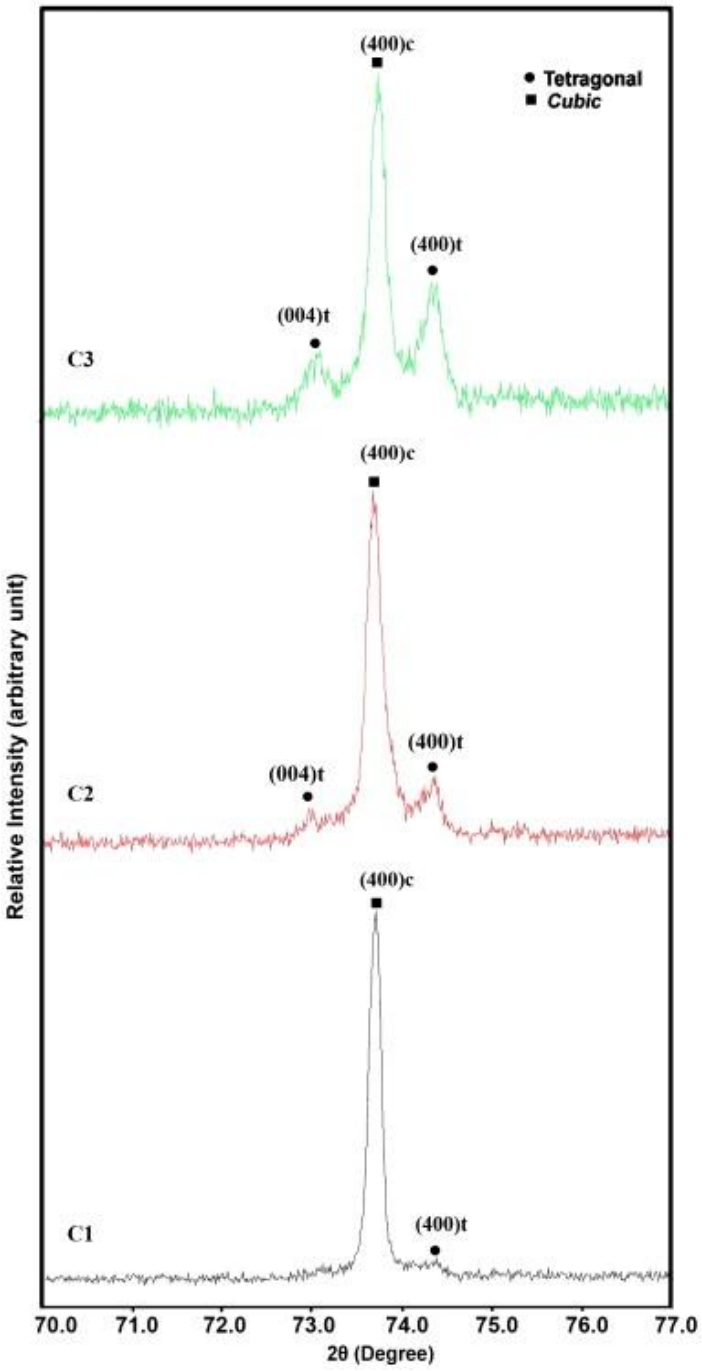


Figure 72: Tetragonal (t) and cubic (c) peaks in YSZ (69).

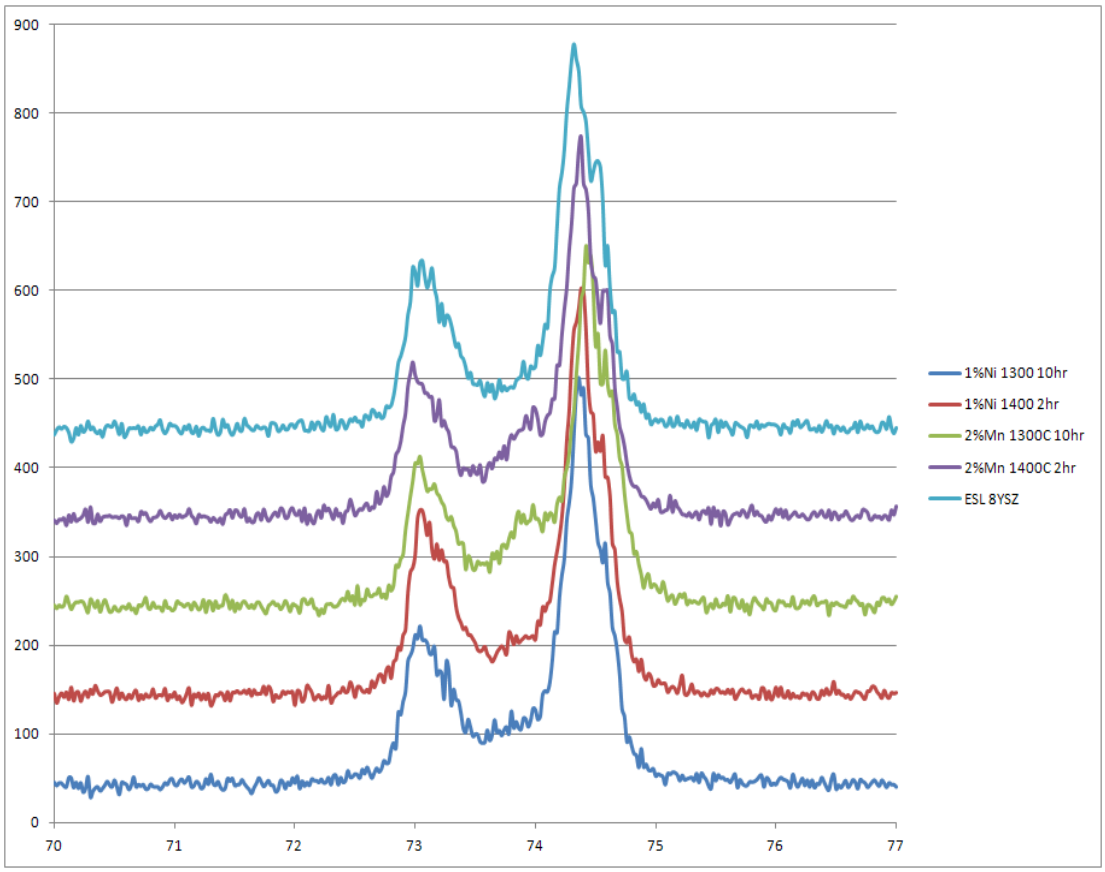


Figure 73: XRD patter for 1%Ni and 2%Mn doped 3YSZ

CHAPTER FIVE

NOVEL INTERCONNECT DESIGN

Introduction

One of the additional goals of this research was to test the fabricated SOFCs in a stack design for purposes of demonstrating reversible SOFC technologies for NASA applications. A stack is simply two or more fuel cells operated in electrical series with only a compact metal plate separating the discrete fuel cells and hence high temperature oxygen and fuel flow which can auto ignite at 536°C. A rough preliminary design was developed through a senior Capstone project and provided a framework and overall dimensions suitable for stack testing at MSU. While perhaps sufficient for demonstrating short stack tests, many opportunities for improvement have been identified. The senior capstone project designers, however, lacked direct hands on experience in fabricating and testing fuel cells which has required substantial revisions to serve as a permanent test bed for reversible stacks for both commercial fabricated and in house (MSU) fabricated SOFCs.

As shown in Figures 74 and 75 the original interconnect design included 11 flow channels for hydrogen and air transfer across the fuel electrode and air electrode, respectively. This design also includes inlet and outlet gas manifolds to disperse the gas to the flow channels and 90 degree edges wherever cuts are made. Some disadvantages of the original interconnect was the sealing of the manifolds, 90 degree edges, compatibility with multiple fuel cell sizes and complexity of the overall design. Because

of the large semicircle shape of the manifolds and small sections of non-machined area, the sealing of gasses would be difficult with another interconnect at 90 degrees from the original. Also, the stack design is intended to be sealed with a slightly compressed o-ring of mica, which would not be obtainable for this design. Protective coating of the interconnect is crucial to increasing the life span and the performance of the stainless steel over time, and is harder to apply to 90 degree edges and complex designs. The design also limits the size of fuel cells that can be used in the stack, because of shape of the flow channels and manifolds. Due to the complexity of this design, machining time and overall cost are also disadvantages. A smaller scale of the original design constructed to fit an HC Starck SOFC was modeled for CFD analysis as shown in Figure 75. The CFD analysis was calculated with a 150sccm gas flow to accurately predict the real life testing of a fuel cell. The flow field was analyzed for comparison to the new interconnect designs.

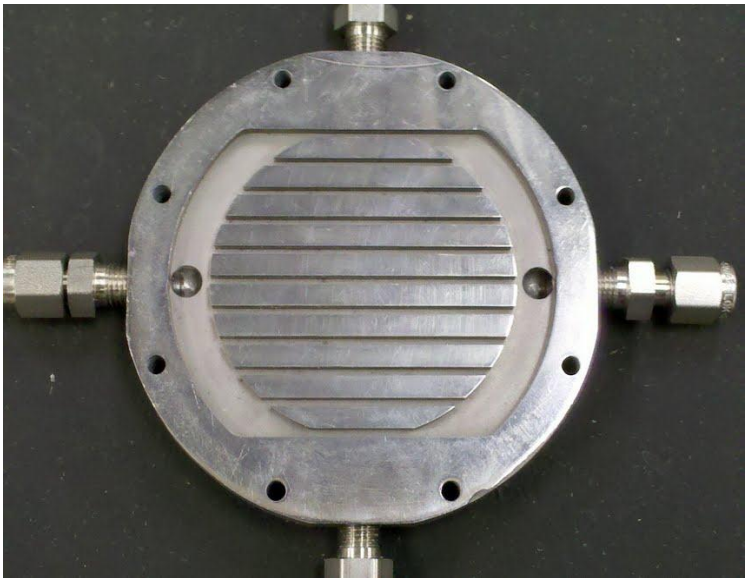


Figure 74: Original fabricated interconnect design

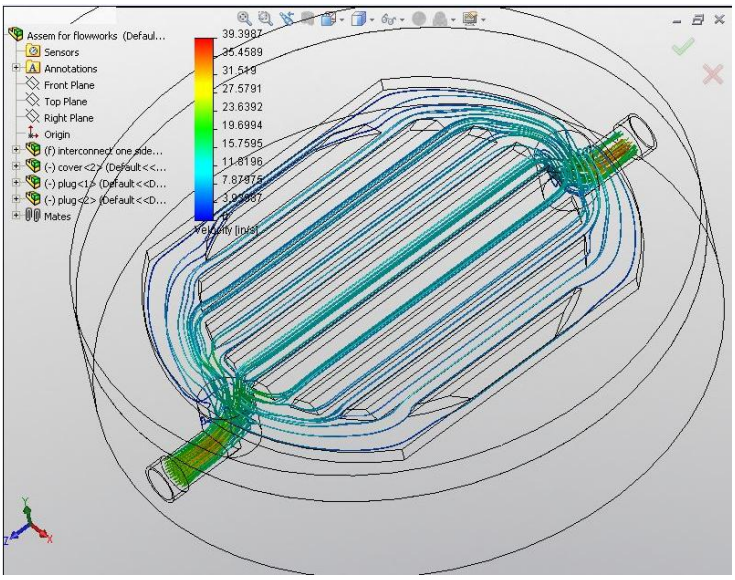


Figure 75: Original interconnect design modeled in SolidWorks FlowExpress

Novel Design

The proposed design, as shown in Figure 76, is dramatically simplified in that there a no flow channels needed, with only two holes for the incoming and outgoing gas. Based on the current methods of testing single cells with flow meshes, this new design is achievable because of the Ni and FeCrAl mesh that is placed on the top and the bottom of the fuel cell, that not only serves as a flow path, but also serves to conform to variations in flatness from cell to cell as shown in Figure 77. The foam creates multiple flow channels, as seen in Figure 78, and acts like multiple flow channels in all directions. The CFD analysis shows that with a laminar inlet flow rate of 150sccm and a Reynolds number of 775, the gas flows in a radial direction throughout the mesh inside of the mica ring, therefore verifying that this design would work when compared to the CFD analysis of the original design. This new design is capable of solving the problems with the

original design by eliminating the gas manifolds, 90 degree edges, and complexity of the overall design which is important given the high cost of the alloy and poor machineablility. The new design also allows for different size fuel cells to be utilized, because the inlet and outlet holes are brought into the middle of the interconnect enabling any size from 53mm to 18.5mm in diameter mesh and mica seal to be used.

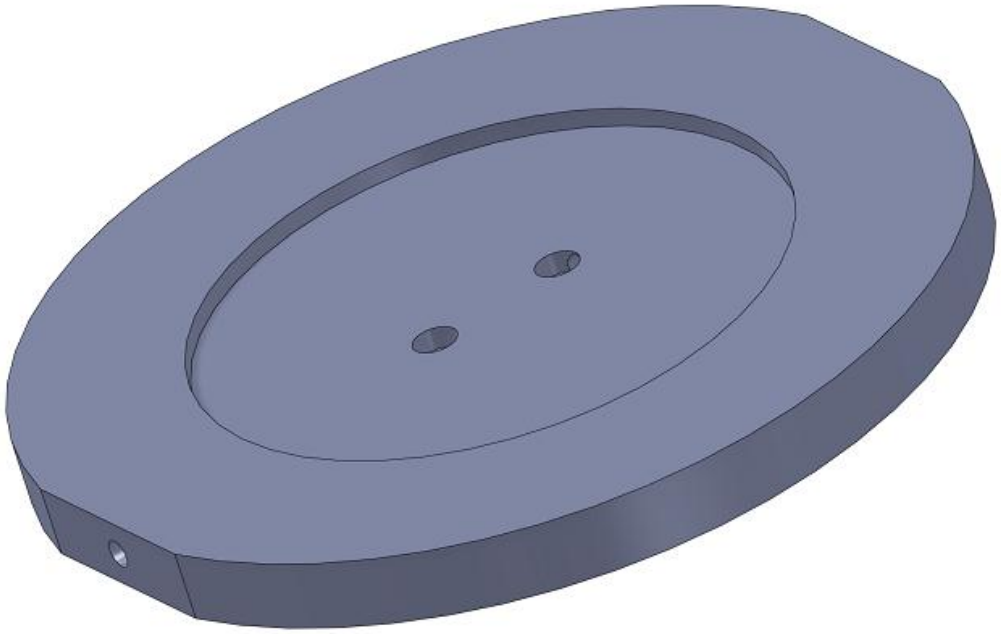


Figure 76: New end cap interconnect design

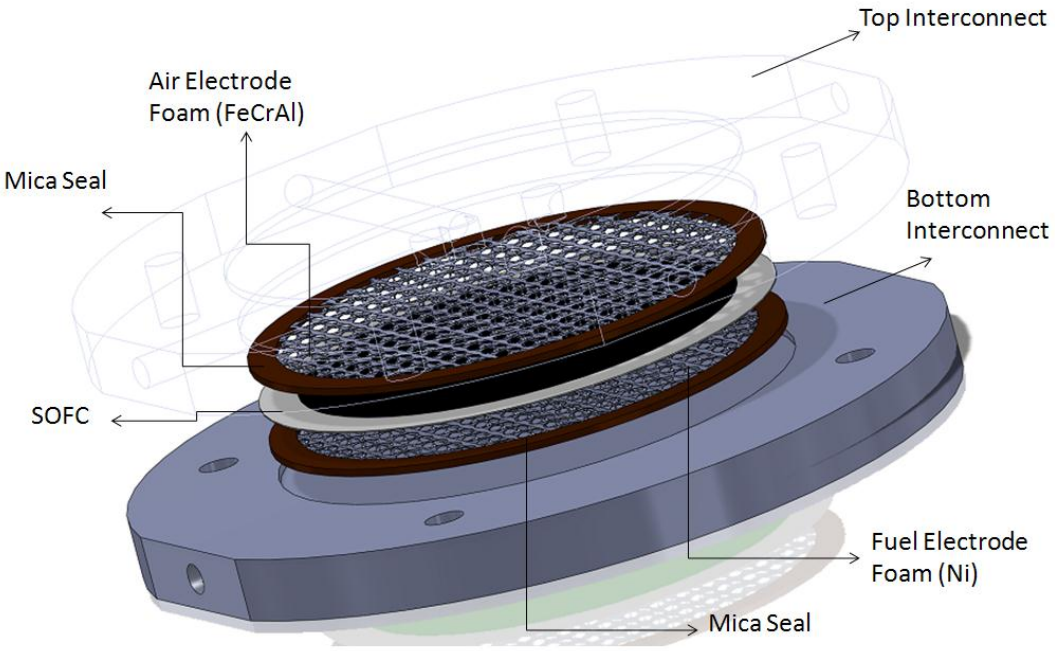


Figure 77: Example of one cell stack

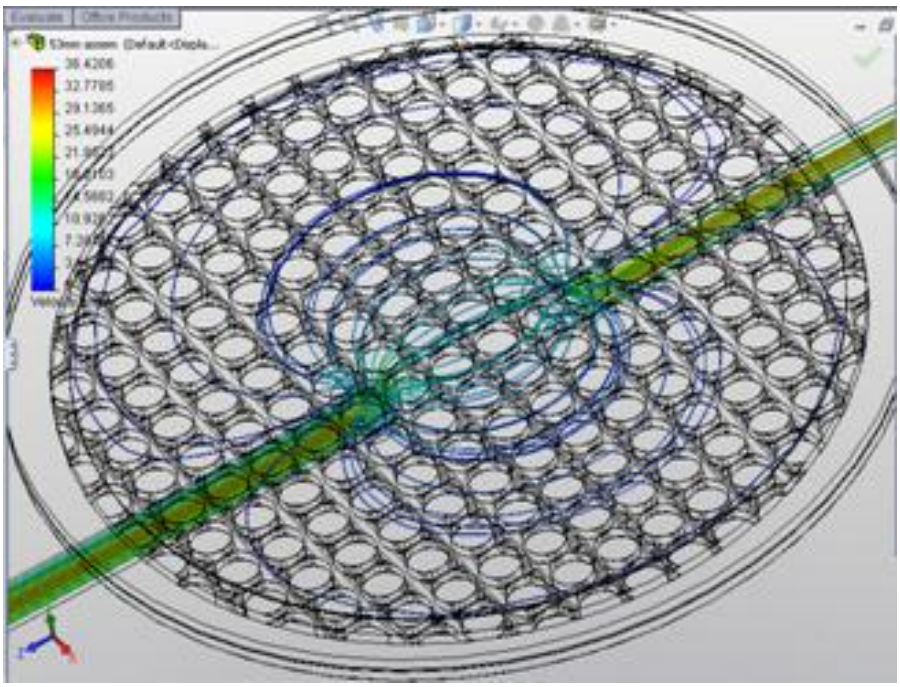


Figure 78: New interconnect design modeled in SolidWorks FlowExpress

Mesh Analysis

The mesh is the integral part of the new design and needed to be tested for pore structure compaction and electrical degradation. The flow channels or mesh pores needed to be analyzed under compaction, which will occur during fuel cell stack testing and proper sealing using the mica rings. The mesh was compacted at 0 psi, 1613 psi, and 3226 psi; cut in half, mounted in epoxy, and analyzed in a scanning electron microscope. Figures 79 and 80 show the pore structure of the mesh at 130X and 287X, respectively. This indicates that the open areas or pores show a decrease as the mesh is pressed, but still show a significant amount of pore area for gas flow. Resistance tests on the FeCrAl air electrode foams were performed on the mesh by connecting silver wire leads to the mesh via silver paste using the standard 4-probe measurement technique. The samples were then clamped into an alumina fixture and placed inside a tube furnace for which a controlled atmosphere could be introduced. Resistivity tests were then performed on mesh at 800°C in air for 100hr. As shown in Figure 81, the resistance decreases over the 100hr indicating that an electrical degradation in the mesh is not a concern.

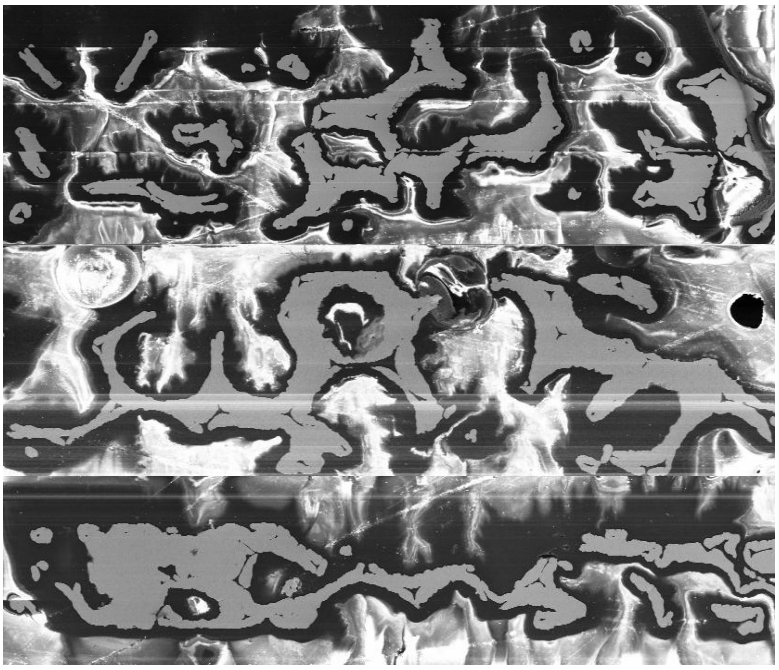


Figure 79: Mesh foam at 130X

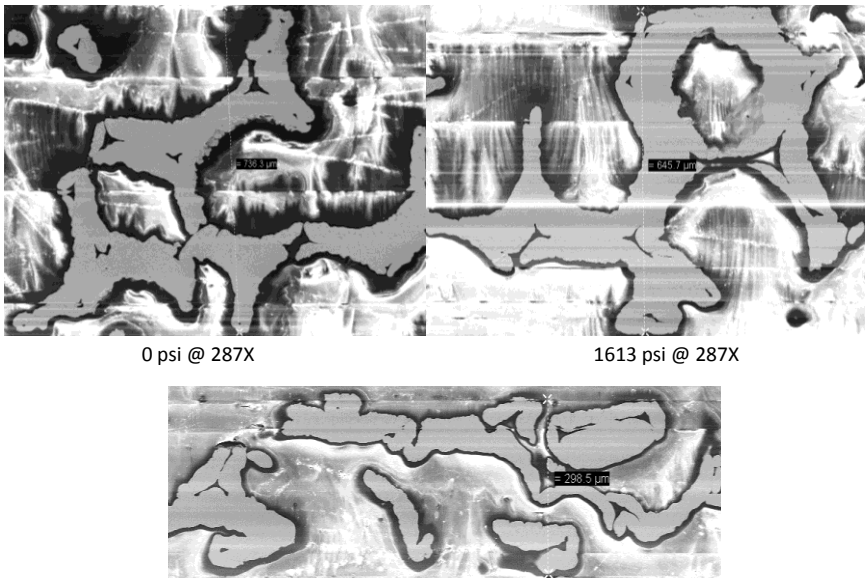


Figure 80: Mesh foam at 287X

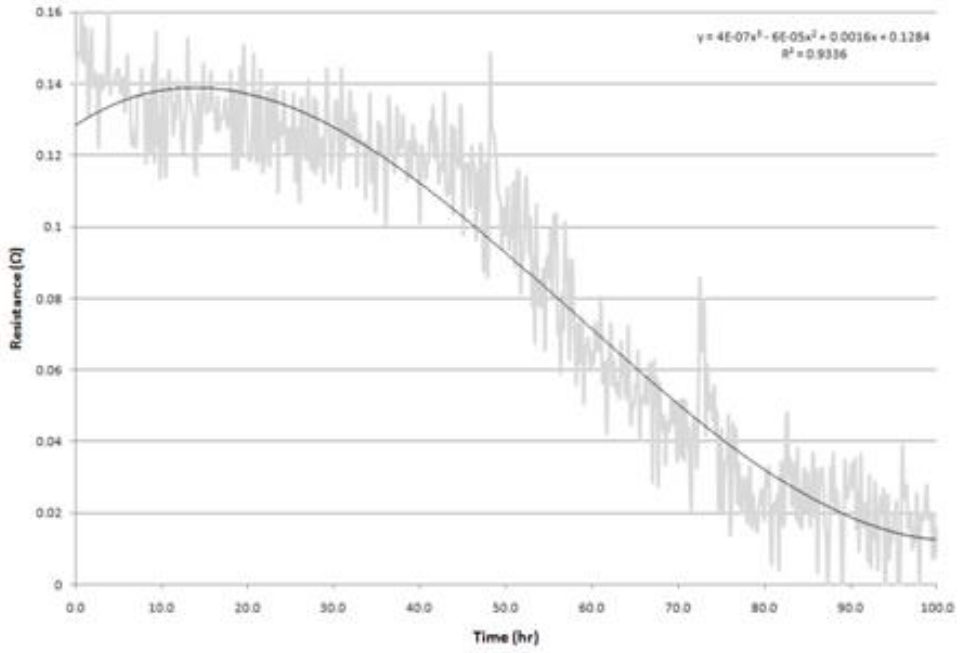


Figure 81: Resistance vs. Time for FeCrAl foam

Conclusions

A rough preliminary interconnect design was developed through a senior Capstone project and provided a framework and overall dimensions suitable for stack testing at Montana State University. While perhaps sufficient for demonstrating short stack tests, many opportunities for improvement have been identified. The senior capstone project designers, however, lacked direct hands on experience in fabricating and testing fuel cells which has required substantial revisions to serve as a permanent test bed for reversible stacks for both commercial fabricated and in house (MSU) fabricated SOFCs. The proposed novel design is dramatically simplified in that there a no flow channels needed, with only two holes for the incoming and outgoing gas. Based on the current methods of testing single cells with flow meshes, this new design is achievable

because of the Ni and FeCrAl mesh that is placed on the top and the bottom of the fuel cell, to serve as a flow path. The foam creates multiple flow channels and acts like multiple flow channels in all directions. This new design is capable of solving the problems with the original design by eliminating the gas manifolds, 90 degree edges, and complexity of the overall design which is important given the high cost of the alloy and poor machineablility. The new design also allows for different size fuel cells to be utilized, because the inlet and outlet holes are brought into the middle of the interconnect enabling any size from 53mm to 18.5mm in diameter mesh and mica seal to be used.

CHAPTER 6

CONCLUSIONS TO THE INVESTIGATION OF MULTIVALENT DOUBLE PEROVSKITES AS ELECTRODES FOR HIGH TEMPERATURE ENERGY CONVERSION

Processing and Characterization of $Sr_{2-x}VMoO_{6-\delta}$ Double Perovskites

In this study, the analysis and characterization of the processing and sintering of $Sr_{2-x}VMoO_{6-\delta}$ perovskites, was investigated. The XRD tests indicate that the phase pure double perovskite $Sr_{2-x}VMoO_{6-\delta}$ structure can only be achieved in a reducing atmosphere at high temperatures (1300˚C) and the $SrBO_{4-\delta}$ scheelite phase is the main phase at lower temperatures and oxidizing atmospheres. XPS revealed a deficiency of vanadium on the pellet surfaces, as 8 out of 9 samples had surface vanadium contents of less than 5%. The low vanadium concentration can be explained by the formation of the $SrMoO_{4-\delta}$ scheelite phase due to oxygen exposure on the surface of the pellets, which indicates vanadium migration to the bulk, and was exhibited in redox cycling. $Sr_{2-x}VMoO_{6-\delta}$ pellets sintered at 1300°C showed the lowest resistivity at both SOFC operating temperature (800°C) and room temperature. The resistivity tests also show a semiconductor to metallic transition for all double perovskites, from heating up to 800°C to cooling down to room temperature in a reducing atmosphere, related to the reduction of Mo6+ to Mo4+.

Electrical Conductivity of $Sr_{2-x}VMoO_6$ (x=0.0, 0.1, 0.2) Double Perovskite Solid Oxide Fuel Cell Fuel Electrode

Electrical conductivity of $Sr_{2-x}VMoO_{6-y}$ (x=0.0, 0.1, 0.2) fuel electrode material has been investigated in a reducing atmosphere at temperatures up to 800 ^{0}C. Elemental valence states were identified through X-ray photoemission on the double perovskite material before and after annealing in a hydrogen environment. Samples exhibited metallic conduction with electrical conductivities of 1250 S/cm ($Sr_2VMoO_{6-y'}$), 2530 S/cm ($Sr_{1.8}VMoO_{6-y''}$) and 3610 S/cm ($Sr_{1.9}VMoO_{6-y'''}$) at 800 ^{0}C in 5%H_2/95%N_2. A highly insulating phase begins to reduce between 400 and 500 ^{0}C in a 5%H_2/95%N_2 environment, as confirmed by X-ray photoemission and thermal gravimetric analysis. This reduction leads to a large increase in electrical conductivity.

The electrical conductivity of $Sr_{2-x}VMoO_{6-\delta}$ materials at 800 ˚C in a 2.9% H_2O/ 4.9%H_2/92.2%N_2 environment exceeds that reported for state of the art Ni-YSZ fuel elelectrodes by a factor of ~1.25-3 at the same temperature in similar environments. Polycrystalline $Sr_{1.9}VMoO_{6-\delta}$ samples exhibited higher conductivity than that reported for $SrMoO_3$ polycrystalline samples. A single crystal sample of $Sr_{1.9}VMoO_{6-\delta}$ would be a candidate for exhibiting the highest known conducting oxide.

Fuel Electrode Performance of Sr_2VMoO_6 Double Perovskites

$Sr_2VMoO_{6-\delta}$ fuel electrodes were synthesized utilizing both solid state synthesis and solution synthesis. A problem that was encountered when utilizing the screen printed double perovskite fuel electrode with the YSZ electrolyte was the delamination of the electrode from the electrolyte during the sintering of the two layers. The SEM elemental

line scans indicated that there was no major migration of the cation elements around the interface. This would indicate that there is not a large amount of $SrZrO_3$ formation between the YSZ and $Sr_2VMoO_{6-\delta}$. However, an anion reaction between YSZ and $Sr_2VMoO_{6-\delta}$ layers could result in the formation of the $SrMoO_4$ scheelite structure.

The infiltrated SOFC with the solution $Sr_2VMoO_{6-\delta}$ was able to produce max power density of 194.8mW/cm^2 at 0.87V. However, upon further XRD analysis, the perovskite phase was not fully developed at 850°C, which lead to the investigation into utilizing a reduction agent and the infiltration of $SrBO_{4-\delta}$ fuel electrodes. A 19.05mm (3/4in) pellet containing a mixture of MoO_3 and TiH_2 was sintered in a reducing environment and MoO_3 was still present, however the desired reduction to MoO_2 was observed along with the oxidation of Ti. $SrMoO_{4-\delta}$ and $SrVO_{4-\delta}$ infiltrated fuel electrodes performed well in initial testing and should be further investigated as fuel electrode materials, as the infiltration of the elements was very low.

Novel Interconnect Design

A rough preliminary interconnect design was developed through a senior Capstone project and provided a framework and overall dimensions suitable for stack testing at Montana State University. While perhaps sufficient for demonstrating short stack tests, many opportunities for improvement have been identified. The senior capstone project designers, however, lacked direct hands on experience in fabricating and testing fuel cells which has required substantial revisions to serve as a permanent test bed

for reversible stacks for both commercial fabricated and in house (MSU) fabricated SOFCs.

The proposed novel design is dramatically simplified in that there a no flow channels needed, with only two holes for the incoming and outgoing gas. Based on the current methods of testing single cells with flow meshes, this new design is achievable because of the Ni and FeCrAl mesh that is placed on the top and the bottom of the fuel cell, to serve as a flow path. The foam creates multiple flow channels and acts like multiple flow channels in all directions. This new design is capable of solving the problems with the original design by eliminating the gas manifolds, 90 degree edges, and complexity of the overall design which is important given the high cost of the alloy and poor machineablility. The new design also allows for different size fuel cells to be utilized, because the inlet and outlet holes are brought into the middle of the interconnect enabling any size from 53mm to 18.5mm in diameter mesh and mica seal to be used.

Acknowledgments to the Investigation of Multivalent
Double Perovskites as Electrodes for High
Temperature Energy Conversion

This work was supported by NASA EPSCoR under grant #NNX09AP73A

REFERENCES

1. Garrison, Earnest. Solid Oxide Fuel Cells. *Illinois Institute of Technology.* [Online] [Cited: March 14, 2011.] http://mypages.iit.edu/~smart/garrear/fuelcells.htm.

2. NFCRC Tutorial: Solid Oxide Fuel Cell (SOFC). *National Fuel Cell Research Center.* [Online] [Cited: March 14, 2011.] http://www.nfcrc.uci.edu/EnergyTutorial/sofc.html.

3. EG&G Technical Services, Inc. *Fuel Cell Handbook (Seventh Edition).* Morgantown : U.S. Department of Energy, 2004.

4. Hill, Micheal. *Ceramic Industry.* [Online] September 1, 2005. [Cited: March 14, 2011.] http://www.ceramicindustry.com/Articles/Feature_Article/10637442bbac7010VgnVCM100000f932a8c0____.

5. *Anchoring of Infiltrated Nickel Electro-Catalyst by Addition of Aluminum Titanate.* Law, C.H. Vancouver : The Electrochemical Society, 2010.

6. Stormer, Dr. Ni modellanoden. *Karlsruher Institut fur Technologie.* [Online] [Cited: October 06, 2010.] http://www.lem.kit.edu/21_198.php.

7. *Study of the Crystal Structure, Thermal Stability and Conductivity of Sr(V0.5Mo0.5)O3 as SOFC Material.* A., Aguadero, et al. 2010, Fuel Cells, Vol. 11, pp. 44-50.

8. *Conductivity and stability of SrVO3 and mixed perovskites at low oxygen partial pressures.* S., Hui and A., Petric. 2001, Solid State Ionics, Vol. 143, pp. 275-283.

9. *Double Perovskties as Anode Materials for Solid-Oxide Fuel Cells.* 2006, Science, Vol. 312, pp. 254-257.

10. *Electronic, megnetic and structrual properties of A2VMoO6 perovskites.* P., Karen, et al. 2006, Journal of Solid State Chemistry, Vol. 179, pp. 2120-2125.

11. *Molybdate Based Ceramic Negative-Electrode Materials for Solid Oxide Cells.* C., Graves, B., Sudireddy and M., Mogensen. 2010, ECS Transactions, Vol. 28, pp. 173-192.

12. *Mixed Conductivity in Perovskite SOFC Materials La1-xMxMn1-yCoyO3 (M=Ca or Sr).* A., Mackor, et al. 1990, Energy Conversion Engineering Conference, Vol. 3, pp. 251-255.

13. A., Bieberle. *The Electrochemistry of Solid Oxide Fuel Cell Anodes: Experiments, Modeling, and Simulations.* Swiss Federal Institute of Technology. 2000. Dissertation.

14. *Conductivity and stability of SrVO3 and mixed perovskites at low oxygen partial pressures.* Hui, Shiqiang and Petric, Anthony. 3-4, s.l. : Solid State Ionics, 2001, Vol. 143.

15. *Electrical conductivity and structural stabiliy of La-doped SrTiO3 with A-site deficiency as anode materials for solid oxide fule cells.* x., Li, et al. 2010, International Journal of Hydrogen Energy, Vol. 35, pp. 7913-7918.

16. *Electrical Properties of Yttrium-Doped Strontium Titanate under Reducing Conditions.* Hui, Shiqiang and Petric, Anthony. 1, s.l. : The Electrochemical Society, 2002, Vol. 149.

17. *The Influence of A-site-deficiency on the Performance of Strontium Doped Lanthanum-Manganate Perovskite Type SOFC Cathodes.* A., Weber, et al. 1996, High Temperature Electrochemistry.

18. *Electronic, magnetic and structural properties of A2VMoO6 perovskites (A=Ca, Sr).* Karen, P., et al. 7, s.l. : Journal of Solid State Chemistry, 2006, Vol. 179. 00224596.

19. *Nickel coarsening in annealed Ni/8YSZ anode substrates for solid oxide fuel cells.* Simwonis, D., Tietz, F. and D., Stover. 3-4, s.l. : Solid State Ionics, 2000, Vol. 132.

20. *Understanding Nickel Ocidation and Reduction Processes in SOFC Systems.* Young, J, et al. 1, Nara, Japan : The Electrochemical Society, 2007, Vol. 7. 1938-6737.

21. *Characterization of sulfur poinsoning of Ni-USZ anodes for solid oxide fuel cells using in situ Raman microspectroscopy.* Cheng, Zhe and Liu, Meilin. 13-14, s.l. : Solid State Ionics, 2007, Vol. 178.

22. *Sulfur-tolerant anode materials for solid oxide fuel cell application.* Gong, Mingyang, et al. 2, s.l. : Journal of Power Sources, 2007, Vol. 168.

23. *Mechanism for SOFC anode degradation from hydrogen sulfide exposure.* Lussier, A, et al. 14, s.l. : International Journal of Hydrogen Energy, 2008, Vol. 33. 03603199.

24. *Molybdenum Based Perovskite Electrodes for Solid Oxide Cells.* Graves, Christopher, Sudireddy, Bhaskar and Mogensen, Mogens. Vancouver : s.n., 2010. The Electrochemical Society.

25. *Double Perovskites as Anode Materials for Solid-Oxide Fuel Cells.* Huang, Yun-Hui, et al. 2006, Science Magizine, pp. 254-257.

26. *Sr2Fe4/3Mo2/3O6 as anodes for solid oxide fuel cells.* Xiao, Guoliang, et al. 24, s.l. : Journal of Power Sources, 2010, Vol. 195.

27. *Synthesis and properties of Ni-YSZ cermet: anode material for solid oxide fuel cells.* Aruna, S.T, Muthuraman, M and Patil, K.C. 1-2, s.l. : Solid State Ionics, 1998, Vol. 111.

28. Lide, David R. *Handbook of Chemistry and Physics.* s.l. : CRC Press, 2004-2005.

29. *Molybdenum based catalysts. I. MoO2 as the active species in the reforming of hydrocarbons.* Katrib, A., et al. 1-2, s.l. : Catalysis Letters, 1996, Vol. 38. 1011372X.

30. *Nature and Activity of Some Vanadium Catalysts.* Whittington, B.I. and R., Anderson J. 5, s.l. : The Journal of Physical Chemistry, 1993, Vol. 97.

31. *A method for the solution of certain non-linear problems in least squares.* Levenberg, Kenneth. s.l. : Quarterly of Applied Mathematics, 1944, Vol. 2.

32. Mayer, M. SIMNRA User's Guide. *Technical Report.* Garching : Max-Plank-Institut fur Plasmaphysik, 1997.

33. *Autothermal oxidative coupling of methane on the SrCO3/Sm2O3 catalysts.* Wang, Kai, et al. 6, s.l. : Catalysis Communications, 2009, Vol. 10. 1566-7367.

34. *The processes of formation and epitaxial alignment of SrTiO3 thin films prepared by metallo-organic decomposition.* Braunstein, G., et al. 2, s.l. : Journal of Applied Physics, 1993, Vol. 73. 10.1063/1.353310.

35. *XPS study of as-prepared and reduced molybdenum oxides.* Choi, J.G. and Thompson, L.T. 2, s.l. : Applied Surface Science, 1996, Vol. 93. 0169-4332.

36. *Stuctural and surface characterization of perovskite-type oxides; influence of A and B substitutions upon oxygen binding energy.* Pradier, C.-M., et al. 12, s.l. : Journal of Materials Science, 1998, Vol. 33. 0022-2461.

37. *Resolving surface chemical states in XPS analysis of first row transition metals, oxides and hydroxides: Sc, Ti, V, Cu and Zn.* Biesinger, Mark C., et al. 3, s.l. : Applied Surface Science, 2010, Vol. 257. 0169-4332.

38. *Solid Oxide Fuel Cells damage mechanisms due to Ni-YSZ re-oxidation: Case of the Anode Supported Cell.* Laurencin, J., et al. s.l. : Journal of Power Sources, 2009, Vol. 192.

39. *Effects of powder sizes and reduction parameters on the strength of Ni-YSZ anodes.* Wang, Y., et al. s.l. : Solid State Ionics, 2006, Vol. 177.

40. *Fe valence state of Sr2FeMoO6 probed by x-ray absorption spectroscopy: The sample age matters.* Kuepper, K., et al. s.l. : Journal of Applied Physics, 2008, Vol. 104.

41. *On the formation of double perovskite Sr2FeMoO6.* Fang, Tsang-Tse, Wu, M.S. and Ko, T.F. 17, s.l. : Journal of Materials Science Letters, 2001, Vol. 20.

42. *Evaluation of Sr2CoMoO6 as anode material in solid-oxide fuel cells: A neutron diffraction study.* Aguadero, A., et al. s.l. : Journal of Applied Physics, 2011, Vol. 109.

43. *Synthesis and electronic properties of the solid solutions SrVxMo1-xO3 with the perovskites.* Fatiev, V.A., Bazuev, G.C. and Zubkov, V.G. 6, s.l. : Inorganic Materials, 1987, Vol. 23.

44. *Study of the Crystal Structure, Thermal Stability and Conductivity of Sr(V0.5Mo0.5)O3 as SOFC Material.* Aguadero, A., et al. 1, s.l. : Fuel Cells, 2010, Vol. 11.

45. *Direct oxidation of hydrocarbons in a solid-oxide fuel cell.* S., Park, J. M., Vohs and R. J., Gorte. 2000, Nature, Vol. 404, pp. 265-267.

46. *A review on the status of anode materials for solid oxide fuel cells.* W. Z., Zhu and S. C., Deevi. 2003, Material Science and Engineering, Vol. 362, pp. 228-239.

47. *Fundamental mechanisms limiting solid oxide fuel cell durability.* H., Yokokawa, et al. 2008, Journal of Power Sources, Vol. 182, pp. 400-412.

48. *Characterization of sulfur poisoning of NiYSZ anodes for solid oxide fuel cells using in situ raman microspectroscopy.* Z., Cheng and M., Liu. 2007, Solid State Ionics, Vol. 178, pp. 925-935.

49. *Density functinoal theory studies of methane dissociation on anode catalysts in solid-oxide fuel cells: Suggestions for coke reduction.* N. M., Galea, D., Knapp and T., Ziegler. 2007, Journal of Catalysis, Vol. 247, pp. 20-33.

50. *Synthesis and electrical properties of the solid solutions SrVxMo1-xO3 with the perovskite structure.* V., Fotiev, G., Bazuev and V., Zubkov. 1987, Inorganic Materials, pp. 895-898.

51. *Synthesis and properties of Ni-YSZ cermet: anode material for solid oxide fuel cells.* S. T., Aruna, M., Muthuraman and K. C., Patil. 1998, Solid State Ionics, Vol. 111, pp. 45-51.

52. *Double-perovksite anode materials Sr2MMoO6 (m=Co, Ni,) for solid oxide fuel cells.* Y. H., Huang, et al. 2009, Chemistry of Materials, Vol. 21, pp. 2319-2326.

53. *Inductions of colossal magnetoresistance in the double perovskite SrCoMoO6.* M. C., Viola, et al. 2002, Chemistry of Materials, Vol. 14, pp. 812-818.

54. *Effect of Nb doping on double perovskite oxides Sr2CrMoO6 as anode for SOFC.* J., Yin, et al. Meeting of the International Society of Electrochemistry Proceedings.

55. *Double-perovskites A2FeMoO6 (a=Ca, Sr, Ba) as anodes for solid oxide fuel cells.* L., Zhang, et al. 2010, Journal of Power Sources, Vol. 195, pp. 6356-6366.

56. *Isovalent and aliovalent substitution effects on redox chemistry of Sr2MgMoO6 SOFC-anode material.* S., Vasala, et al. 2010, Solid State Ionics, Vol. 181, pp. 754-759.

57. *Highest conductivity oxide SrMoO3 grown by a coating zone method under ultralow oxygen partial pressure.* I., Nagai, et al. 2005, Applied Physics Letters, Vol. 87.

58. *Metallic conductivity in perovskit-type compounds AMoO3 (a-Ba, Sr, Ca) down to 2.5K.* S., Hayashi, R., Aoki and T., Nakamura.

59. *SrVO3 and SrVO4, electrical properties below and above room temperature.* V., Giannakopoulou, et al.

60. *Optimizedeffective potential modle for the double perovskites Sr2-xYxVMoO6 and Sr2-xYxVTcO6.* I. V., Solovyev. 2011, Journal of Physics and Condensed Matter, Vol. 23.

61. *Structural and electrical properties of Sr2V2O8 Ceramics.* P., Khatri, B., Behera and R. N. P., Choudhary. 2009, Physica Status Solidi, Vol. 246, pp. 1118-1123.

62. *A simple aqueous mineralization process to synthesize tetragonal molybdate microcrystallites.* D., Chen, et al. 2006, Crystal Growth and Design, Vol. 6, pp. 247-252.

63. AMPERGY Solid Oxide Fuel Cell products. *H.C. Starck Cermaics.* [Online] H.C. Starck. [Cited: March 17, 2011.] http://www.hcstarck-ceramics.com/index.php?page_id=2702.

64. *Study of the Crystal Structure, Thermal Stability and Conductivity of Sr(V0.5Mo0.5)03 as SOFC Material.* Aguadero, A., et al. 1, s.l. : Fuel Cells, 2010, Vol. 11.

65. *Redox behaviour, chemical compatibility and electrochemical performance of Sr2MgMoO6 as SOFC anode.* D., Marrero-Lopez, et al. 2010, Solid State Ionics, Vol. 180, pp. 1672-1682.

66. *Thermal expansion coefficient of yttria stabiliized zirconia for various yttria contents.* H., Hayashi, et al. 2005, Solid State Ionics, Vol. 176, pp. 613-619.

67. Molybdenum(VI) Oxide. *Chemistry Reference.* [Online] [Cited: August 20, 2012.] http://www.chemistry-reference.com/.

68. The Ellingham diagram. *DoITPoMS.* [Online] University of Cambridge. [Cited: August 20, 2012.] http://www.doitpoms.ac.uk/tlplib/ellingham_diagrams/ellingham.php.

69. *Investigation of electrical and mechanical properties of 3YSZ/8YSZ composite electrolytes.* Ghatee, M., Shariat, M.H. and Irvine, J.T.S. s.l. : Solid State Ionics, 2009, Vol. 180.

70. *Tetragonal zirconia polycrystals - a high performance solid oxygen ion conductor.* Weppner, W. s.l. : Solid State Ionics, 1992, Vol. 52.

71. *Chemical and Structural Changes in Manganese-Doped Yttria-Stabilized Zirconia Studied by Electron Energy Loss Spectroscopy Conbined with Electron Diffraction.* Appel, Charlotte C., et al. s.l. : American Ceramics Society, 1999, Vol. 82.

72. *Conductivity of Mn and Ni-doped stabilized zirconia electrolyte.* Herle, Jan Van and Vasquez, Ruben. s.l. : Journal of the European Ceramic Society, 2004, Vol. 24.

73. *advanced ceramics: cracking in transformation-toughened zirconia.* Encyclopaedia Britannica Online, s.l. : 2012.

74. *Phase compostion and its changes during annealing of plasma-sprayed YSZ.* IIavsky, Jan and Stalick, Judith. 2-3, s.l. : Surface and Coatings Technology, 2000, Vol. 127.

75. *A method for the solution of certain non-linear problems utilizing leat squares.* Levenberg, Kenneth. 1944, Applied Mathematics, pp. 164-168.

76. Cava, Rovert J. Cava Lab. *Princeton University.* [Online] [Cited: July 1, 2010.] http://www.princeton.edu/~cavalab/tutorials/public/structures/perovskites.html.

77. Faraji, Sedigheh. *Hydrogen Production from methane Using Oxygen-permeable Ceramic.* s.l. : University of Kansas.

78. Linseis Thermal Analysis. *Linseis.* [Online] [Cited: January 10, 2011.] http://www.linseis.net/html_en/thermal/dilatometer/l75v.php.

79. *Application of XPS to study electrocatalysts for fuel cells.* Corcoran, C.J., et al. 2010, Journal of Power Sources, pp. 7856-7879.

80. X-ray photoelectron spectroscopy. *Wikipedia The Free Encyclopedia.* [Online] [Cited: March 1, 2011.] http://en.wikipedia.org/wiki/X-ray_photoelectron_spectroscopy.

81. X-ray Diffraction (XRD). *Portland State University.* [Online] [Cited: March 1, 2011.] http://web.pdx.edu/~pmoeck/phy381/Topic5a-XRD.pdf.

82. *Teh mechanical and electrical properties of Ni/YSZ anode supoort for solid oxide fuel cells.* He, Changrong, Chen, Tao and Wang, Wei Guo. 2008.

83. X-raay Absorption Spectroscopy (XAS). *Department of Chemistry.* [Online] University of Calgary. [Cited: August 08, 2010.] www.chem.ucalgary.ca/research/groups/faridehj/xas.pdf.

84. Natelson, Doug. What is a polaron? *Nanoscale Views.* [Online] January 24, 2009. [Cited: July 05, 2010.] http://nanoscale.blogspot.com/2009/01/what-is-polaron.html.

85. *Adiabatic and non-adiabatic hopping conduction in La-Pb-Mn-0 type stystem.* Banerjee, A., et al. s.l. : International Conference on Magnetic materials, 2001.

86. Voltage induced Ti valence switching in SrTiO3. *Photon Science.* [Online] Desy, 2009. [Cited: October 24, 2011.] http://hasylab.desy.de/news__events/research_highlights/perovskite_like_crystal_in_an_electric_field/index_eng.html.

87. Mass Spectrometry. *Michigan State University Department of Chemistry.* [Online] Michigan State University. [Cited: October 27, 2011.] http://www2.chemistry.msu.edu/faculty/reusch/VirtTxtJml/Spectrpy/MassSpec/masspec1.htm.

88. Photoelectron Spectroscopy. *Biological & Chemical Sciences.* [Online] Queen Mary Univeristy of London. [Cited: November 11, 2011.] http://www.chem.qmul.ac.uk/surfaces/scc/scat5_3.htm.

89. *Understanding Nickel Oxidation and Reduction Processes in SOFC Systems.* Young, J, et al. 1, Nara, Japan : The Electrochemical Society, 2007, Vol. 7. 1938-6737.

90. *Highest conductivity oxide SrMoO3 grown by a coating zone method under utralow oxygen partial pressure.* I., Nagi, et al. 2005, Applied Physics Letters, Vol. 87.